GHENT UNIVERSITY

FACULTY OF SCIENCE

Aqueous chemical solution deposition of $La_2Zr_2O_7$ and La-, Ce- substituted buffer layers for coated conductors

Vyshnavi Narayanan

Promoter : Prof. Dr. I. Van Driessche

Thesis submitted in fulfillment of the requirements for the degree of Doctor (PhD) in Sciences: Chemistry

SCRIPTS, Department of Inorganic and Physical Chemistry
Faculty of Sciences
April 2012

UNIVERSITEIT GENT

Faculteit Wetenschappen

This research was performed at:

Ghent University
Department of Inorganic and Physical Chemistry, Faculty of Sciences Krijgslaan 281 (S3),
B-9000 Gent, Belgium
Tel. +32 (0)9 264 44 21; Fax +32 (0)9 264 49 83;

Acknowledgement

First and foremost I would like to thank Prof. Dr. Em. Serge Hoste for providing me a Ph. D position to perform research in the department of inorganic and physical chemistry, Ghent University. His enthusiastic guidance in the first two years of my Ph.D was motivating and thought provoking. His support in the final two years despite being retired from active professorship is highly commendable and unforgettable.

I would like to express my gratitude to my promoter Prof. Dr. Isabel Van Driessche for taking over the promotership from Prof. Dr. Em. Serge Hoste and thereon carrying it forward. I thank her for her active participation in reviewing my research work from time to time.

I express my deep appreciation to Prof. Dr. Klaartje De Buysser and Dr. Petra Lommens for guiding me in my Ph.D research work and the time they had spent for providing useful comments for my journal publications.

The help provided by Dr. Els Bruneel with the analysis of XPS data is unforgettable and it was a joy working with her. I would like to thank my dear colleagues Thuy, Marcos, Nigel, Jonas, Pieter, Melis, Jian, Veerle, Danny, Iwein and Mieke with whom working together in the lab was exciting and fun-filled. Although I could spent very less time with my newer colleagues Glenn, Kenny, Tom, Koen and Katrien, it was nice to come in contact with all of them.

Getting assistance with administrative related things from Claudine and Pierre was always a fun and their bubbling response is appreciable. My sincere appreciation to Danny, Tom, Bart, Philip, Nico, Olivier for providing me with all technical related assistance and Pat for his support with IT.

I express my gratitude to Zenergy Power GmbH for providing Ni-5%W tapes and for depositing CSD-YBCO on my samples. I thank Dr. Ruben Hühne from IFW Dresden for

depositing YBCO and performing J_c tests on my samples. I also thank Dr. Leopoldo Molina and Prof. Dr. Gustaaf Van Tendeloo from University of Antwerp conducting TEM measurements on my samples.

My gratitude also goes to all the members of the examination committee, Prof. Dr. Isabel Van Driessche (UGent), Prof. Dr. Em. Serge Hoste (UGent), Prof. Dr. Katrien Strubbe (UGent), Prof. Dr. Klaartje De Buysser (UGent), Dr. Petra Lommens (UGent), Dr. Oliver Stadel (Percotech), Prof. Dr. Stephanie Lambert (ULiège), Prof. Dr. Mieke ADriaens (UGent) for their efforts in reading my thesis and giving their precious suggestions and comments.

I would like to thank all the educational and administrative personnel of S3 whose contact have been highly useful both directly and indirectly. I thank Ghent University, Belspo and the commission of the European Union in providing me monetary support during the tenure of my Ph.D.

It was fun working together and supervising Ayse and Guillermo as a part of their bachelor thesis and Sigelinde as part of her master thesis. I fondly remember you all. It is also good to remember that my proposal of the acronym ‘SCRIPTS’ was considered to be the name for the lab.

My heartfelt thanks to the Indian fraternity in Ghent whose contact and support were useful in every bit. My deepest gratitude to my special set of well wishers during the times of necessity. I thank all those indirectly related persons whose contribution in the various forms have helped me. And finally words do fall short when thanking my ever-loving parents and brother for their unconditional support and relentless wishes for my well-being. I can only thank almighty for all the above blessings.

Ghent, April 2012
Vyshnavi Narayanan

Dedicated to my parents

TABLE OF CONTENTS

Table of contents

Introduction and motivation

The high-temperature ceramic superconductor $YBa_2Cu_3O_{7-x}$ (YBCO) has an orthorhombic crystal structure consisting of three superimposed similar pseudo-perovskite cells. The CuO_2 planes, which contain two thirds of the Cu ions, are responsible for the transport of the Cooper pairs, while the CuO chains act as a charge reservoir. The variable oxygen content of the one dimensional chains gives rise to a difference in electronic properties of the material in question. $YBCO_{6+x}$, for example, has a tetragonal lattice and is an insulator, whereas $YBCO_{7-x}$ has an orthorhombic lattice and is superconducting [1-3].

The orthorhombic structure causes a characteristic strong anisotropy in many of its fundamental and materials properties, especially in relation to the more important purpose of its technical application exhibiting high J_c at high magnetic fields [1-5]. Hence, the deposition of epitaxial YBCO films on biaxially textured technical Rolling Assisted Biaxially Textured Substrates (RABiTS substrates) leads to the formation of good quality second generation YBCO layers [6-9]. Suitable substrate materials, especially nickel-alloy, silver and copper substrates, steel are studied as possible alternatives [10-12].

For the RABiTS method the use of nickel-based substrates is beneficial. The main deciding factors are the thermal expansion of the substrate similar to that of YBCO (Ni = $13.4 \cdot 10^{-6}$ K^{-1} at T= 50°C), and high melting temperature (melting temperature of Ni = 1145°C) and excellent texturing. Ni has a cubic lattice structure with lattice parameter equal to 3.52 Å. The lattice mismatch of Ni to the YBCO a-axis is around 8.1% (based on an 'a' lattice constant of YBCO = 3.83 Å). This is essential for good epitaxial growth of the layer. The high crystallinity of the Ni substrate is obtained after several rolling steps and subsequent crystallization at high temperatures [8, 10]. Typical thicknesses of the substrates used are 50 microns-150 microns.
A disadvantage of Ni is the oxidation on the surface when treated under oxygen conditions and its weak mechanical properties. An alloy of Ni with W improves the mechanical properties of the material and the lattice parameter of Ni-5 at% W was found to be = 3.54 Å [13]. However, the

oxidation of the Ni-based substrates was envisaged to be essentially overcome by the use of buffer layers as a diffusion barrier between the Ni substrate and YBCO. For the successful deposition of epitaxial buffer layers and the to-be deposited YBCO layer, primarily a low lattice mismatch layer to that of the substrate and YBCO is preferred. Besides that, the main function of the buffer layer is to act as a diffusion barrier of nickel into the superconducting YBCO layer. Moreover, since the subsequent YBCO coating takes place under oxidizing conditions, it should constitute as a barrier against oxygen diffusion. This is because, the formation of NiO layer at the boundary surface, with a preferable (111) orientation hinders the epitaxial growth and the increased lattice mismatch causes peeling of the layer [14]. Buffer layers also should transmit the texture from the substrate to the YBCO layer and reduce the lattice mismatch to YBCO.

In the past 15 years, a large number of potential buffer materials for the realization of YBCO coated conductors have been studied: CeO_2[15-22], Gd_2O_3[23,24], Nd_2O_3[25], Tb_2O_3[26], Eu_2O_3[27], Ho_2O_3[28], Y_2O_3[29], $La_2Zr_2O_7$ [30-46], $Gd_2Zr_2O_7$ [47], $LaMnO_3$[48] and Y_2O_3-stabilized ZrO_2(YSZ) [49, 50]. Some doped layers including that of $(Ce_{1-x}\ Gd_x)_2O_3$[51], $(Eu_{1-x}\ Yb_x)_2O_3$[52], $(Gd_{1-x}\ Yb_x)_2O_3$and $(Gd_{1-x}\ Ho_x)_2O_3$ [53] have also been studied for optimizing the lattice-mismatch with that of the substrate and the to-be deposited YBCO layer. Others include that of conducting oxide buffer layers namely, $SrRuO_3$ and $LaNiO_3$ [54] and $La_{1-x}Sr_xMnO_3$ (LSMO). The double layer architecture of $CeO_2/La_2Zr_2O_7$/Ni-5%W which has replaced the traditional layers of $CeO_2/YSZ/Y_2O_3$/Ni-5%W for the simplicity and economic benefits of reduced number of layers, are recently considered as good buffer layers for YBCO growth. Earlier, the preferred buffer layer architecture was $CeO_2/YSZ/CeO_2$/Ni-5%W [50] and $CeO_2/YSZ/Y_2O_3$/Ni-5%W [55]. Currently, the buffer layer using $La_2Zr_2O_7$ is of great interest in simplifying the architecture and the first two layers of CeO_2/ YSZ and Y_2O_3/ YSZ by its replacement but retaining its efficiency.

In the following research work, chemical solution deposition (CSD) has been adopted for the preparation of these buffer layers using the double layer architecture of $CeO_2/La_2Zr_2O_7$/Ni-5%W. Since CSD employs a homogeneous distribution of metal ions in a solvent, the transfer of homogeneity from the as-deposited amorphous films to a crystalline film, can be ensured. Furthermore, CSD allows easy compositional adaptation and non-vacuum processing [44, 45]. Additionally, water-based CSD preparation was adopted as it offers additional benefits of

environmental friendliness, safe handling and cost reduction [44, 45, 56]. Firstly, water-based buffer layer preparation involves proper preparation of the substrate in order to obtain good wettability. This has been dealt in chapter 3. In the continuation of the previous research on water-based architectures of $CeO_2/La_2Zr_2O_7$/Ni-5%W, the unattainability of thicker $La_2Zr_2O_7$ [44, 45] has been dealt with use of polymers in this current research to increase the single layer thickness of $La_2Zr_2O_7$ [56]. This was necessary because thicker layers of 150 nm were found to be efficient in Ni penetration followed by YBCO deposition [56]. Moreover, multiple buffer layers added to interface diffusion showing ineffective prevention of Ni penetration. The thickness effect and interface reactions have been studied using XPS and analyzed and presented in chapters 4-6. In the second part of the work, doped buffer layers in line with the concept of single buffer layers to replace the double layers of $CeO_2/La_2Zr_2O_7$/Ni-5%W, have been explored. These layers were also prepared by using water as the main solvent for preparation of the precursor solution. These buffer layers are in lines with previously investigated and reported single, lattice matched buffer layers including that of $(Ce_{1-x}\ Gd_x)_2O_3$[51], $(Eu_{1-x}\ Yb_x)_2O_3$[52], $(Gd_{1-x}\ Yb_x)_2O_3$ [53] and $(Gd_{1-x}\ Ho_x)_2O_3$, $YBiO_3$, Gd^{3+} doped CeO_2, La^{3+} doped CeO_2 or Eu^{3+} doped Yb_2O_3 and non-stoichiometric $La_2Zr_2O_7$ [57-62]. These single buffer layers were prepared to decrease the double layer architecture to simpler single layer architecture. Here, La^{3+} doping in CeO_2 and $Ce^{3+/4+}$ doping in $La_2Zr_2O_7$ and non-stoichiometric $La_2Zr_2O_7$ have been prepared and investigated for their efficiency as possible single buffer layers for coated conductors in chapter 7.

References

[1] M. Cyrot, D. Pavuna, Introduction to superconductivity and high T_c-materials, World scientific (1992).

[2] V. Cloet. Synthesis and microstructure analysis of $La_2Zr_2O_7$ buffer layers for coated conductors, PhD thesis, Ghent University, 2010.

[3] V. Breit, P. Schweiss, R. Hauff, H. Wuhl, H. Claus, H. Rietschel, A. Erb and G. Muller, Phys. Rev. B 52 (1995) 15727-15730.

[4] J.L. Tallon, C. Bernhard, H. Shaked, R.L. Hitterman and J.D. Jorgensen, Phys. Rev. B 51 (1995) 12911-12914.

[5] K. Kitazawa, H. Takagi, K. Kishio, T. Hasegawa, S. Uchida, S. Tajima, S. Tanaka and K. Fueki, Physica C 153-155 (1988) 9-14.

[6] W. Buckel, Superconductivity: Fundamentals and Applications, VCH Verlag (1993).

[7] B. Holzapfel, L. Fernandez, F. Schindler, B. de Boer, N. Reger, J. Eickemeyer, P. Berber, IEEE Trans. Appl. Supercond. 11 (2001) 3872-3875.

[8] A. Goyal, D.P. Norton, J.D. Budai, M. Paranthaman, E.D. Specht, D.M. Kroeger, D.K. Christen, Q. He, B. Satffito, F.A. List, D.F. Lee, P.M. Martin, C.E. Klabunde, E. Hartfield and V.K. Sikka, Appl. Phys. Lett. 69 (1996) 1795-1797.

[9] D.P. Norton, A. Goyal, J.D. Budai, D.K. Christians D.M. Kroeger, E.D. Specht, Q. He, B. Satffito, M. Paranthaman, C.E. Klabunde, D.F. Lee, B.C. Sales and F.A. List, Science 274 (1996) 755-757.

[10] A. Goyal, D.P. Norton, D.K. Christians E.D. Specht, M. Paranthaman, D.M. Kroeger, J.D. Budai, Q. He, F.A. List, R. Feenstra, H.R. Kerchner, D.F. Lee, E. Hatfield, P.M. Martin, J. Mathis and C. Park, Appl. Supercond. 4 (1996) 403-427.

[11] T.J. Doi, T. Yuasa, T. Ozawa and K. Higashiyama: Advance in Superconductivity VII Springer-Verlag (1994).

[12] M. Jin, S. Han, T. Sung and K. No, Physica C 334 (2000) 243-248.

[13] Y. Xu and D. Shi: A Review of Coated Conductor Development. http://www.eng.uc.edu/ DSHI ~ / News / Review% 20of% 20Coated% 20Cond.pdf.

[14] D.P. Norton, C. Park, C. Prouteau, D.K. Christians M.F. Chisholm, J.D. Budai, S.J. Pennycook, A. Goyal, E.Y. Sun, D.F. Lee, D.M. Kroeger, E. Specht, M. Paranthaman and N.D. Browning, Mat Sci. Eng. B-Solid 56 (1998) 86-94.

[15] E. Celik, J. Schwartz, E. Avci, H.J. Schneider-Muntau and Y.S. Hascicek, IEEE Trans. Appl. Supercond. 9 (1999) 2264-2267.

[16] I. Van Driessche, G. Penneman, J.S. Abell, E. Bruneel and S. Hoste, Mater. Sci. Forum 426 (2003) 3517-3522.

[17] M.S. Bhuiyan, M.P. Paranthaman, S. Sathyamurthy, T. Aytug, S. Kang, DF Lee, A. Goyal, E.A. Payzant and K. Salama, Supercond. Sci. Tech. 16 (2003) 1305-1309.

[18] Y. Akin, E. Celik, W. Sigmund and Y.S. Hascicek, IEEE Trans. Appl. Supercond. 13 (2003) 2563-2566.

[19] S. Morlens, L. Ortega, B. Rousseau, S. Phoke, JL Deschanvre, P. and Chaudouët, P. Odier, Mat Sci. Eng. B-Solid 104 (2003) 185-191.

[20] Y. Takahashi, Y. Aoki, T. Hasegawa, T. Watanabe, T. Maeda, T. Honjo, and Y. Shiohara, Physica C 392-396 (2003) 887-894.

[21] N. Van de Velde, D. Van de Vyver, O. Brunkahl, S. Hoste, E. Bruneel, I. Van Driessche, Eur. J. Inorg. Chem. 2010(2) (2010) 233-241.

[22] S. Chen, S.S. Wang, K. Shi, Q. Liu and Z. Han, Physica C 419 (2005) 7-12.

[23] T. Aytug, M.P. Paranthaman, B.W.W. Kang, D.B. Beach, S. Sathyamurthy, E.D. Specht, D.F. Lee, R. Feenstra, A. Goyal, D.M. Kroeger, K.J. Leonard, P.M. Martin and D.K. Christians, J. Am. Ceram. Soc. 86 (2003) 257-265.

[24] IH Mutlu, Z. Aslanoglu, MI El-Kawni, E. Celik, H. Okuyucu, Y. Akin, W. Sigmouth and Y. S. Hascicek, AIP Conference Proceedings 614 (2002) 589-594.

[25] E. Celik and Y.S. Hascicek, Mat Sci. Eng. B-Solid 106 (2004) 1-5.

[26] E. Celik and Y.S. Hascicek, Mat Sci. Eng. B-Solid 96, (2002) 300-306.

[27] Y. Akin, Z.K. Heiba, W. Sigmund and Y.S. Hascicek, Solid-State Electronics 47 (2003) 2171-2175.

[28] M.S. Bhuiyan, M. Paranthaman, S. Kang, D.F. Lee and K. Salama, Physica C 422 (2005) 95-101.

[29] H. Okuyucu, L. Arda, Y. Akin, Z.K. Heiba, Z. Aslanoglu and Y.S. Hascicek, IEEE Trans. Appl. Supercond. 13 (2003) 2680-2683.

[30] T.G. Chirayil, M.P. Paranthaman, D.B. Beach, D.F. Lee, A. Goyal, R.K. Williams, X. Cui, D.M. Kroeger, R. Feenstra, D.T. Verebelyi, D.K. Christen, Phys. C Superconductivity 336 (2000) 63-69.

[31] M.P. Paranthaman, S. Sathyamurthy, L. Heatherly, P.M. Martin, A. Goyal, T. Kodenkandath, X. Li, C.L.H. Thieme, M.W. Rupich, Phys. C Superconductivity 445-448 (2006) 529-532.

[32] S. Sathyamurthy, M.P Paranthaman, H.Y. Zhai, S. Kang, H. M. Christen, C. Cantoni, A. Goyal, P.M. Martin, IEEE Trans. Appl. Supercond. 13 (2003) 2658-2660.

[33] L.L. Ying, Z.Y. Liu, Y.M. Lu, B. Gao, F. Fan, J.L. Liu, C.B. Cai, T. Thersleff, S. Engel, R. Hühne, B. Holzapfel, Phys. C Superconductivity 469 (2009) 288-292.

[34] M.P. Paranthaman, S. Sathyamurthy, M.S. Bhuiyan, A. Goyal, T. Kodenkandath, X. Li, W. Zhang, C.L.H. Thieme, U. Schoop, D.T. Verebelyi, M.W. Rupich, IEEE Trans. Appl. Supercond. 15 (2005) 2632-2634.

[35] H.S. Chen, R.V. Kumar, B.A. Glowacki, Mater. Chem. Phys. 122 (2010) 305-310.

[36] Z. Yu, P. Odier, S. Morlens, P. Chaudouët, M. Bacia, L. Zhou, P. Zhang, L. Jin, C. Li, P. David, O. Fruchart, Y. Lu, J. Sol-Gel Sci. Technol. 54 (2010) 363-370.

[37] Y. Wang, L. Zhou, Y. Lu, C. Li, Z. Yu, J. Li, L. Jin, Y. Zhang, Y. Shen, J. Mater. Sci.-Mater. El. 22 (2011) 474-480.

[38] T. Caroff, S. Morlens, A. Abrutis, M. Decroux, P. Chaudouët, L. Porcar, Z. Saltyte, C. Jiménez, P. Odier, F. Weiss, Superconductor. Sci. Technol. 21 (2008) 075007

[39] K. Knoth, R. Hühne, S. Oswald, L. Schultz, B. Holzapfel, Superconductor Sci. Technol. 18 (2005) 334-339.

[40] K. Knoth, R. Hühne, S. Oswald, L. Schultz, B. Holzapfel, Acta Mater. 55 (2007) 517-529

[41] M.P. Paranthaman, S. Sathyamurthy, M.S. Bhuiyan, P.M. Martin, T. Aytug, K. Kim, M. Fayek, K.J. Leonard, J. Li, A. Goyal, T. Kodenkandath, X. Li, W. Zhang, M.W. Rupich, IEEE Trans. Appl. Supercond. 17 (2007) 3332-3335.

[42] K. Knoth, PhD Thesis (2006) "Chemisch abgeschiedene Lanthanzirkonatpufferschichten auf technischen Substraten zur Realisierung von Yttriumbariumkupferoxidbandleitern".

[43] T. Caroff, L. Porcar, P. Chaudouët, A. Abrutis, C. Jiménez, P. Odier, F. Weiss, IEEE Trans. Appl. Supercond. 19 (2009) 3184-3187.

[44] V. Cloet, J. Feys, R. Hühne, S. Hoste, I. Van Driessche, J. Solid State Chem. 182 (2009) 37-42.

[45] V. Cloet, P. Lommens, R. Hühne, K. De Buysser, S. Hoste, I. Van Driessche, J. Cryst. Growth 325 (2011) 68-75.

[46] M.S. Bhuiyan, M.P. Paranthaman, K. Salama, Superconductor. Sci. Technol. 19 (2006) R1-R21.

[47] Y. X. Zhou, X. Zhang, H. Fang, P. T. Putman, and K. Salama, IEEE Trans. Appl. Supercond. 15 (2005) 2711-2714.

[48] F.F. Lange, C.-H. Kim, S. Fillery, S. Buzzi, A. Goyal and P. Clem, Superconductivity for Electric Systems 2004 Annual Peer Review. Washington, USA, 27-29. July 2004

[49] Y. Akin, Z. Aslanoglu, E. Celik, W. Sigmund and Y.S. Hascicek, IEEE Trans. Appl. Supercond. 13 (2003) 2673-2676.

[50] H. Jarzina, S. Sievers, C. Jooss, H.C. Freyhardt, P. Lobinger and H.W. Roesky, Supercond. Sci. Tech. 18 (2005) 260-263.

[51] Y. Takahashi, Y. Aoki, T. Hasegawa, T. Watanabe, T. Maeda, T. Honjo, and Y. Shiohara, Physica C 392-396 (2003) 887-894.

[52] Y. Akin, Z.K. Heiba, W. Sigmund and Y.S. Hascicek, Solid-State Electronics 47 (2003) 2171-2175.

[53] H. Okuyucu, L. Arda, Y. Akin, Z.K. Heiba, Z. Aslanoglu and Y.S. Hascicek, IEEE Trans. Appl. Supercond. 13 (2003) 2680-2683.

[54] T. Aytug, B.W. Kang, C. Cantoni, E.D. Specht, M. Paranthaman, A. Goyal, D.K. Christians, D.T. Verebélyi, J.Z. Wu, R.E. Ericson, C.L. Thomas, C.-Y. Yang and S.E. Babcock, J. Mater. Res 16 (2001), 2661-2669.

[55] Y. X. Zhou, X. Zhang, H. Fang, P. T. Putman, and K. Salama, IEEE Trans. Appl. Supercond. 15 (2005) 2711-2714.

[56] V. Narayanan, P. Lommens, K. De Buysser, R. Hühne, I. Van Driessche, J. Solid State Chem. 184 (2011) 184, 2887-2897.

[57] G. Li, M.H. Pu, X.H. Du, R.P. Sun, H. Zhang, Y. Zhao Physica C 463 (2007) 589-593.

[58] K. Chiba, **S.** Makino, M. Mukaida, M. Kusunoki, **S.** Ohshima IEEE Trans. Appl. Supercond. 1 (2001) R1-R4.

[59] Y. Takahashi, Y. Aoki, T. Hasegawa, T. Maeda, T. Honjo, Y. Yamada, Y. Shiohara, Physica C 412 (2004) 905-910.

[60] D. Chambonnet , D. Keller, C. Belouet, Physica C 302 (1998) 198-204.

[61] L. Arda, Z.K. Heiba, Thin Solid Films 518 (2010) 3345-3353.

[62] M.P. Paranthaman, S. Sathyamurthy, X. Li, E.D. Specht, S.H. Wee, C. Cantoni, A. Goyal, M.W. Rupich, Physica C 470 (2010) 352-355.

Chapter-1

Introduction: Coated Conductors

This chapter describes the history of superconductivity and that of the high temperature superconductors. The coated conductor design for preparation of high temperature superconductors is described.

1.1 Superconductivity: Basic concepts

The discovery of superconductors by Kammerlingh Onnes in the year 1911was marked by the drop down of resistance in mercury to zero ohms at a temperature of 4 K. This phenomenon termed as 'Superconductivity' is displayed by some materials when they are cooled below a transition temperature known as critical temperature (T_c). Below T_c, superconducting materials exhibit two characteristic properties: (1) loss of the electric resistance and (2) active expulsion of the applied magnetic field (the Meissner effect) [1].

After this initial discovery of superconductivity in mercury at 4.2 K, search for new superconducting materials with higher T_c went on. One of those initial materials with high T_c was Nb_3Ge that displayed superconductivity at 23K [2]. These superconducting materials, considering its relative low T_c, are named superconductors of low critical temperature (LTSC). A theory developed by J. Bardeen, L. Cooper and J. Schrieffer (BCS) has been very successful in describing LTSC, assuming that electrons are coupled via electron-phonon interaction to form Cooper pairs [1-3]. Thirty years later, a mixed valence oxide of lanthanum, barium and copper discovered by Bednorz and Müller [4] exhibited zero resistance at a remarkably higher T_c of 35K that paved the path to a revolutionary higher transition temperature, leading to the present generation of high temperature superconductors (HTSC).

This was followed by the discovery of the '123' class of materials in 1987, marked especially by $YBa_2Cu_3O_{7-\delta}$ (YBCO), which showed an even higher T_c ~90K [5]. YBCO, being the first material with a critical temperature above liquid nitrogen temperature, provided hope for the reduction in the cost of cryogenics involved - a fact that could facilitate the technological application of superconducting materials. Subsequently, several compounds with T_c above 92K were found, $Bi_2Sr_2Ca_2Cu_3O_{10}$ (120K) [6], $Tl_2Ba_2Ca_2Cu_3O_{10}$ (127K) and $HgBa_2Ca_2Cu_3O_x$ (134 K) [7]. In HTSC, in contrast to LTSC, the phenomenon of superconductivity could not be explained by the conventional BCS theory. Many theories have been proposed but they still remain open for further discussions [8, 9]. The discovery of HTSC materials has led to the intense research activities on the use of superconductors in technological applications, including transmission cables, motors, generators, transformers and fault current limiters [10, 11]. The evolution of T_c as a function of time is displayed in figure 1.1.

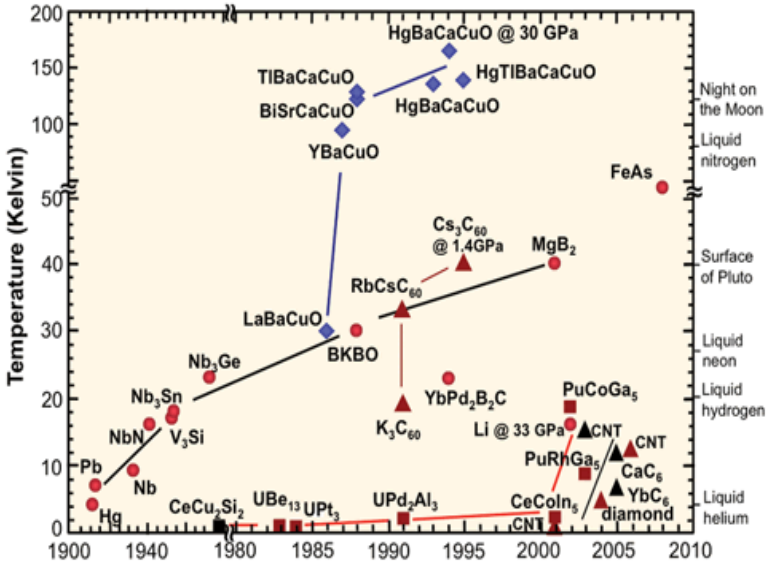

Figure 1.1: Evolution of T_c in the course of last century Courtesy: U.S. Department of Energy, www.ccas-web.org/superconductivity.

1.2 Structural properties of $YBa_2Cu_3O_{7-\delta}$

The orthorhombic YBCO structure has a pseudo-perovskite crystal lattice with Cu-O planes lying normal to the crystallographic c-direction. This structure is commonly found in all cuprates. Fig. 1.2 shows a sketch of the unit cell of the YBCO structure. The Cu-O planes are separated by charge-reservoir interleaved layers. This allows a change in the carrier density available in the Cu-O planes which compensates for the positive charge carrier density. These interleaved layers contain Cu-O chains in the b direction which contain free carriers and contribute to the normal conductivity. Therefore, the current that can flow parallel to the Cu-O planes (a-b planes) is much higher than the current flowing through the c - axis. Hence, the current flow should be carried out through the a-b plane direction in order to get a maximum current density. The critical current density, J_c, is then defined by the maximum current that these materials can carry without dissipation. In fact, all cuprates have this anisotropic layered structure which creates restrictions on their properties. As explained further in paragraph 1.2, YBCO properties are optimal in superconducting films with a c-axis orientation perpendicular to the substrate, so that high currents can be applied along the a-b planes.

YBCO essentially consists of three units namely, $BaCuO_3$, $YCuO_2$, and CuO_2. These three pseudo-perovskite units stack vertically form the superconducting unit cell with some oxygen vacant sites. In fact, the oxygen content will determine its crystallographic structure and the mobile charge carrier concentration in the Cu-O planes. The formula in the standard notation of YBCO is YBa_2Cu_3Ox where x denotes the variable oxygen content ranging from x = 6-7. The $YBa_2Cu_3O_{6+\delta}$ compound has a tetragonal structure and is an insulator. Increasing the oxygen content up to x = 6.6, represented as $YBa_2Cu_3O_{7-\delta}$, the compound changes from a tetragonal phase to an orthorhombic phase. The orthorhombic phase of YBCO is superconducting, with the highest T_c of 92 K at an oxygen content of 6.97.

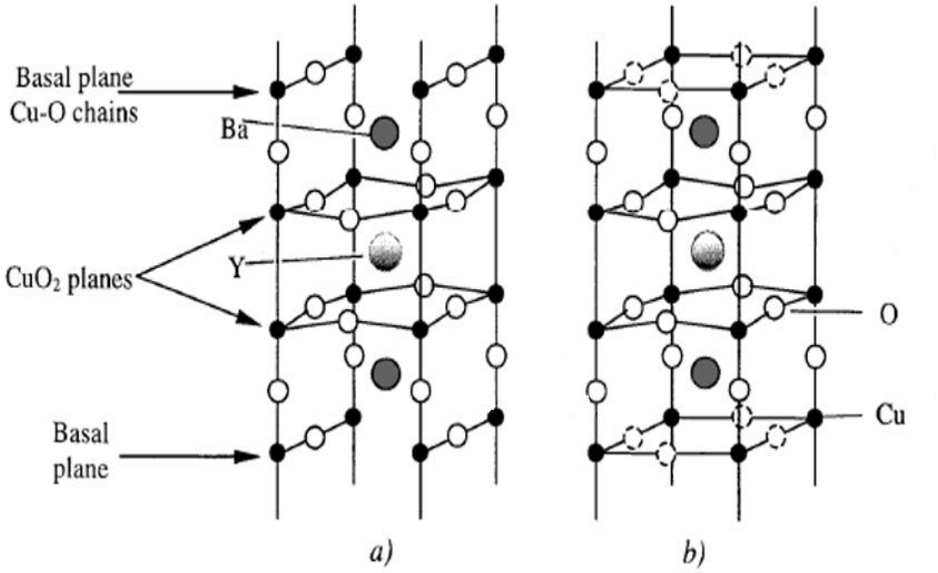

Figure. 1.2: Structure of $YBa_2Cu_3O_{7-\delta}$ [12, 13]

1.3 Physical properties of $YBa_2Cu_3O_{7-\delta}$

Two types of superconductors based on the transition in magnetic properties and the superconducting transition temperatures properties, can be distinguished. In a weak external magnetic field below the superconducting transition temperature T_c, magnetic flux is expelled from the interior of the superconductor termed as Meissner effect [12]. In a type I superconductor, a sharp transition from the superconducting to the normal state occurs. In type II, a gradual transition from the superconducting to the normal state can be observed [1]. In comparison to the sharp transition

of a Type-I superconductor, Fig. 1.3(a), a type II superconductor has two critical magnetic fields. Above the lower critical magnetic field, $H_{c1}(T)$, the magnetic flux from the external field is no longer completely expelled, and the superconductor exists in a mixed state. In a type I superconductor only the Meissner phase exists. A magnetic field penetrates into the superconductor only near the surface and the magnetic field in the core is zero. The type II superconductors can have either Meissner or the Shubnikov phase. In the Shubnikov phase some magnetic flux goes deep into the superconductor. This is energetic favorable, because the penetration length (λ_{GL}) is higher than the coherence length (ξ_{GL}) of the Cooper pair density. The concentration of cooper pairs can change easier at short distances than the magnetic field. For technical applications only a type II "hard" superconductor can be used. "Hard" means, that the magnetic flux, which penetrates the superconductors is pinned. If the magnetic flux is not pinned, the flux is moving in the superconductor, which results in an electrical field. If the magnetic flux is effectively pinned high currents can flow in the superconductor without resistance.

Above the higher critical magnetic field, H_{c2} (T), the superconductivity is completely destroyed, and the material exists in a normal state, see Fig. 1.3 (b).

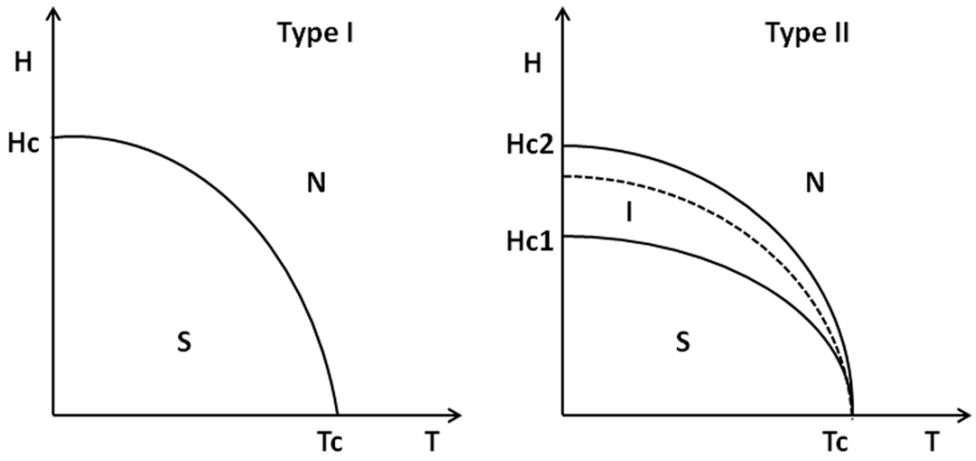

Figure.1.3: Superconducting phase transition diagram based on the magnetic field for type I (a) and type II (b) superconductors [12]

YBCO is a potential candidate for future technical superconducting applications where they exhibit their ability to carry high bulk super current at magnetic fields that exceeds 100T. Fig. 1.4 represents the magnetic field-temperature (H-T) phase diagram for the three prominent superconductors namely, Nb_3Ti, Nb_3Sn and $Bi_2Ca_2Cu_2O_3$ (Bi-2223)) and that of the second generation YBCO and the third generation MgB_2 conductor materials. As a comparison between the most prevalent first generation superconductor BSCCO and that of YBCO, there is a large difference between H_{irr} and H_{c2} of BSCCO. This makes it not favorable for employing BSCCO at high temperature (77 K) and at high fields. However, YBCO does not suffer from this problem which renders YBCO a more versatile and interesting superconductor for practical applications. These different phase diagrams have been attributed to their structural anisotropy. Anisotropy has described by the parameter γ, has values of 1 for Nb-Ti, 7 for YBCO and 50-200 for Bi-2223 [15]. The Strongly anisotropic Bi-2223 material exhibits an enormous suppression of H_{irr} (77K) to a very low value of 0.3T. In practice high temperature superconductors are limited by the irreversibility field, H_{irr}, above which magnetic vortices melt or decouple. This irreversibility field prevents the use of Bi-2223 at higher critical temperatures of 77K in high magnetic field applications for motors and magnets. This is an added advantage for developing a second generation HTSC technology based on YBCO, for which H (77K) ~7T.

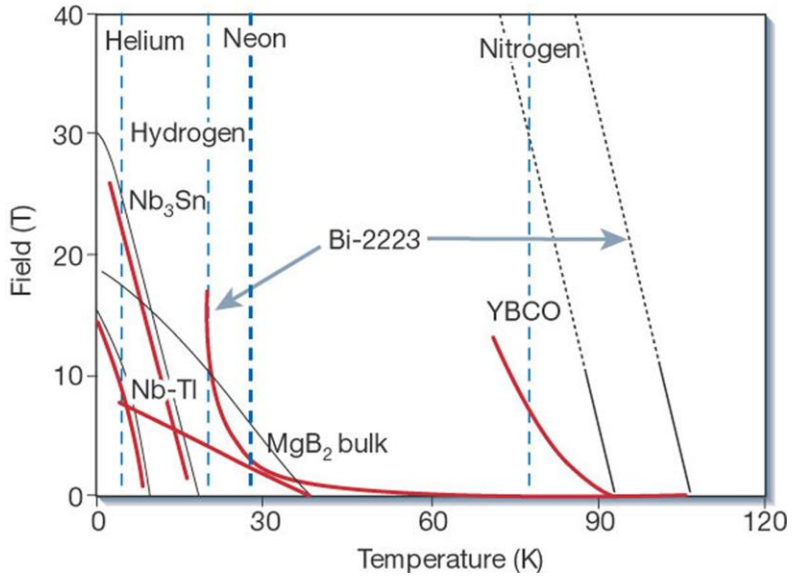

Figure 1.4: Magnetic field-temperature diagram for type II superconductors [10].

1.4 Coated conductors: Design and development

Given the anisotropy in the structure of HTSC (sec. 1.2) and their ceramic mechanical properties that are brittle and hard in intrinsic nature, HTSC cannot be used as such (in bulk) for practical applications. To ensure c-axis orientation, and thus a high critical current density, in combination with improved mechanical properties, thin layers of HTSC will be deposited on metallic substrates leading to the so-called coated conductors. Looking at the history of long-length superconductors, there are two basic architectures for HTSC wires, a multifilamentary or first generation conductor (1G) based on Bi-series in a silver tube [16] and a coated conductor (CC) or second-generation conductor (2G) based on YBCO on flexible tapes [17] (Fig. 1.5). Both categories serve their purpose within their limits. The manufacturing process and the design also restrict their end-product utility. The fabrication process, stress encountered in the material, etc are also some of the crucial parameters in the materials' manufacturing. First generation high temperature superconductors (1G HTSC) are multi-filamentary composite wires made of bismuth based material, such as Bi-2212 or Bi-2223 in a silver or an alloy matrix, that are pressed into a tape by rolling. The so-called (oxide-) powder-in-tube technique ((O)PIT) an silver(-alloy) tube is packed with the HTS powder [13, 18]. Silver or an alloy is chosen as a template material because it is non-reactive with the powder material, resilient to mechanical deformations, permeable to oxygen and the silver interface tends to promote the *c*-axis growth of the Bi-based grains. The filled Ag tube undergoes deformation processes to be converted into a mono-filamentary wire. These single filament HTSC wires are then restacked in a silver(-alloy) tube, drawn into a wire, pressed into a tape and heat treated at 800 - 900 °C in an O_2 atmosphere to form an oxide superconducting material.

The new second generation of superconductors (2G HTSC), otherwise known as the coated conductors or 'CC', generally consist of a flexible metal substrate, one or more buffer layers and a superconducting layer. As a substrate, biaxially textured, alloyed **R**olling **A**ssisted **Bi**axially **T**extured **S**ubstrates (RABiTS), especially using nickel-alloys is commonly used as the metal substrate for the CC.

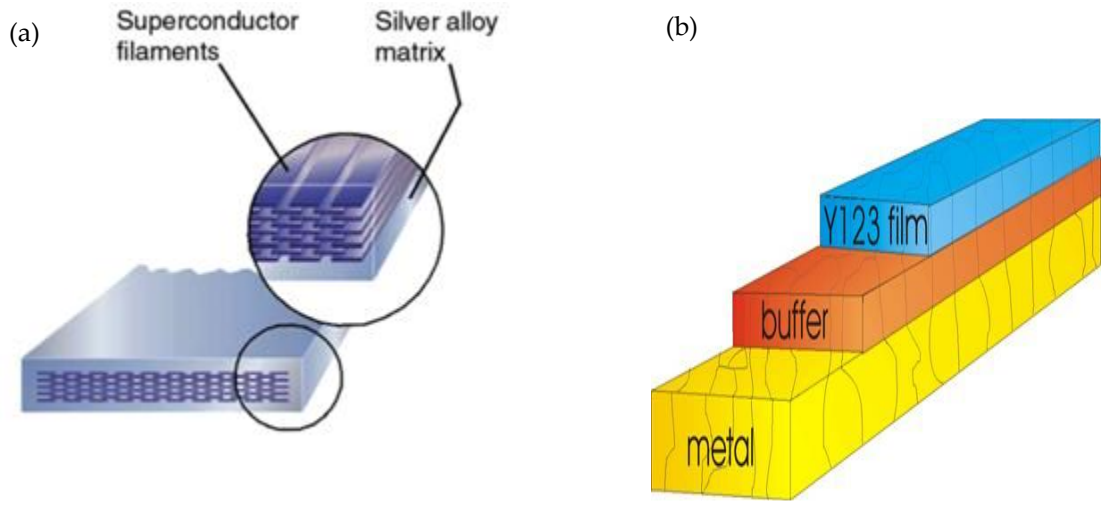

Figure 1.5: (a) First-generation superconductive wire based on Bi-2223 superconductive filaments in a silver matrix and (b) Second-generation (2G) YBCO-coated conductor [21].

Another technique for making coated conductors is based on Ion beam assisted deposition (IBAD) and inclined substrate deposition (ISD). They both differ from the RABiTS process in that the buffer layers are textured because of the deposition technique on the substrate (e.g. stainless steel, hastelloy, inconel, etc). The in-plane texture of the developing film is controlled by means of an ion bombardment. In surface oxidation epitaxy or self oxidation epitaxy (SOE), a biaxially textured oxide phase is grown on a RABiTS substrate [14, 22]. More details on substrate development will be given in sec. 1.6.

Early investigations on HTSC materials revealed the possibility to grow oriented YBCO layers on these flexible and buffered substrates which showed good J_c at 77 K. However, the grain boundaries can restrict the J_c by inducing structural disorder and thereby blocking any further transport of current across the grain boundaries. It was found that J_c has been shown to decrease exponentially with the misorientation angle between adjacent grain orientation θ. This high sensitivity to misorientation and the inherent anisotropy of the HTSC compounds, summons the situation to possibly grow long length of superconductors in optimal conditions and also the crucial need of joining of the superconductor [23].

1.5 Epitaxy and lattice mismatch

Two types of epitaxy can be recognized based on the nature of film and substrate as well as the lattice matching between them. Homoepitaxy is the occurrence of epitaxial growth wherein the film and substrate are from the same material. The second type of epitaxy is known as heteroepitaxy and occurs when films and substrates are composed of different materials. Heteroepitaxy is the common phenomenon for layers grown on polycrystalline substrates and the YBCO coated conductors are based on heteroepitaxial film structures. The lattice mismatch strain ε_m, experienced by the film is then calculated according to the relation [24]:

$$\varepsilon_m = (a_s - a_b)/a_b \quad (1.1)$$

where, a_b is the bulk lattice parameter of the film material and a_s is the lattice parameter of the substrate. Since the film grown on top of the substrate accommodates the lattice mismatch, the strain that is experienced by the layer can be calculated from the equation. In heteroepitaxy the lattice parameters are necessarily unmatched, and depending on the extent of the mismatch ε_m, we can envisage the following distinct epitaxial regimes:

If the lattice mismatch is very small, then the heterojunction interfacial structure is essentially like that for homoepitaxy. However, differences in film and substrate chemistry and coefficient of thermal expansion can strongly influence the electronic properties and perfection of the interface. When the film and substrate lattice parameters differ more substantially, we can expect an occurrence of dislocation defects at the interface. It usually occurs between film-substrate pairs composed of dissimilar materials which have the same crystal structure. The theory predicts that any epitaxial layer having a lattice-parameter mismatch with the substrate of less than ~ 9% would grow pseudomorphically, i.e., initially, very thin films strain elastically to have the same interatomic spacing as the substrate, making the interface coherent with atoms on either side lining up. With increasing film thickness the rising total elastic strain energy will eventually exceed the energy associated with a relaxed structure consisting of an array of misfit dislocations separated by wide regions of relatively good fit [25].

1.6 Coated conductor architectures

Substrate

In order to avoid any chemical interaction between the metal substrate and the oxide superconductor, and to minimize the lattice mismatch of the substrate, epitaxial buffer layers are necessary [21]. Today, there are mainly four different principal approaches for achieving long length textured coated conductor tapes which are currently being developed for commercialization by several industries worldwide. One substrate technology, called Rolling-Assisted Biaxially Textured Substrates (RABiTS), was invented by Oak Ridge [26], while another, ion-beam assisted deposition (IBAD) was pioneered by Fujikura [27] , later improved by the Los Alamos group [28].

The function of a buffer layer is twofold. Besides acting as a barrier against diffusion of Ni and O_2 between the metal substrate and the superconducting film, it is also required that the texture of the metal substrate is transferred to the superconductor [19-20]. The role of flexible substrates can be typically served by polycrystalline metals. Typically in RABiTS process based on a thermo-mechanical treatment of metallic substrates where the face centered cubic metals, e.g. Ni, are subjected to rolling along the (001) plane followed by annealing in vacuum, the growth of cube texture becomes more prominent [17]. Pure Ni is seldom used, instead alloyed nickel (mostly alloy element $\leq$ 5 at%W) is more favoured for industrial implementation because of its good mechanical strength, thermal stability and corrosion resistance properties. The texture of these substrates can then be transferred to the subsequent layers on top through epitaxial growth.

Alternative approaches to texture buffer layer/substrate combinations is through self-oxidation epitaxy (SOE) [29] or the so-called inclined substrate deposition (ISD) [30] where a single textured buffer layer is vacuum deposited on a flexible polycrystalline substrate and the texture is achieved as a consequence of the higher growth rate of a given crystallographic orientation. In Ion Beam Assisted Deposition (IBAD), an energetic ion beam irradiates the substrate at a particular angle during the deposition of an oxide buffer layer. These are typically, yttrium-stabilized zirconia (YSZ) [31], or MgO [32]) deposited onto a non textured metal tape (stainless steel, hastelloy or similar alloys). Additionally, some extra buffer layers can be grown between the IBAD-textured layer and the YBCO in order to enhance the

crystallographic orientation of YBCO. This process in comparison to RABiTS deposition is shown in Fig. 1.6. In this work, RABiTS Ni-5%W tape prepared by EViCO GmbH and supplied by Zenergy Power GmbH was used.

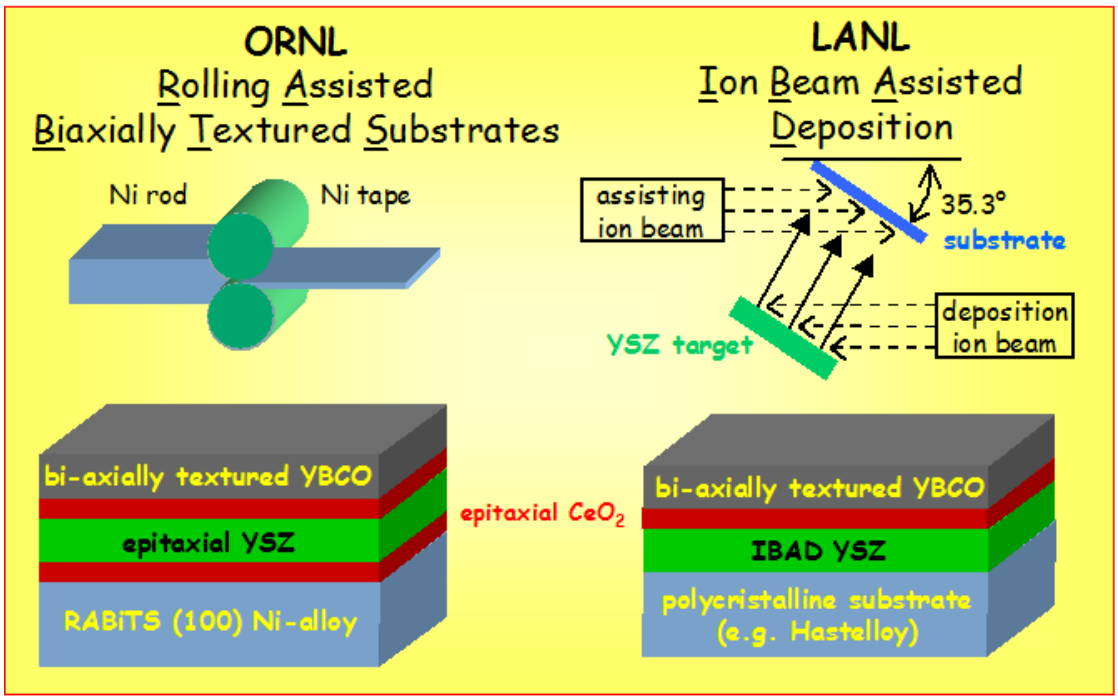

Figure1.6: Comparison sketch of the RABiTS and IBAD approach for the production of $YBa_2Cu_3O_{7-\delta}$ coated conductor [LANL website]

Buffer layer

Buffer layers play a key role in YBCO 2G wire technology wherein they transfer the biaxial texture from the substrate to the YBCO layer. In addition, dense buffer layers necessarily need to provide a good barrier for cation and oxygen diffusion. Apart from preventing the penetration of Ni into the YBCO which can otherwise destroy the superconducting properties, the control of oxygen diffusion is a second major function of the buffer layer. Another essential role of the buffer layer(s) is that, it should be chemically stable and nonreactive with the YBCO, nonporous and strongly bonding. Until this day, no single buffer layer material has been found that meets all of these needs, and great effort is being devoted to find a single buffer layer or simplified multi-layer architectures that function well, this is therefore also the ambition of this work.

Many materials have been proposed and demonstrated as buffer layer for YBCO films, but most have met with limited success [21]. In general, the search for a buffer layer that can support the growth of YBCO film has centered on materials having a fluorite-like structure (MX_2), a pyrochlore ($A_2B_2O_7$) crystal structure or a perovskite (ABO_3) structure. In this work we have focused on the study of pyrochlore and fluorite structures fabricated by chemical solution deposition (see following chapters 3-7).

Superconducting film

The superconducting material of choice here is c-axis oriented $YBa_2Cu_3O_{7-x}$. To obtain high critical current densities, the YBCO grains must be well aligned. The YBCO layer can generally be deposited by pulsed layer deposition (PLD), chemical solution deposition (CSD) or metal-organic chemical vapour deposition (MOCVD) and is processed under oxidizing conditions. A renewed water-based CSD approach was considered in this work.

Protective cap layer

The primary function of a protective layer (usually Ag or Au) is to provide mechanical protection against abrasion, wear and corrosion. A secondary, and perhaps more important, function is to redirect the J_c (~ 1 MA/cm² for a 1 μm thick film) in case of malfunctioning of the cooling system. As the dissipation of heat is proportional to the product of the resistance (0 Ω in the superconducting state) and the square of the current, the integrity of the material is at risk. This is because, the increase of resistance is exponential at the transition between superconducting state and normal conductivity. Therefore the dissipation energy is very high at the place, which possesses a little bit lower I_c. For applications the homogeneity of I_c is crucial.

1.7 Chemical solution methods of precursor preparation

Chemical solution deposition (CSD) is presently a well established field which has shown path for depositing materials of wide use with high performance such as nanoparticles, bulk ceramics, hybrid materials, mesoporous solids, coatings, etc. [33, 34]. This method has recently appeared as a low cost alternative for the fabrication of 2G coated conductors. The main advantage of this methodology is that low capital investment and supply costs are involved, thus it has become a competitive alternative to vacuum based depositions. Other advantages are the high degree of compositional control inherent with the solution synthesis of multi-element,

inorganic materials.

The main requirements that need to be fulfilled by the solution to be used in CSD are: (1) a stable coating solution,(2) precursors that decompose without undesirable residues during thermal processing (3) acceptable wetting of the substrate,(4) no crack formation or compositional non uniformities during pyrolysis or crystallization [35].

The general principle involved in the solution deposition is to prepare a homogeneous solution of the necessary cations that will be later applied to a substrate. The fabrication of thin films by this approach involves four basic steps (i) synthesis of the precursor solution, (ii) deposition by spin coating [36], spraying [37] dip-coating and ink-jet printing [14, 18] (iii) low-temperature heat treatment for drying, pyrolysis of organic species (typically 300-400ºC) and formation of an amorphous film, and (iv) a high temperature heat treatment for densification (typically 700-900ºC) and crystallization of the coated film to convert the precursor into the desired oxide phase.

A variety of precursor chemicals that include metal organic molecules, metal salts, and polymers can be heat-treated to obtain oxides at high temperatures. The requirements of appropriate solubility combined with heat-treatment that will result in a final oxide, needs careful choice of precursors. Usually, metal-organic compounds are suitable, due to the fact that their solubility in polar or non-polar solvents can be tuned by modifying the organic part of the molecule, and because the organic part pyrolyzes in oxidizing ambient atmosphere without residue [33, 38]. One of the most common precursors are metal salts that include carboxylates (M-(RCOO)x, where R represents an alkyl group) which can normally be dissolved in their own (parent) carboxylic acids. For short alkyl chain salts, some solubility in water and other highly polar solvents is typically observed due to the polar nature of the salt. Alkoxides $(M\text{-}OR)_x$, β-diketonates (organic molecules with two keto groups separated by one methylene group ($-CH_2$)) and mixed ligand precursors are also frequently employed in CSD processing [35].

In addition to precursor properties, solvent choice is also an important consideration for control of film gelation and processing behaviour. The solvent used can determine the wettability of the solution on the substrate. The solvent should also possess desirably, high evaporation rate, can drive gelation and good surface tension characteristics which can dictate substrate wetting behaviour.

The various chemical routes utilized for thin film growth can be grouped into four principal categories :

- The most frequently used sol-gel process uses alkoxide precursors that undergo hydrolysis and polycondensation. This technique is primarily used for silica [39].
- The metal organic decomposition (MOD) routes that employ carboxylate precursors that do not undergo significant condensation reactions during either solution preparation or film deposition [35].
- In this thesis we have synthesized buffer layer films (LZO, doped CeO_2) by an inorganic metal-chelate route. According to Kakihana et al.[40], this metal-chelate structure reduces the free concentration of metal ions in the solution by forming water-soluble metal complexes. With variation of pH and metal concentration, gelation can occur upon the evaporation of the solvent [41]. These systems henceforth will be referred as, **inorganic metal-chelate systems.** This will be discussed in chapter 4.
- Hybrid routes that exhibit condensation reactions at several process stages. Frequently, this route has been used for preparation of multicomponent PZT oxide films. We have used this method in combination with complexants for preparing **inorganic hybrid metal-chelate systems** for developing LZO, Ce doped LZO and non-stoichiometric LZO thin films [42].

The basic approach used here consists of dissolving inorganic metal salts (acetates, nitrates) in a common solvent (here, water), and restricting the free metal ion concentration by adding suitable complexants and combining the solutions to yield the desired stoichiometry. With variation of pH and metal concentration, gelation can occur upon the evaporation of the solvent. These systems henceforth will be referred as, **inorganic metal-chelate systems.** Additional organic components like EDA, EG play their role in these systems which will be discussed in the following sections.

With a small variation, including one metal salt and one metal alkoxide for a multi component metal oxide, the above said **inorganic metal-chelate systems** can be changed to an **inorganic hybrid metal-chelate systems**. In these systems, first, the large organic ligands may cause cracking during thin film processing due to the excessive weight loss and shrinkage that can occur. To circumvent this, control of solution concentration and thermal processing is

required. Alternatively, short chain carboxylate (e.g., acetate, propionate) and strongly chelating β-diketonate (e.g., acetylacetonate acac-type) compounds can be used. The use of chelating ligands such as EDTA can lead to the formation of monomeric compounds and the lower organic content of the precursors reduces film shrinkage after deposition, decreasing problems with film cracking.

This work focuses on water-based metal-chelate systems which have been used earlier in other sytems [14, 18, 43, 44]. They resulted in stable solutions which are cost effective and environmentally friendly.

In this work LZO, doped LZO, varied stoichiometeric LZO and doped CeO_2 and buffer layers have been prepared by this route and its detailed synthesis are described in chapter 4.

1.8 Coating techniques

Once the precursor solution has been prepared, films from these solutions can be deposited on the substrate by dip-coating, spin-coating, ink-jet printing, slot-die coating or spraying.Excess solvent is removed during coating forms a solid or gel precursor film. At the laboratory scale, deposition is usually achieved with a dip-coater and the substrate is typically a poly crystalline RABiTS Ni-5%W substrate. The substrate is held in place on the dip-coater (under clean-room conditions) and dip-coated at various withdrawal speeds. The higher the withdrawal speed, more material is deposited and results in thicker films. But, thicker films can finally be cracked once the critical thickness is reached. The thickness of the layer is controlled by the precursor solution characteristics, such as concentration and viscosity. The attributing factors contributing to the layer thickness is based on Landau-Levich equation (Eq. 1.2).

$$h = \frac{0.94(\eta U_0)^{2/3}}{\gamma^{1/6} LV (\rho g)^{1/2}} \qquad (1.2)$$

where η is the viscosity of the solution (mPa s), U_0 is the withdrawal speed (mm/min), γ_{LV} is the liquid-vapor surface tension (N/m), ρ the density of the solution (kg/L) and g the standard acceleration due to gravity. A typical dip-coating set-up and the withdrawal process is shown in Fig. 1.7.

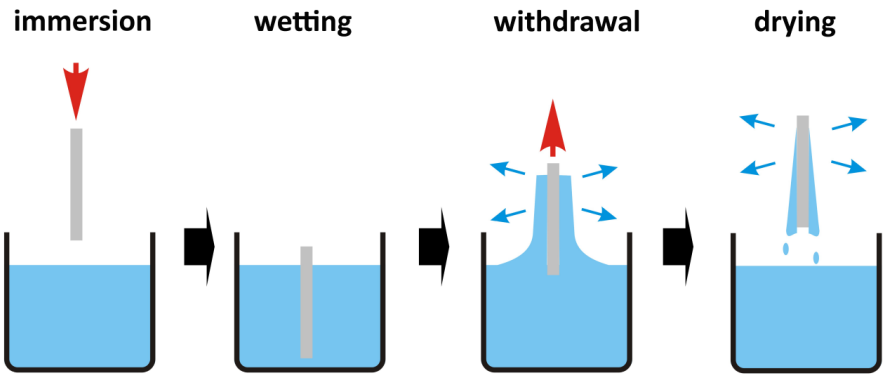

Figure 1.7: Depiction of dip-coating process [14]

To complete the transformation of the as-deposited film into the crystalline ceramics, they are heat-treated until very high temperatures to obtain the final metal-oxide phase. It is important to know the decomposition characteristics and the pathway by which the crystalline phase evolves because they can be dependent on the precursor chemistry employed, the material chemistry, heating rate and temperature. This can be studied by thermal analysis (TGA-DTA-DSC).

References

[1] J.R.Waldram, Superconductivity of Metals and Cuprates, Edited by Institut of Physics Publishing (1996).

[2] J.R.Gavaler, M.A.Janocko, and C.S.Jones, Appl. Phys. Lett. 23 (1973) 480-487.

[3] J.Bardeen, L.N.Cooper, and J.R.Schrieffer, Theory of Superconductivity, Physical Review 108, 1175 (1957).

[4] J.G. Bednorz and K.A. Müller, Zeitschrift fur Physik B-Condensed Matter 64 (1986) 189-193.

[5] M.K. Wu, J.R.Ashburn, C.J.Torng, P.H.Hor, R.L.Meng, L.Gao, Z.J.Huang, Y.Q.Wang and C.W. Chu, Phys. Rev. Letters 58 (1987) 908-912.

[6] D.C.Larbalestier, Power Applications of Superconductivity in Japan and Germany (World Technology and Engineering Center) , Loyola College, MD, September (1997).

[7] A. Schilling, M. Cantoni, J.D. Guo, and H.R.Ott, Nature 363 (1993) 56-63.

[8] F.Beech, S.Miraglia, A.Santoro, and R.S.Roth, Phys. Rev. B 35 (1987) 8778-8785.

[9] V.Breit, P.Schweiss, R. Hauff, H.Wühl, H. Claus, H. Rietschel, A.Erb, and G.Müller-Vogt, Phys. Rev. B 52 (1995) 15727-15735.

[10] D. Larbalestier, A. Gurevich, D.M. Feldmann and A. Polyanskii, Nature 414 (2001) 368-373.

[11] J. R. Hull, Reports on Progress in Physics, 66(11) (2003) 1865-1886.

[12] M. Cyrot, D. Pavuna, Introduction to superconductivity and high T_c-materials. World scientific (1992).

[13] J. Evetts. Concise encyclopedia of magnetic and superconducting materials. Advances in materials science and engineering. PergamonPress (1992).

[14] V. Cloet, "Synthesis and microstructure analysis of $La_2Zr_2O_7$ buffer layers for coated conductors", PhD Thesis, Ghent University (2010)

[15] G.Blatter, M.V.Feigelman, V.B.Geshkenbein, V.B.Larkin, and A.I.Vinkour, Rev. Mod. Phys. 66 (1994) 1125-1133.

[16] K.Heine, J.Tenbrink, and M.Thoner, Appl. Phys. Lett. 55 (1989) 2441-2443.

[17] A.Goyal, M.Paranthaman, and U.Schoop, Materials Research Bulletin 8 (2004) 552-555.

[18] J. Feys et al., J. Mat. Chem., 22 (9) (2012), 3717 – 3726.

[19] T.G. Chirayil, M. Paranthaman, D.B. Beach, D.F. Lee, A. Goyal, R.K. Williams, X. Cui, D.M. Kroeger, R. Feenstra, D.T. Verebelyi and D.K. Christen, Phys. C: Supercond., 336(1-2) (2000) 63-69.

[20] K. Knoth, R. Hühne, S. Oswald, L. Schultz, B. Holzapfel, Acta Materialia, 55(2) (2007) 517-529

[21] M.Paranthaman and T.Izumi, Materials Research Bulletin 8 (2004) 533-535.

[22] R. Hühne, D. Selbmann, J. Eickemeyer, J. Hänisch and B. Holzapfel., Supercond. Sci. Technol., 19(2) (2006) 169-174.

[23] D.Dimos, P.Chaudhari, J.Mannhart, and F.K.Legoues, Phys. Rev. Letters 61 (1988) 219-225.

[24] M.Ohring,"Materials Science of Thin Films, Deposition and structure" 2nd Edition, Academic Press, New York , 412-430 (2005).

[25] J.W. Matthews,"Coherent Interfaces and Misfit Dislocations" Ed. by J. W. Matthes, Academic Press , 559 (1975)

[26] A. Goyal, D.P.Norton, J.D.Budai, M.Paranthaman, E.D.Specht, D.M.Kroeger, D.K.Christen, Q.He, B.Saffian, F.A.List, D.F.Lee, P.M.Martin, C.E.Klabunde, E.Hartfield, and V.K.Sikka, Appl. Phys. Lett. 69 (1996) 1795-1783.

[27] Y.Iijima, N.Tanabe, O.Kohno, and Y.Ikeno, Appl. Phys. Lett. 60 (1992) 769-773.

[28] X.D.Wu, S.R.Foltyn, P.N.Arendt, W.R.Blumenthal, I.H.Campbell, J.D.Cotton, J.Y.Coulter, W.L.Hults, M.P.Maley, H.F.Safar, and J.L.Smith, Appl. Phys. Lett. 67 (1995) , 2397-2400.

[29] K. Matsumoto, K. Kim, K. Yamagiwa, Y. Koike, I.Hirabayashi, T.Watanabe, N.Uno, and M. Ikeda, Physica C 335 (2000) 39-45.

[30] M.C. Bau, “Chemical solution deposition of oxide buffer layers and superconducting layers for $YBa_2Cu_3O_7$ coated conductors”, PhD Thesis, Universitat Autonoma de Barcelona (2006).

[31] A. Usoskin, J. Dzick, A.Issaev, J. Knoke, F. Garcia-Moreno, K. Sturm, and H.C. Freyhardt, Supercond. Sci. & Techn. 14 (2001) 676-683.

[32] M.Varela, D.Arias, Z.Sefrioui, C.Leon, C.Ballesteros, and J.Santamaria, Phys. Rev.B 62 (2000) 12509-12515.

[33] C.Brinker and G.W.Scherer, Sol-Gel Science: The Physics and Chemistry of Sol-Gel Processing , New York (1990)

[34] J.D.Mackenzie and E.Bescher, J. Sol-Gel Sci. Technol. 27 (2003) 7-12.

[35] R.W.Schwartz, T.Schneller, and R.Waser, Comptes Rendus Chimie 7 (2004) 433-439.

[36] D.E.Bornside, C.W.Macosko, and L.E.Scriven, Journal of Imaging Technology 13 (1987) 122-125.

[37] S. Halder, "Preparation and characterization of barium-based perovskite dielectrics on different bottom electrodes by chemical solution deposition" PhD Thesis, RWTH-Aachen (2006).

[38] R.T.Morrison and R.N.Boyd, Organic Chemistry, 3rd Edition, Allyn and Bacon, Inc., Boston (1974)

[39] P.K.Coffman and S.K.Dey, J. Sol-Gel Sci. and Tech. 1 (1994) 251-255.

[40] M. Kakihana, Sol-gel Sci. and Tech. 6 (1996) 7-55.

[41] R.W.Schwartz, R.A.Assink, and T.J.Headley, Materials Research Society Symposium Proceeding 243 (1992) 245-254.

[42] M.Liu and D.Wang, J. Mater. Res. 10 (1995) 3210-3215.

[43] I. Van Driessche, G. Penneman, E. Bruneel, S. Hoste, Pure Appl. Chem. 74 (2002) 2101-2109.

[44] I. Van Driessche, S. Cattoir, S. Hoste, Appl. Supercond. 2 (1994) 101-110.

Chapter-2

Experimental techniques

This chapter describes the characterization techniques that were used to quantify the properties of the precursors and the finally obtained layers. Various instruments including that of XRD, SEM, XPS were used and their utility in characterization studies are described.

2.1 TGA-DTA

Thermal gravimetric analysis (TGA) measures the difference in weight changes in a material as a function of temperature (or time) in a controlled atmosphere. Simultaneously, the differential temperature analysis (DTA) is measured between the sample and a reference (a thermally inert substance-Al_2O_3). This observed temperature difference can be due to a difference in heat capacity between sample and reference [1, 2]. The resulting DTA and TGA curves are simultaneously plotted on a dual Y-axis graph so the DTA's fingerprint and the TGA's weight loss (gain) characteristics are directly compared as the tested sample is heated or cooled. The equipment used for this thesis was a SDT 2690 (TA instruments, Department of Inorganic and Physical Chemistry, UGent). It has been used for investigation of the thermal decomposition behavior of the gel network on bulk samples with the same composition as dip-coated layers.

2.2. X-Ray Diffraction

An ordered crystalline substance shows a characteristic pattern that can be observed using X-ray Diffraction (XRD) study [3]. The X-ray diffraction pattern of a pure substance is, therefore, like a fingerprint of the substance. The powder diffraction method is thus ideally suited for characterization and identification of polycrystalline phases [4, 5]. Today about 50,000 inorganic and 25,000 organic single components, crystalline phases, and diffraction patterns have been collected and stored as standards. The main use of powder diffraction is to identify components in a sample by a match procedure [4]. In this thesis, XRD was used for identification of different phases present in the LZO, Ce doped LZO, non stoichiometric LZO and CeO_2 layers. Measurements were collected on a Siemens D5000 diffractometer (Department of Inorganic and Physical Chemistry, UGent), using Cu-K_α radiation.

2.2.1 Theory of XRD

When an X-ray beam is incident on the planes of the crystal structures with an inter planar spacing 'd', (Fig. 2.1), incident rays make an angle θ (Theta) with these planes. A reflected beam of maximum intensity will result if the reflected waves are in phase. The difference in path length between incident and reflected beam must then be an integral number of wavelengths, λ (lambda).

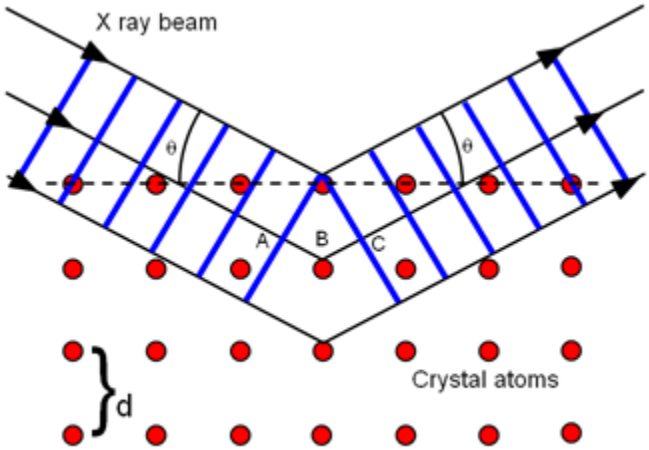

Figure 2. 1: Representation of Bragg's law

Courtesy: http://tap.iop.org/atoms/xray/530/page_47297.html

This can be expressed mathematically using Bragg's law as:

$$n\lambda = 2d.\sin\theta \qquad (2.1)$$

The process of reflection is described here in terms of incident and reflected (or diffracted) rays, each making an angle θ with a fixed crystal plane. Reflections occur from planes set at angle θ with respect to the incident beam and generates a reflected beam at an angle 2θ from incident beam. A Siemens D5000 instrument (Department of Solid State Sciences, UGent) was used to acquire the Bragg's reflection of the crystal planes of the buffer layers. Additionally using the same instrument the out-of-plane misalignment called the 'rocking curves' of the (0 0 4) LZO reflections or (0 0 2) LCO reflections of the buffer layers are acquired. These rocking curves determine the out-of-plane alignment of the LZO crystals or how much the LZO crystals are tilted away from the ideal c-axis orientation.

2.2.2 Pole-figures (for films)

The preferred orientation determination in a polycrystalline aggregate is carried-out using pole-figure texture analysis [6-10]. A pole figure is scanned by measuring the diffraction intensity of a given reflection (2-Theta is constant) at a large number of different angular orientations of the sample. A contour map of the intensity is then plotted as a function of angular orientations of the specimen. The most common representation of the pole-figures is a stereographic or an equal area projection. The intensity of a given reflection (h, k, l) is proportional to the number of (h, k, l) planes in reflecting conditions (Bragg's law). Hence, the pole-figures give the probability of finding a given crystal-plane-normal as function of specimen orientation. If the crystallites in the sample have a random orientation the recorded intensity will be uniform (Fig. 2.2). The pole-figures for use in this thesis were collected on a Bruker D8-Discover equipment (Department of Solid State Sciences, UGent). In order to identify the in-plane misalignment, phi-scans of the (2 2 2) LZO or (1 1 1) LCO reflections buffer layers are acquired using the same instrument. These scans determine the in-plane alignment of the LZO crystals along the c-axis orientation.

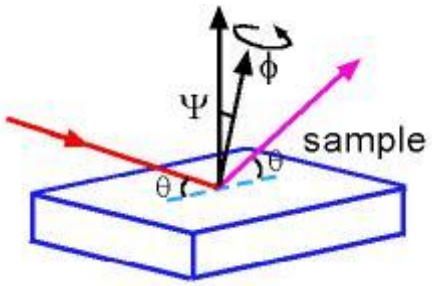

Figure 2.2: Pole figure measurement

Courtesy: http://www.mrl.ucsb.edu/mrl/centralfacilities/xray/xray-basics/index.html

2.3 Reflection High Energy Electron Diffraction

Pole figures give evidence of the epitaxy of the entire layers. For epitaxially grown YBCO it is a necessity to have a perfectly oriented surface to grow on. Reflection High Energy Electron Diffraction (RHEED) is an electron diffraction technique used to characterize the topmost layer (2-5 nm) of a crystalline material [11]. A coherent beam of electrons, generated by an electron gun, strikes the surface of the sample under a grazing angle (< 1.5°) and is diffracted by the

atoms at the sample's surface. Due to the very small angle and a wavelength of 7.08 nm for an accelerating potential of 30 keV, their mean free path perpendicular to the surface is at the most 5 to 10 nm. This has implications on the diffraction pattern. At the surface, the in-plane lattice parameters satisfy the Bragg condition. However, there is no diffraction condition for the out-of-plane lattice parameter. The diffraction pattern, captured on a photo luminescent screen or with a CCD camera, as a result exhibits either discrete spots (for monocrystalline material) or spots merged into rings (for polycrystalline material), that extend perpendicular to the surface.

Two types of RHEED exist. Kinematic RHEED, which is based on a single elastic scattering event of the electrons, is most often encountered and provides the typical diffraction pattern common to RHEED. In dynamic RHEED, the electrons are scattered more than once in the material and end up losing part of their initial energy. Computational models are needed to retrieve quantitative information from the diffraction patterns. In this work, <100> and <110> diffraction patterns were recorded by Institute for Metallic Materials (IFW Dresden, Germany) using a RHEED system (Staib Instruments). The sample stage, onto which the sample is placed, is rotated 45° around the axis perpendicular to the surface to optimize the intensity distribution.

2.4 Viscosity measurements

The viscosity of the solution is important to predict its wetting behaviour and its relationship to the final thickness of the film, according to the Landau-Levich equation [12]. The viscosity measurements were carried-out at a constant temperature of 20 °C using a DV-E Viscometer, Brookfield (Department of Inorganic and Physical Chemistry, UGent). The basic principle involved in the operation of the DV-E is to rotate a spindle which is immersed in the test fluid through a calibrated spring. The spring deflection quantifies the viscous drag of the fluid against the spindle. Spring deflection is measured with a rotary transducer which provides a torque signal. The measurement range of a DV-E (in centipoises or milliPascal seconds) is determined by the rotational speed of the spindle, the size and shape of the spindle, the container in which the spindle is rotating, and the full scale torque of the calibrated spring [13].

2.5 Spectroscopic measurements

In using IR spectroscopy as an analytical tool, three major categories based on the three IR spectral regions are considered [14]. The most important uses of near-IR region, which extends from the upper wavelength end of the visible region at about 13,000 to 4000 cm^{-1} are for the quantitative determination of species, such as water, proteins, low-molecular-weight hydrocarbons, and fats, in products of the agricultural, food, petroleum, and chemical industry. The far-IR region is particularly useful for inorganic studies because absorption due to stretching and bending vibrations of bonds between metal atoms and both inorganic and organic ligands generally occurs at frequencies lower than 650 cm^{-1}. The mid-IR, which extends from about 4000 to 670 cm^{-1} is the most widely used region. Here, absorption, reflection, and emission spectra are employed for both qualitative and quantitative analysis. The infrared spectra were recorded with a Bruker Equinox 55 instrument (Department of Inorganic and Physical Chemistry, UGent) in the spectral range between 4000 and 400 cm^{-1}, using the KBr pellet technique.

Raman spectroscopy being a non-destructive tool to study vibrational, rotational and characteristic phonon modes in solids. When monochromatic light (VIS, near IR or UV) interacts with the phonons (lattice vibrations) in a solid material, these modes are excited from the ground to a virtual state. Relaxation can then either happen in an elastic manner (resulting in Rayleigh scattering), or inelastically (resulting in Stokes or anti-Stokes scattering) [15]. The latter, referred to as the Raman effect, requires a change in polarizability. As the Raman effect itself is not very efficient, monochromatic light is provided by a laser which is a coherent, intense light source with a fixed wavelength. In this research, the Raman equipment utilized is a Thermo Scientific Nicolet NXR FT-Raman spectrometer (Department of Inorganic and Physical Chemistry, UGent) with a CaF_2 beam splitter. It doesn't matter if only one or two beam(s) pass through the sample, but one beam is made to traverse a longer distance. When both beams are recombined, an interference pattern is created. Changing the optical path difference gives rise to an interferogram. This Fourier transform method is superior to a dispersive method in that the wavenumbers can be scanned simultaneously. The Raman spectrum is a plot of the intensity versus shift (in cm^{-1}). For our research, the most interesting region is the area below 600 cm^{-1} where the M-O bonds manifest themselves.

In attenuated total reflection/ Fourier transform infrared spectroscopy (ATR/FTIR), used for analysis of the surface of materials, a beam of radiation passes from a denser to a less dense medium and reflection occurs [16]. The fraction of the incident beam reflected increases as the angle of incidence becomes larger; beyond a certain critical angle, reflection is complete. The depth of penetration, which varies from a fraction of a wavelength up to several wavelengths, depends on the wavelength, the index of refraction of the two materials, and the angle of the beam with respect to the interface. At wavelengths where the less dense medium absorbs the evanescent radiation, attenuation of the beam occurs, which is known as attenuated total reflectance, or ATR. ATR-IR (Perkin Elmer 160 FT-IR, Department of Organic Chemistry, UGent) was used for analysis of the surface of the films.

2.6 Scanning Electron Microscopy

Scanning Electron Microscopy (SEM) is an electron microscopy measurement and is mostly based on the following electron interaction with the specimen: secondary electrons, backscattered electrons and X-rays [17]. It is used to inspect surface features, i.e. the topography, of materials and generate images with a magnification in the μm-nm scale. When an electron beam is directed at a sample under a certain angle, the primary electrons penetrate the material and are scattered in all directions. The energy losses, due to inelastic scattering events, are converted into secondary effects such as secondary electrons SE, backscattered electrons BSE, characteristic X-rays and light. The amount and type of the secondary effects are strongly dependent on the physical and chemical structure of the material. As both the electrons and electromagnetic radiation originate from a specific interaction between the incident electrons and the sample, they can be used for chemical characterization.

Secondary electrons are used for imaging in terms of topography. Only electrons with an energy below 50 eV and an escape depth of 5 to 50 nm, are considered to be secondary electrons. These electrons either originally belonged to the sample atoms or are primary electrons that hit the sample and escape again from the surface. Secondary electron images provide contrast and are characterized by a good spatial resolution and a large depth of field.

Backscattered electrons are used for imaging as well, but with the purpose of obtaining compositional information. These electrons escape without losing energy from depths of more

than 20 nm below the surface. Contrary to secondary electrons, the resolution of a backscattered electron image is not as good because the yield in general is lower. However, this yield increases exponentially with the atom number Z. So, backscattered electron images are in fact representations of the homogeneity or heterogeneity of the sample surface. The intensity of the signals is given according to a greyscale.

Once areas of interest on a sample surface are identified, a spectrum of characteristic X-rays can be composed with Energy Dispersive X-ray detection (EDX). Elemental mapping is also an option. The SEM images and X-ray elemental analysis presented in this thesis are obtained with a FEG-SEM (FEI, (Department of Solid State Sciences, UGent).

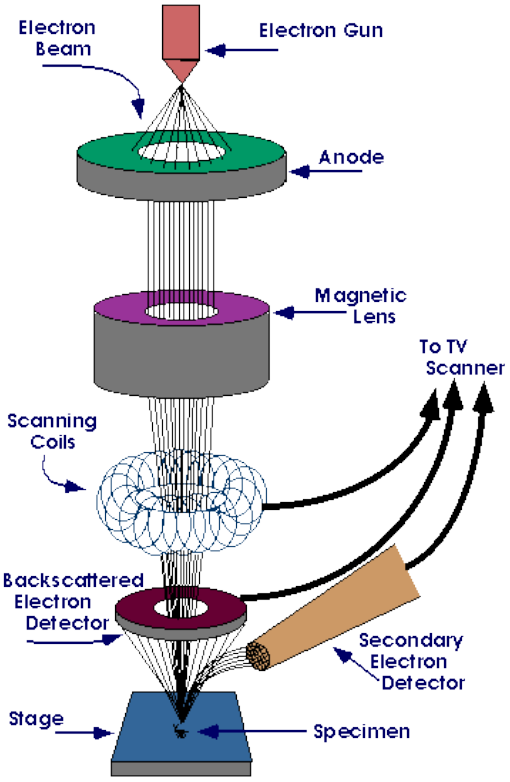

Figure 2.3: Schematic diagram of the main components of a SEM

A schematic diagram of the main components of the SEM equipment is shown in Fig.2.3. A field emission gun is used as electron source to obtain higher resolution in comparison to the thermo-ionic emission types. The electrons are accelerated to an energy which is usually between 1 keV and 30 keV. Two or three condenser lenses de-magnify the electron beam. It may have a

diameter of only 2-10 nm as it hits the specimen. The objective lens is used to further de-magnify the filament image producing a probe of a specific diameter on the surface of the specimen.

2.7 Ellipsometry

Ellipsometry estimates the thickness of the film once the substrate polarization ellipse is measured. A thin film as thin as ~ 1nm can be measured, as well as thicker multi-layers. A large flat area of a few mm^2 is needed for probing. The resulting plots of optical constants versus wavelength are computer-fitted to an optical model of the multilayer film. A good fit then reveals the remaining thicknesses and indices. Ellipsometry is based on measurements of the change in the polarization state of a light beam reflected by a surface [18, 19]. The quantities measured by an ellipsometer are the so called ellipsometric angles φ and Δ that are defined by the ratio ρ of the complex-valued reflection coefficients R_p and R_s for light parallel p and perpendicular s to the plane of incidence, respectively:

$$\rho = \frac{R^p}{R^s} = \tan\varphi e^{j\Delta} \qquad (2.1)$$

ρ, the amplitude ratio of is given by tan φ. Δ is the phase difference between the reflection coefficients in the p and s directions. The simplest case is reflection at the interface between two semi-infinite media, and a description with a two-phase model is used with $R_p = r_p$ and $R_s = r_s$, where r_p and r_s denote the Fresnel reflection coefficients [20]. R_p and R_s can be calculated by the Airy formulas, the scattering matric formalism [21], or a 4x4 matric formalism [22] if the sample has a single isotropic layer, an isotropic multilayer, or an anisotropic layer, respectively. Ellipsometry is a direct technique, and for extracting parameter values such as layer thicknesses or refractive indices from the experimental results, an appropriate optical model needs to be defined and fitting algorithms applied [23].

During this thesis Spectroscopic ellipsometry (JA Woollam Alpha-SE, Department of Solid State Sciences, UGent) was used to measure the thicknesses of cerium oxide films. In ellipsometry, a polarized beam of light is reflected off a sample at a given angle of incidence and the change in polarization state induced by the sample (the ratio of the in-plane (p) and out-of plane (s) Fresnel reflection coefficient) is measured. This measurement is presented in terms of the ellipsometric

parameters ψ and Δ where they signify the reflectivity ratio and the phase. To extract information such as thicknesses and optical constants, a model must be built to fit the optical data. The Easy-to-Use Acquisition/Analysis Software for Spectroscopic Ellipsometry Program (EASE) provides a graphical interface for building models and displaying experimental data and model fits. It was a powerful tool for acquiring spectroscopic ellipsometry (SE) data, building optical models, measuring layer thickness in this research. Fitting model parameters to the experimental data and generating data based on the current model are ways of extracting information about sample. When fitting data, the parameters of the model selected for fitting are adjusted by the software to provide the closet ('best fit') match to the experiment data. The criterion for the 'best fit' is minimization of the Mean Squared Error (MSE) which is calculated from the difference in the experimental standard deviations at each wavelength. If the model is correct, the data calculated from the model will fall on top of the experimental data. In addition to the MSE, an 'Absolute MSE' is also reported which is the unweighed error between the experimental and generated N, C and S data where N, C and S are defined as:

$$N = \cos(2\psi) \tag{2.2}$$

$$C = \sin(2\psi)\cos(\Delta) \tag{2.3}$$

$$S = \sin(2\psi)\sin(\Delta) \tag{2.4}$$

2.8 Transmission Electron Microscope

Transmission Electron Microscope (TEM) operates on the same basic principles as the light microscope but uses electrons instead of light. Their much lower wavelength makes it possible to get a resolution a thousand times better than with a light microscope. The beam of electrons is transmitted through an ultra thin specimen, where it interacts with the specimen as it passes through. An image is formed from the interaction of the electrons transmitted through the specimen; the image is magnified and focused onto an imaging device, such as a fluorescent screen, on a layer of photographic film, or to be detected by a sensor such as a Charge Coupled Device (CCD) camera [24]. The size, shape and arrangement of the particles which make up the specimen as well as their relationship to each other on the scale of atomic diameters and the

degree of order, and compositional details upto a few nanometers in diameter can be studied. The description of a typical TEM set-up is shown in Fig. 2.5

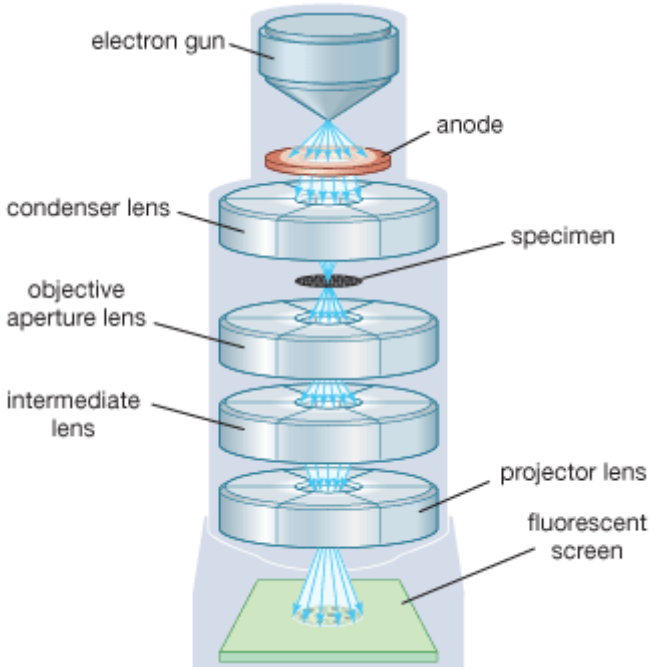

Figure 2.5: Description of TEM machine with the basic working principle

Courtesy: http://www.britannica.com/EBchecked/media/110686/Transmission-electron-microscope

The investigation of the detailed microstructure of the samples prepared in this work was performed in a C_s-corrected Transmission Electron Microscope (TEM, JEOL 2200 FS, Department of Materials Science and Department of Inorganic and Physical Chemistry, UGent and EMAT, University of Antwerp). For preparing the TEM samples, an in-situ lift-out procedure (FEI, Nova 600 Nanolab dual-beam FIB, Department of Materials Science and Department of Inorganic and Physical Chemistry, UGent) was used.

2.9 Critical temperature (T_c) and critical current density (J_c)

In superconducting materials, the characteristics of superconductivity appear when the temperature T is lowered below a critical temperature T_c. The value of this critical temperature varies from material to material.

Onnes recorded that there was a ‘‘threshold value’’ of the current density in mercury, above which the resistanceless state disappeared [26]. This critical value was temperature dependent,

increasing as the temperature was reduced below the critical temperature, according to the expression

$$Jc(T) = Jc(0)\ (Tc - T)/Tc \qquad (2.5)$$

This temperature dependent current density is termed as the critical current density (J_c). It is also dependent on the thickness. The J_c values of high temperature YBCO coated conductors are anywhere between 1.2 – 2.5 MA/cm^2, typically for RABiTS based coated conductors. The critical current density (Jc) of pulsed laser deposited (PLD) YBCO and YBCO using trifluoro acetate (TFA) method on the buffer layers was measured inductively with a Cryoscan (THEVA) instrument (IFW Dresden, Germany and Zenergy Power GmbH, Germany). The superconducting properties of the grown YBCO layers were determined by inductive methods. The critical current density J_c was measured at 77 K in self field using the THEVA Cryoscan assuming an YBCO thickness of 300 nm.

2.10 Atomic Force Microscope

The Atomic Force Microscope (AFM) consists of a cantilever with a sharp tip (probe) at its end that is used to scan the specimen surface. The cantilever is typically silicon or silicon nitride with a tip radius of curvature on the order of nanometers. When the tip is brought into proximity of a sample surface, forces between the tip and the sample lead to a deflection of the cantilever according to Hooke's law [27]. Typically, the deflection is measured using a laser spot reflected from the top surface of the cantilever into an array of photodiodes. The surface roughness of the thin films of the order of few nanometers can be measured based on the deflection of the cantilever while the tip scans across the surface. The surface analysis of the samples was carried-out using a Picoplus AFM equipment (Department of Inorganic and Physical Chemistry, UGent).

2.11 X-ray Photoelectron Spectroscopy

The principle of X-ray Photoelectron Spectroscopy **(**XPS) is based on the photoelectric effect outlined by Einstein in 1905 where

the concept of the photon was used to describe the ejection of electrons from a surface when photons impinge upon it [28]. This process can be expressed by the following equation 2.6:

$$BE = h\gamma - KE - f \quad (2.6)$$

Where BE is the binding energy of the electron in the atom (a function of the type of atom and its environment), $h\gamma$ is the photon energy of X-ray source, KE is the kinetic energy of the emitted electron that is measured in the XPS spectrometer and f is the spectrometer work function. For XPS, Al K_α (1486.6eV) or Mg K_α (1253.6eV) is often the photon energies of choice. Other X-ray lines can also be chosen such as Ti K_α (2040eV). The XPS technique is highly surface specific due to the short range of the photoelectrons that are excited from the solid. The energy of the photoelectrons leaving the sample is determined using an analyzer and this gives a spectrum with a series of photoelectron peaks. The binding energy of the peaks are characteristic of each element. The peak areas can be used (with appropriate sensitivity factors) to determine the composition of the materials surface. The shape of each peak and the binding energy can be slightly altered by the chemical state of the emitting atom. Hence XPS can provide chemical bonding information as well. XPS is not sensitive to hydrogen or helium, but can detect all other elements [29]. The analysis of composition has been widely applied in the thin film research fields. The detailed information of each element in the thin film can be obtained from the narrow scan spectrum of XPS. For all the discussion based on analysis of the samples, an X-ray Photoelectron Spectroscopy instrument from S-Probe monochromatized XPS spectrometer, Surface Science Instruments (VG) was used (Fig. 2.6) (Department of Solid State Sciences and Department of Inorganic and Physical Chemistry, UGent). The instrument uses an Al-K_α source (monochromatized Al-radiation: 1486.6 eV), at a base pressure of $2x10^{-9}$ mbar and an acceptance area of 250 x 1000 μm^2, with an hemispherical analyzer at a pass energy of 157.7 eV. The normally measured surface was 250 μm by 1000 μm. The voltage of the Ar^+-ion gun was maintained at 4 keV to sputter an area of 3x3 mm^2. Experimental data were processed using the software package CasaXPS (Casa Software Ltd., UK) using Shirley background and Scoffield sensitivity factors.

Figure 2.6: XPS machine used for the analysis with their major component indicated

A spectrum representing the number of electrons recorded at a sequence of energies includes both a contribution from a background signal and also resonance peaks characteristic of the bound states of the electrons in the surface atoms. The resonance peaks above the background are the significant features in an XPS spectrum [30]. XPS spectra are, for the most part, quantified in terms of peak intensities and peak positions. The peak intensities measure how much of a material is at the surface, while the peak positions indicate the elemental and chemical composition. Other values, such as the full width at half maximum (FWHM) are useful indicators of chemical state changes and physical influences. That is, broadening of a peak may indicate: a change in the number of chemical bonds contributing to a peak shape, a change in the sample condition (x-ray damage) and/or differential charging of the surface (localized differences in the charge state of the surface). The underlying assumption when quantifying XPS

spectra is that the number of electrons recorded is proportional to the number of atoms in a given state. The basic tool for measuring the number of electrons recorded for an atomic state is the quantification region. Figure 2.7 illustrates a survey spectrum where the surface is characterized using a quantification table based upon values computed from various regions and the expected elements. The primary objectives of the quantification region are to define the range of energies over which the signal can be attributed to the transition of interest and to specify the type of approximation appropriate for the removal of background signal not belonging to the spectrum.

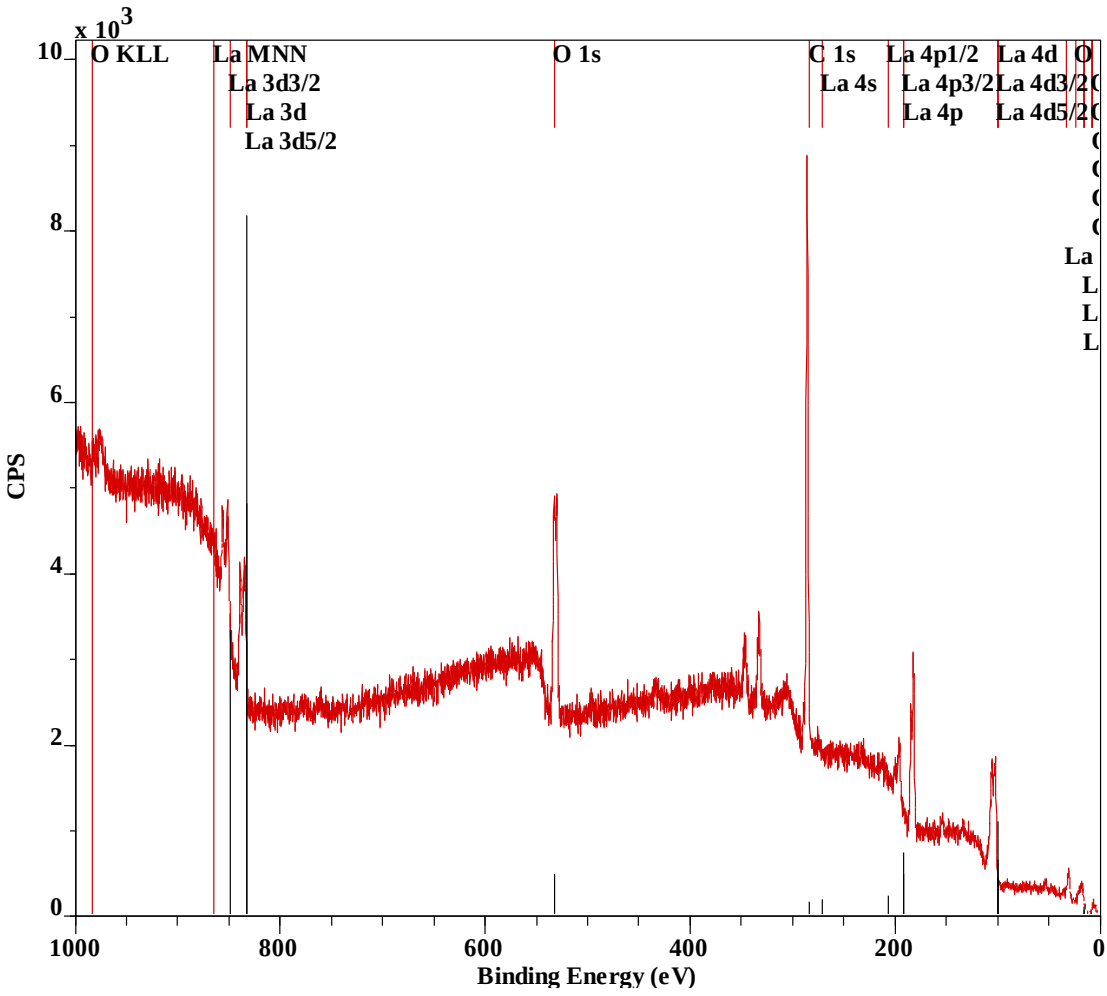

Figure 2.7: Survey spectrum of the thin film sample

A direct comparison of peak areas is not a recommended means of comparing samples for the following reasons. An XPS spectrum is a combination of the number of electrons leaving the sample surface and the ability of the instrumentation to record these electrons; not all the electrons emitted from the sample are recorded by the instrument. Further, the efficiency with which emitted electrons are in turn depends on the operating mode of the instrument. As a result, the best way to compare XPS intensities is via percentage atomic concentrations [31]. The main feature of these percentage atomic concentrations is the representation of the intensities as a percentage, that is, the ratio of the intensity to the total intensity of electrons in the measurement.

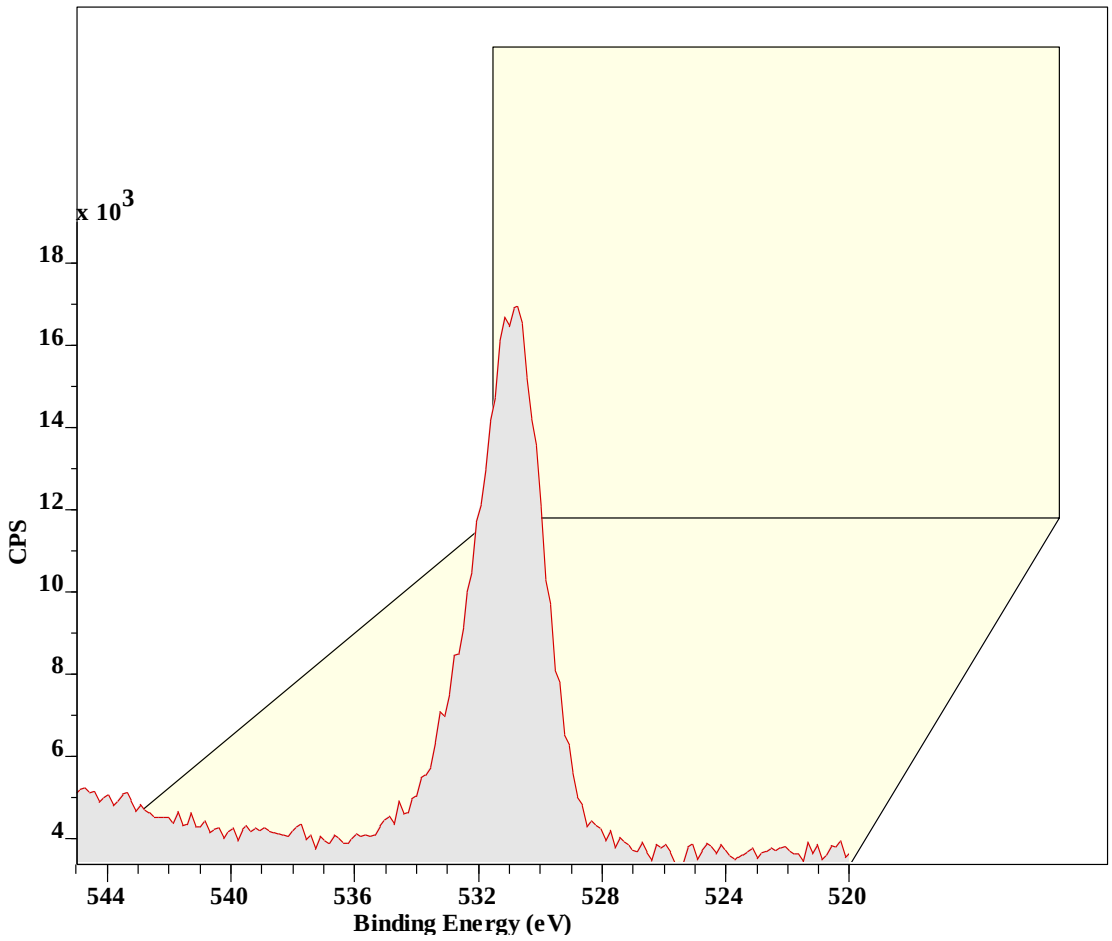

Figure 2.8: Area under consideration for oxygen O1s peak

In this research work, for a coated thin films on a Ni-5%W substrate, the various regions for non-overlapping energies for various elements are considered and multiplied by their relative sensitive factor (RSF) or Scoffield factor with Shirley back-ground correction using CASAXPS program. For analyzing various depths of the samples, 4 KeV Ar^+-ion bombardment is carried-

out to remove the layers of various thickness based on a calibrated Ta_2O_5 sputter rate of 1.5 – 2 Å/s. Sample is analyzed after every cycle of Ar+-ion bombardment and the atomic concentration of various elements, in terms of percentage, is calculated. The appearance of substrate peaks indicate the total removal of the buffer layer and the end of it. The depth profile measurement can be indirectly correlated to the thickness of the layer. A plot of various concentration of the elements versus the sputtering time is plotted and the thickness of the layer determined (Fig. 2.9).

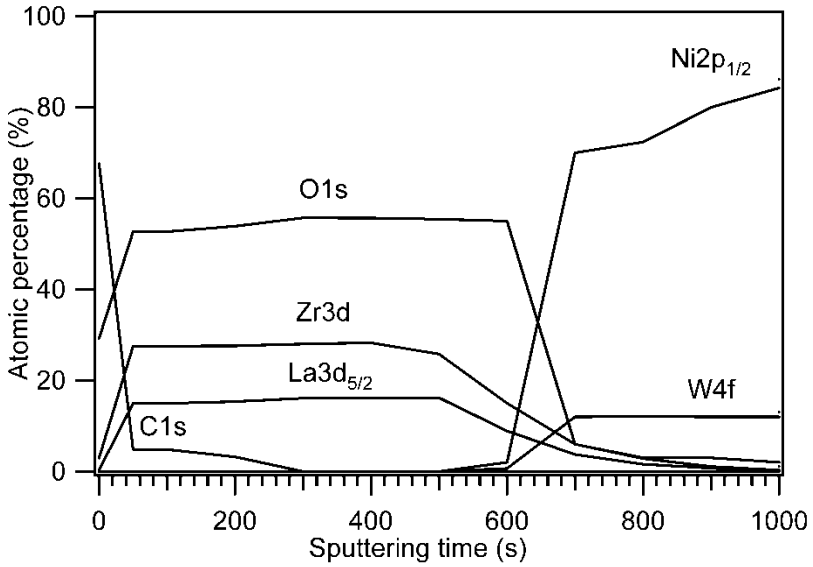

Figure 2.9: Depth-profile analysis-plot for a LZO thin film coating on Ni-5%W substrate

The regions under consideration for various elements in the coated layers are:

1. Oxygen 1s - 531.6 eV
2. Carbon 1s - 284 eV
3. Nickel 2p1 – 872 eV
4. Tungsten 4f – 34 - 37 eV
5. Lanthanum $3d_{5/2}$ – 832 eV
6. Zirconium 3d – 180 – 183 eV
7. Cerium 3d – 884 - 902 eV

References

[1] M.E. Brown, Introduction to thermal analysis: techniques and application. Chapman and Hall (1988).

[2] P. Gabbot, Principles and applications of thermal analysis Oxford: Blackwell (2008).

[3] A.W. Hull, (1919), Journal of Am. Chem. Soc. 41(1919) 1168-1175.

[4] B.D. Cullity, S.R. Stock, Elements of X-ray diffraction. Upper Saddle River (N.J.): Prentice-Hall (2001).

[5] V.K. Pecharsky, P.Y. Zavalij, Fundamentals of powder diffraction and structural characterization of materials, New York: Springer (2005).

[6] P. Scardi, L. Lutterotti, L. Correra and S. Nicoletti, J. Mat. Res. 8(1993) 2780-2784.

[7] T.G. Woodcock, J.S. Abell and M.G. Hall, M. G. Journal of Microscopy Oxford 205 (2001) 231-237.

[8] Q.L. Xu, L.J. Bi, D.K. Peng, G.Y. Meng, G. Zhou, Z.Q. Mao, C. G. Fan and Y.H. Zhang, Supercond. Sci. & Techn 3(1990) 564-567.

[9] Y. Akin, E. Celik, W. Sigmund and Y.S. Hascicek, IEEE Transactions on Applied Superconductivity 13(2003) 2563-2566.

[10] A. Scott and J.E. Gray-Munro Thin Solid Films 30 (2009) 40-45.

[11] A. Ichimiya and P.I. Cohen, Cambridge University Press, 2004.

[12] C.J. Brinker, A.J Hurd, P.R. Schunk, G.C. Frye and C.S Ashley, Journal of Non-crystalline solids, 147 (1992) 424-436.

[13] G. Penneman, "Ceramic layers of buffer layers for high Tc superconductors starting from aqueous sol-gel precursors" PhD thesis, Ghent University, 2007.

[14] D.A. Skoog, D.M. West and F.J. Holler, Fundamentals of analytical chemistry, Fort Worth (Tex.): Saunders college (1992).

[15] G. Socrates, Infrared and Raman characteristic group frequencies: Tables and charts, Chichester : Wiley & Sons (2001).

[16] F.A. Miller, D.W. Mayo and R.W. Hannah, Course notes on the interpretation of infrared and Raman spectra, Hoboken (N.J.) : Wiley-Interscience (2004).

[17] K. De Buysser, "Negative thermal expansion in substituted ZrW_2O_8 and its ceramic composites", PhD thesis, Ghent University (2007).

[18] D.L. Smith, Thin-film deposition: Principles and Practice, Mc Graw-Hill, Inc. (1995).

[19] R.M.A. Azzam and N.M. Bashara, Ellipsometry and polarized light, Amsterdam, North Holland (1988).

[20] H.G. Tompkins and W.A.M. Gahan, Spectroscopic ellipsometry and reflectometry, a user's guide, John Wiley & Sons, Inc.(1999).

[21] H. Arwin, M. Poksinski and K. Johansen, Applied Optics 43(2004)3028-3036.

[22] M. Schubert , Physical Review B 53(1996) 4265-4274.

[23] P. Atkins and L. Jones "Chemical Principles: The quest for insight " New York, W.H Freeman and Company.

[24] D.B. Williams and C.B. Carter. Transmission electron microscopy: a textbook for materials science,Springer Science (1996).

[25] R. Azzam and N.M. Bashara, Ellipsometry and polarized light Amsterdam, North Holland (2004).

[26] M. Cyrot, D. Pavuna. Introduction to superconductivity and high T_c-materials. World scientific (1992).

[27] G. Binning, H. Rohrer, Ch. Gerber and E. Weibel. Surface Studies by Scanning Tunneling Microscopy. Physical Review Letters (1982), 49-57.

[28] B.D. Ratner and D.G. Castner, Surface analysis: The principal techniques JC Vickerman Chichester [England]; New York: John Wiley (1997).

[29] E. Sokolowski, C. Nordling and K. Siegbahn, Physical Review 110 (1958) 776-784.

[30] S. Hagstrom, C. Nordling and K. Siegbahn Physics Letters 9 (1964) 235-236.

[31] D. Briggs and J.T. Grant, In Surface Analysis by Auger and X-Ray Photoelectron Spectroscopy (2003).

Chapter-3

Cleaning methods for Ni-5%W substrates and their effects

This chapter describes cleaning methods involved in the preparation of Ni-5%W substrates for the deposition of buffer layers using water based solvents. The substrate has been studied for their surface properties using XPS and RHEED. The contaminants in the substrates have been quantified and the appropriate cleaning method was chosen in terms of contaminants level and showing good surface crystallinity.

3.1 Need for Cleaning

Superconductors employing RABiTS (Rolling-Assisted-Biaxially-Textured-Substrates) offer a viable way to develop superconductor wires for commercial use (Chapter 1). Coated conductors are based on the deposition of oriented buffer layers and YBCO films on nickel alloy substrates. Researchers have noticed that the surface properties of the nickel surface play a crucial role in making it conducive to epitaxial film deposition [1]. The crucial factor to obtain a YBCO thin film is the ability to deposit smooth, dense, crack-free and highly aligned oxide buffer layers on textured metal substrates to protect the superconductors from metal contamination and, to provide an appropriate biaxially oriented, lattice matched substrate for the subsequent epitaxial growth of YBCO on top of it. Furthermore, such a barrier layer may also limit diffusion as well from the metal substrate to the superconducting coating as inversely, thereby allowing for a better control of purity and oxygen content. Before a buffer layer can be deposited, the substrates must be prepared for coating by an optimized cleaning procedure. Subsequently, optimized buffer layer architecture must be designed in order to have a biaxially textured, smooth and dense thin film that fulfils all the requirements. The first focus of this work was therefore to elucidate the action of different cleaning methods for the Ni- 5 at % W substrates. Flexible 80 µm thick and polished substrates are provided by Zenergy Power GmbH and produced by EVICO (Chapter 1). In this work, the results obtained from a combination of a chemical and thermal cleaning procedure based on a sequence of chemical treatments in trichloroethylene, acetone, methanol, deionized water and an etching mixture of hydrogen peroxide and formic acid and thermal treatment at 800˚C are reported. The chemical composition in terms of atom percentages of Ni and W and the contaminants including C and O are quantified using XPS as well as the influence of cleaning on top surface structure by RHEED studies is also presented. It was found that the cleaning treatments significantly improves the wettability of the substrates, a crucial property for the epitaxial growth of crack-free and homogeneous buffer layers by means of water-based solution-gel deposition techniques.

3.1.1 Chemical cleaning process

The substrates were dipped consecutively in trichloroethylene 99% (ACROS Organics), in acetone 99.5% (Fiers) and in methanol 99.85% (Fiers) where each dipping step lasted for 5 minutes for removing organic traces of oil, grease, and also dirt. This degreasing procedure was followed by a 5 minutes rinse in MiliQ water obtained from a MILLIPORE 00A/040 MiliQ water purification system. In this step, residual solvents and ionic salts were removed. Subsequently, the substrates were introduced in a hot mixture (50-55˚C) of hydrogen peroxide (H_2O_2) 35% in weight (Sigma ALDRICH): formic acid (HCOOH) 99% (Chem-Lab) of equal volume, for 5-15 minutes. This final step will involve 'etching' of the surface and will more specifically have an influence on grain boundaries. Substrates were afterwards rinsed twice for 10 minutes again with MiliQ water. The whole sequence of the treatment is termed as 'chemical cleaning' of substrates.

3.1.2 Thermal cleaning process

Substrates were exposed to high temperatures (800°C) for 1 hour in a quartz tubular furnace (CARBOLITE, Three zone furnace) and in a reducing atmosphere provided by a continuous flow of Ar-5%H_2 gas maintained at 0.2 L/min. The native NiO, which can act as passive protection for the Ni-5%W substrates will be reduced under the reducing gas flow during this step. Heating and cooling rate was set at 10°C/min. After this thermal treatment the substrates were stored in methanol to avoid contamination from air and particulates in the atmosphere.

3.2 XPS study

Initially, XPS study was undertaken to quantify the contaminants such as carbon and oxygen present in the tapes under uncleaned and differently cleaned conditions. The C 1s, O 1s, Ni 2p and W 4f peaks were considered for quantification. The binding energies corresponding to these elements are chosen as they possess the highest sensitivity. A depth profile study was carried out to enter at least approx. 6 nm depth of the samples from their surface. Ar^+-ion sputtering was carried-out for four consecutive sputter cycles each lasting 10 s. In total, 40 s of sputtering was carried out. According to the standard sputtering rate of Ta_2O_5, fixed at 1.5 Å/s, each sputter cycle can be roughly estimated to remove 1.5 nm thickness of the substrate and in

total, therefore approximately 6 nm thickness of the substrate is believed to have been sputtered and removed. There is native contamination of carbon and oxygen inside the XPS instrument which can cause an error in the estimation of species.

In the following discussion, many different combinations of chemical and thermal cleaning were carried-out on the substrates and discussed.

3.2.1 Uncleaned Ni-5%W substrate

Fig. 3.1 shows the depth profile XPS-study of the as-received, uncleaned substrate showing significant carbon contamination. The native carbon and oxygen contamination is removed after 10 s of sputtering, finally exposing the Ni and W peaks.

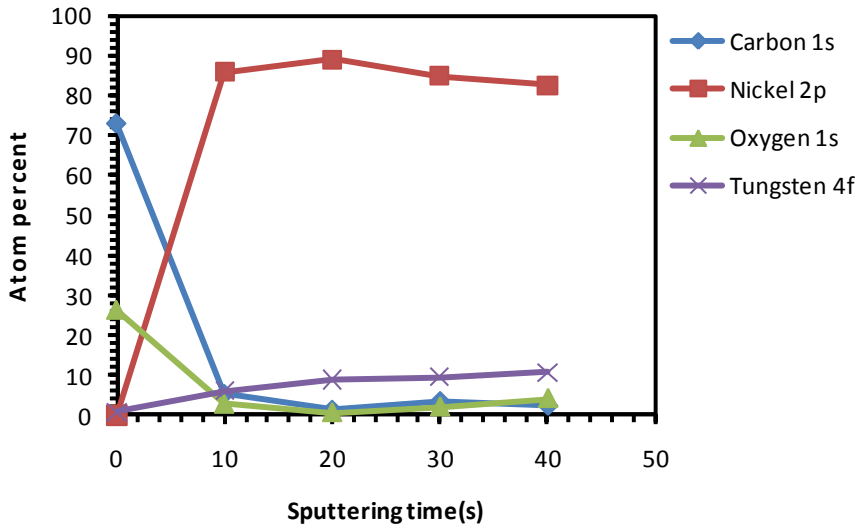

Figure 3.1: XPS depth profile studies of uncleaned Ni-5%W substrate

Fig. 3.2 explicitly depicts the Ni peaks under different sputtering cycles (from bottom to top). The Ni peaks in different sputtering cycle are shown because, the top-surface exposing the epitaxial Ni is crucial for the epitaxial growth of the following buffer layers and YBCO growth. The intensity of Ni peaks on the top surface and in different depths of sputtering, correlates to the exposed epitaxial Ni surface. The intense Ni peaks using XPS (AlK_{α}): Ni $2p_{3/2}$ and Ni $2p_{1/2}$ for metallic Ni is expected at a binding energy of 852.3 eV and 869.7 eV (along with their corresponding satellite peaks) whereas, it is expected at 853.3 eV and 871.7 eV for NiO. There is also an observation of a shoulder-peak for Ni $2P_{3/2}$ peak of NiO. The observation of peak shift in

Ni peaks helps in verifying whether it corresponds to metallic Ni or that of NiO. As seen in Fig. 3.2, less Ni is exposed on the top-surface compared to different depths of sputtering. The Ni peaks can be correlated to the corresponding to metallic Ni peak position as observed from the figure. The reason for the less intense peak of Ni can be attributed to the presence of surface carbon and oxygen as shown in Fig. 3.1. This shows the necessity of cleaning the surface prior to deposition of the buffer layers. Additionally, a droplet of water placed on this substrate did not wet the sample instead it remained stagnant (Fig. 3.3) with a contact angle of 75^{o}. This also means that the wettability of the native substrate needs to be improved to coat water-based solutions.

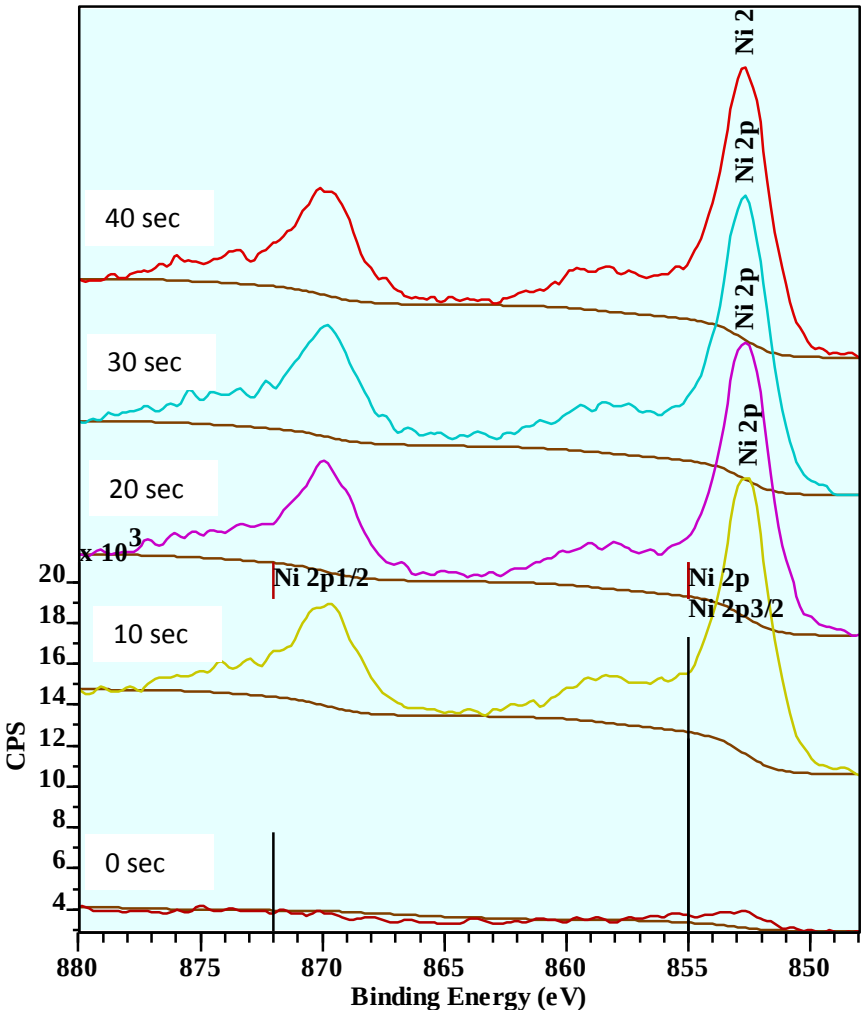

Figure 3.2: XPS depth profile studies of Ni peaks in uncleaned substrates

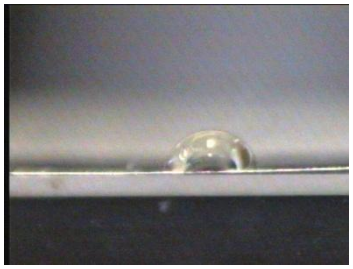

Figure 3.3: Nonwetting droplet of water on top of uncleaned Ni-5%W substrate

3.2.2 Chemical cleaning with etching for 15 minutes

The as-received substrates were chemical cleaned as described in section 3.1.1 and etched for 15 minutes. Fig. 3.4 depicts the various percentages of elements present in this sample after different sputter cycles thicknesses from the top-surface.

An increase in oxygen can be seen in the top-surface of the sample. This will most probably be due to the use of the HCOOH-H_2O_2 mixture which releases active oxygen species that can attach to the surface of the sample. The presence of oxygen is still seen after 20 s of sputtering which indicates that by etching the surface, the etchant has penetrated to several nm deep into the substrate. This can be interpreted that, the oxidation of the substrate up to ~4.5 nm thickness could have occurred. The visible peak of Ni in fig. 3.4 after 10 seconds of sputtering is indexed to be partially corresponding to that of NiO. The NiO grows along the thermodynamically stable (1 1 1) phase. The formation of NiO on the substrate surface can cause the growth of buffer layers along the (1 1 1) phase which is undesirable for the growth of c-axis YBCO. Fig. 3.5 shows the detail of the Ni-peak under different sputtering depths. However, compared to uncleaned substrate, there is only a small amount of Ni that is exposed on the top-surface after this cleaning procedure. Also, a decrease in amount of C at the surface is seen compared to the uncleaned substrate (Fig.3.4).

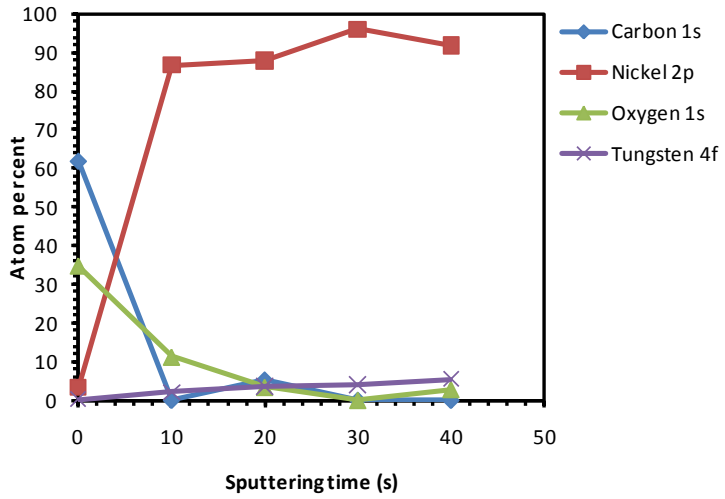

Figure 3.4: XPS depth profile studies of Ni-5%W substrate kept in etching solution for 15 minutes

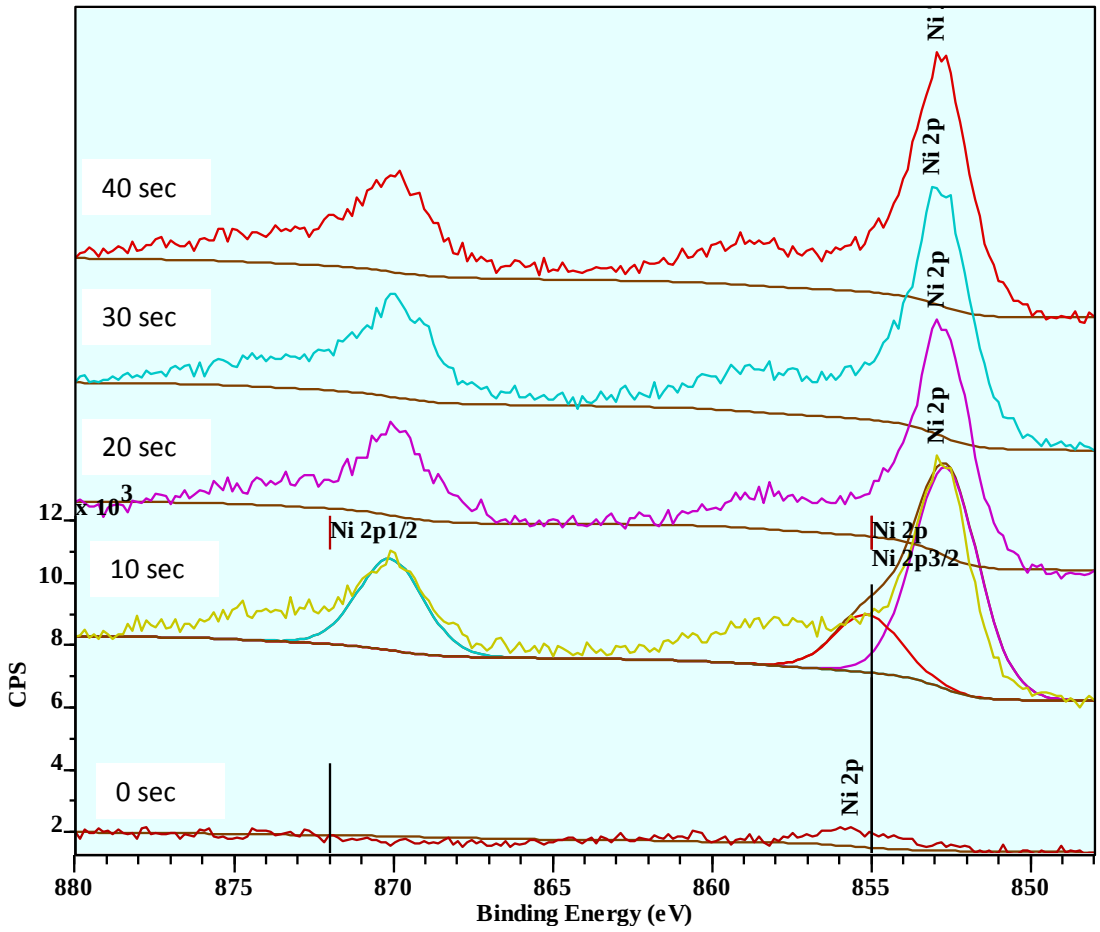

Figure 3.5: XPS depth profile studies of Ni peaks in substrate kept in etching solution for 15 minutes

However, etching for 15 minutes significantly improved the wettability of the substrate as tested by placing a drop of water similar to the etched substrate from 5 minutes. This improvement in the wettability can be a result of the roughness increase due to NiO formation.

Also, after etching, the concentration of carbon has decreased in comparison to uncleaned substrates (although the oxygen percentage is higher). This signifies that the carbon impurities are removed after etching. But, the oxygen percentage remains high which is also undesirable.

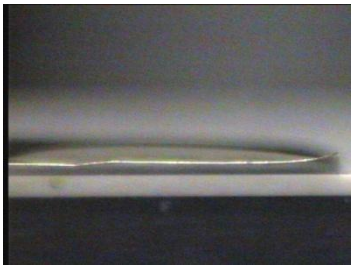

Figure 3.6: Perfectly wetted droplet of water on top of etched Ni-5%W substrate

3.2.3 Thermal cleaning

Thermal cleaning of the native substrates was carried-out under reducing gas flow to remove any native NiO that could be present in the substrate (sec. 3.1.2). As seen in Fig. 3.7, after thermal cleaning in the Ar-5%H_2 atmosphere at 800^{O}C for one hour, surface oxygen is reduced but, oxygen is not totally removed. Fig. 3.8 shows that the top-surface is exposing the Ni peak after thermal cleaning which was less visible in the uncleaned substrate. The wettability of the substrate was slightly improved as tested with a droplet of water as seen in Fig.3.9 (contact angle of 55^{o}).

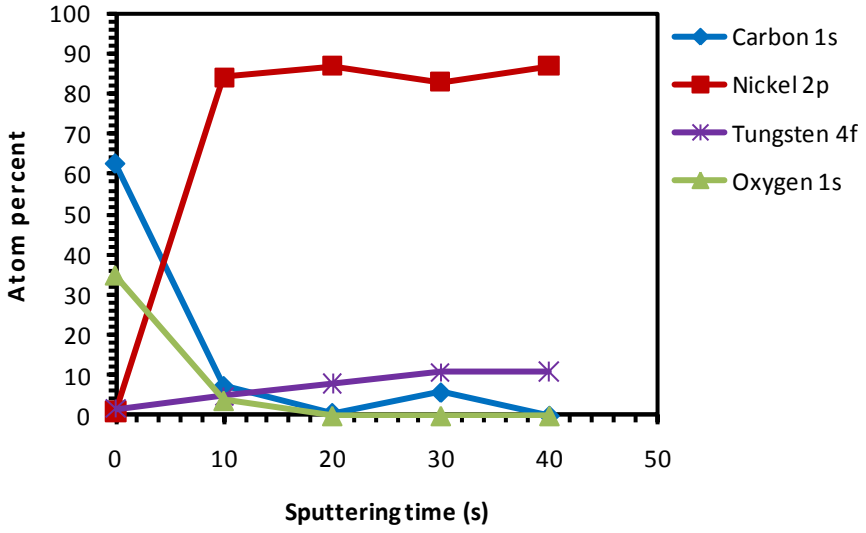

Figure 3.7: XPS depth profile studies of Ni-5%W substrate after thermal cleaning

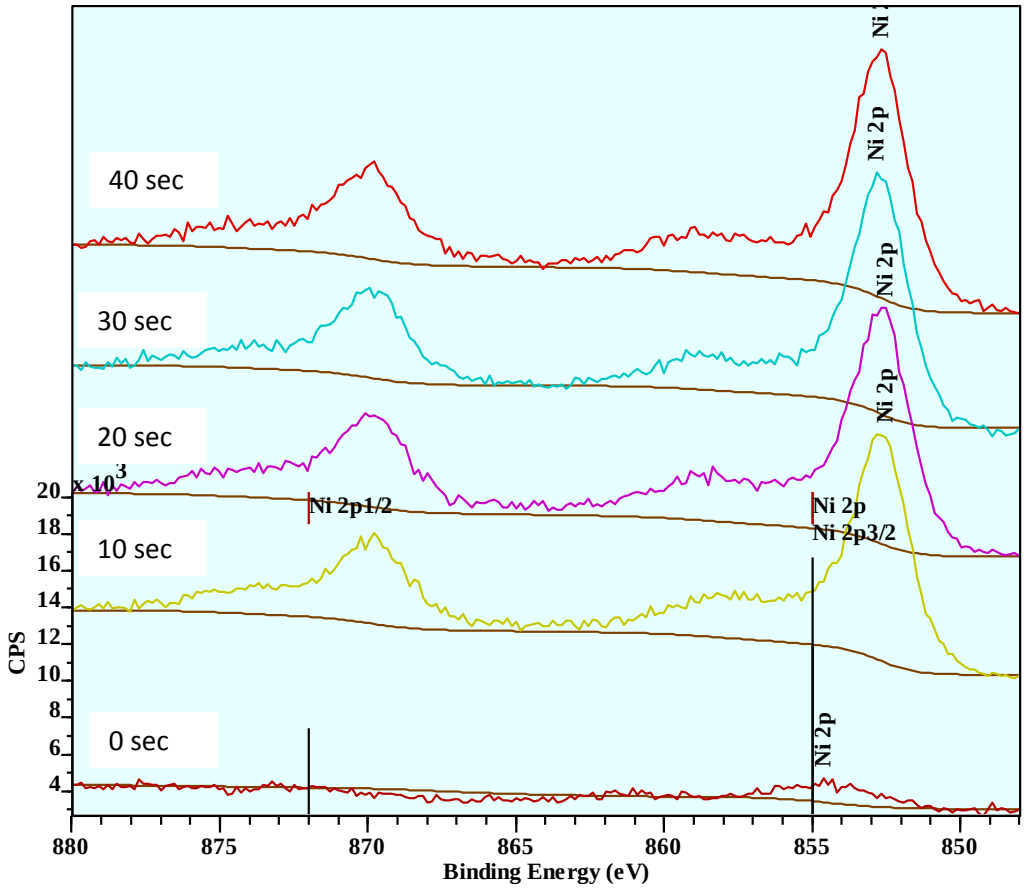

Figure 3.8: XPS depth profile studies of Ni peaks in substrate after thermal cleaning

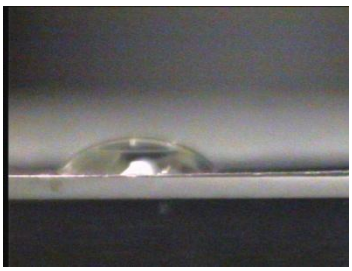

Figure 3.9: Water droplet on top of thermally cleaned Ni-5%W substrate

Both thermal and chemical cleaning result in a decrease of carbon in the spectra of the top surface of the sample. But, chemical etching result in a good wettability and high amount of oxygen as observed in the inner part of the sample. However, the thermal process shows only a minor improvement in the wettability and no increase in the oxygen content in the sample.

3.2.4 Thermal cleaning followed by chemical cleaning with etching for 15 minutes

To ensure good etching of the surface ensuring complete wettability of the surface as carried-out previously for 15 mins (sec. 3.2.2), the above said sequence of thermal followed by chemical cleaning was repeated with an etching time of 15 minutes and this showed improvement in the wettability with a contact angle of $< 5^{o}$, but the contamination with NiO (deconvoluted after 10 seconds of sputtering) did not improve as seen in figs. 3.10-11. The dependency of increasing percentage of oxide species with etch time can be confirmed from this.

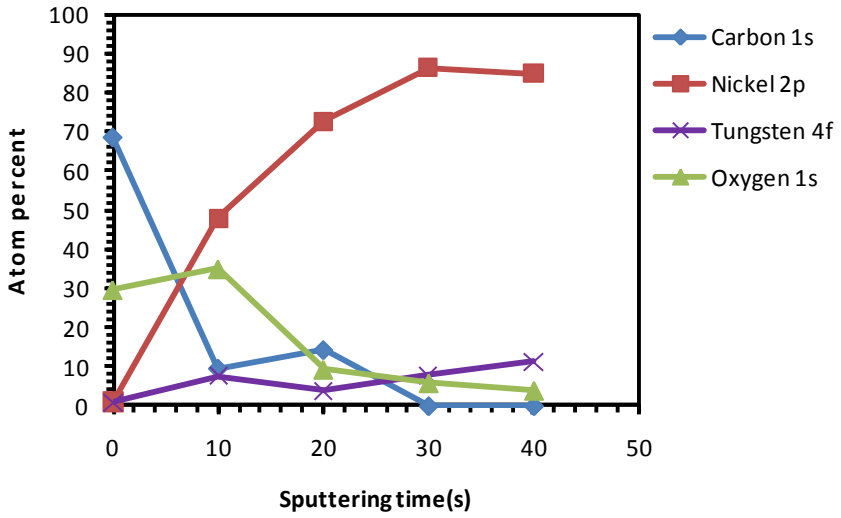

Figure 3.10: XPS depth profile studies of Ni-5%W substrate after thermal cleaning followed by chemical cleaning in etchant for 15 minutes

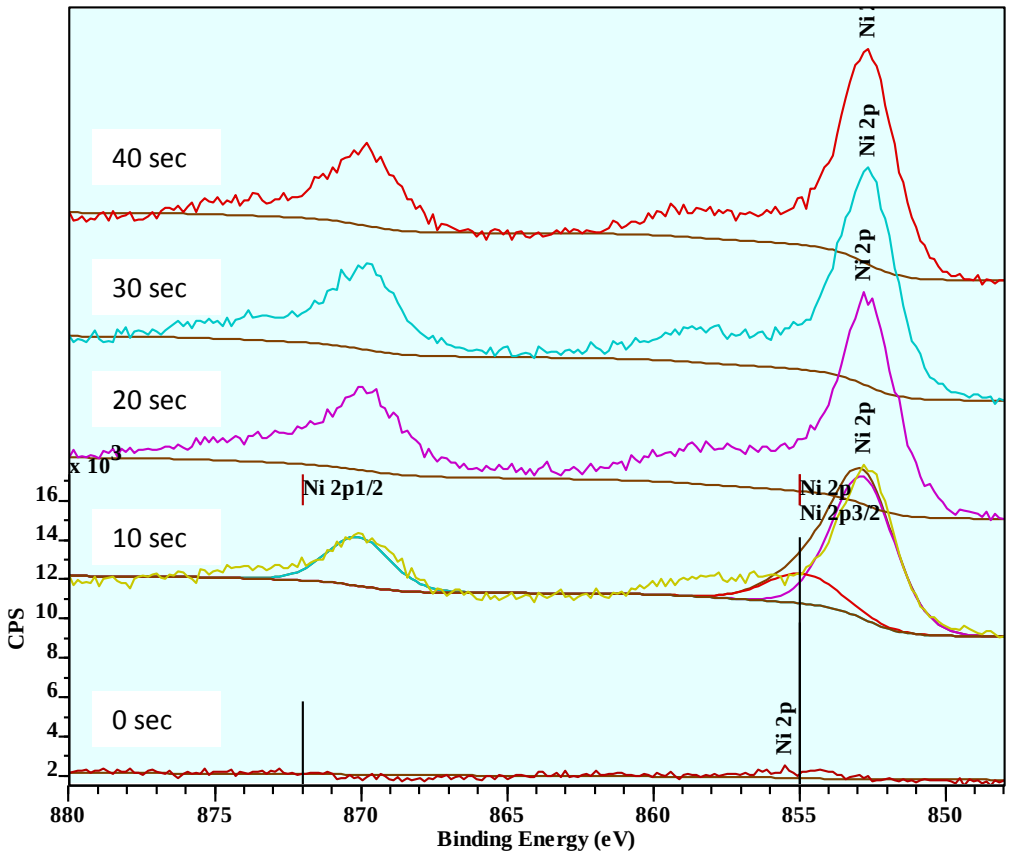

Figure 3.11: XPS depth profile studies of Ni peaks after thermal cleaning followed by chemical cleaning in etchant for 15 minutes.

3.2.5 Chemical cleaning with etching for 15 minutes followed by thermal cleaning

According to Sathyamurthy et al [2], a chemical cleaning followed by thermal cleaning improved the wettability and reduces carbon contaminations. According to Knoth et. al [3], cleaning the substrates in acetone under ultrasonic bath followed by thermal treatment under Ar-5%H_2 showed good wettability. According to Cloet et. al [4], a thermal treatment of the substrates under reducing gas flow followed by chemical cleaning and etching improved the wettability. Since, the thermal followed by chemical cleaning and etching showed significant oxidation as seen in previous sections, the reverse procedure of chemical cleaning with etching followed by thermal cleaning was applied. The above said condition was applied with etching time of 15 minutes. As seen in figs. 3.12 and 3.13, the Ni-peaks are better exposed on the top-surface and no visible oxidation of the substrate is seen.

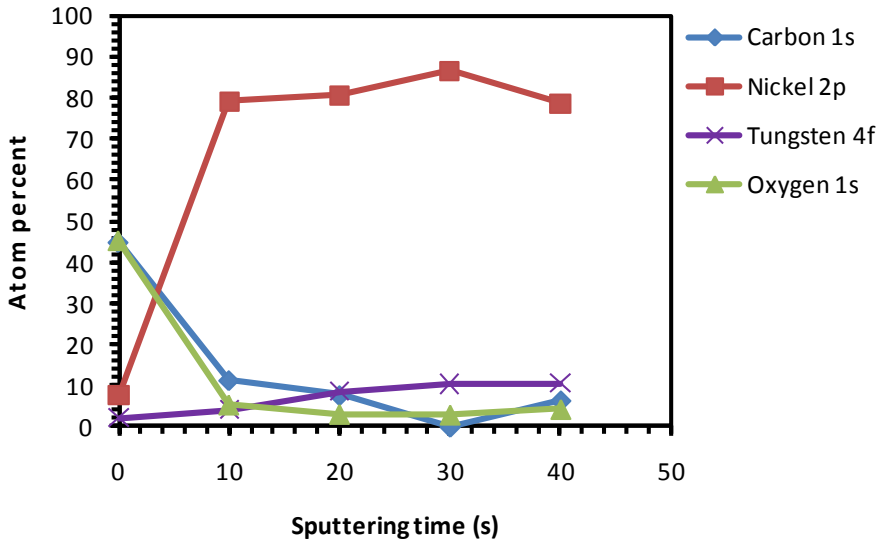

Figure 3.12: XPS depth profile studies of Ni-5%W substrate after chemical cleaning with etching for 15 minutes followed by thermal cleaning

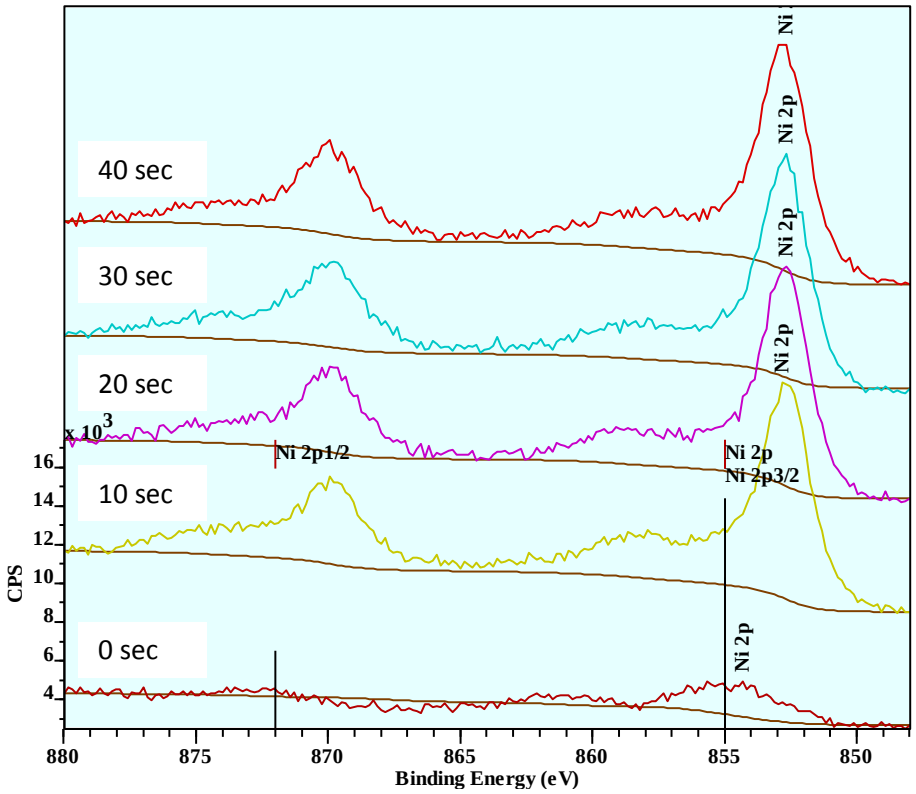

Figure 3.13: XPS depth profile studies of Ni peaks after chemical cleaning with etching for 15 minutes followed by thermal cleaning

Finally, the combination of chemical cleaning with etching for 15 minutes followed by thermal cleaning was chosen to be the best in terms on less surface contamination and exposure of epitaxial Ni surface and wettability (contact angle of 18^{o}), especially for water-based solutions (which has high surface tension) that needs wettable surface with less contaminations.

3.1 RHEED analysis

To qualitatively understand the presence of NiO, the substrates with thermal + chemical cleaning with 15 minutes etching (T+C) and another substrate with chemical cleaning and etching of 15 minutes + thermal cleaning (C+T) were chosen and analysed for native NiO spots. As seen in Fig. 3.20, the native NiO spots are clearly visible for the T+C samples compared to C+T sample. The faint spots seen in C+T sample are attributed to the crystalline Ni and a diffuse background layer that has developed due to the storage of the sample in methanol. The fitting of the RHEED diffraction spots was done by using the kinematic diffraction theory and the lattice constants corresponding to them were recalculated. Accordingly, the diffraction spots of T+C

sample matched with that of NiO (Lattice parameter of 4.17 Å) and diffraction spots of C+T sample matched with that of crystalline Ni (Lattice constant of 3.52 Å). From this it can be concluded that C+T cleaning is better and also storage of sample under methanol is undesirable as aging can cause the growth of the NiO layer. The presence of NiO is undesirable because, the (0 0 2) oriented epitaxial Ni is masked by the NiO which grows in its thermodynamically stable (1 1 1) phase. The presence of (1 1 1) NiO will hamper any growth of c-axis oriented buffer layers and in turn c-axis oriented YBCO growth on top of it. As mentioned in previous chapters, c-axis oriented growth of YBCO helps in the superconducting current transport along the a-b plane.

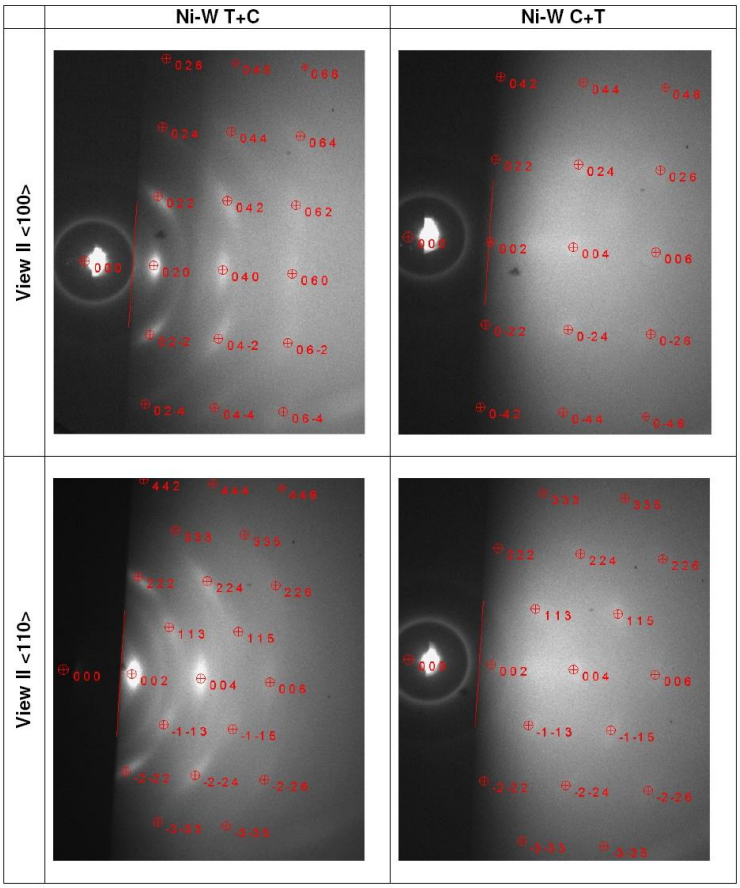

Figure 3.20: RHEED analysis of differently cleaned Ni-5%W substrates.

3.4 Conclusions

Different ways of cleaning the Ni-5%W substrate were tried and tested. The possible contaminations in terms of carbon and oxygen were quantified using XPS and the best cleaning method was chosen based on the minimal contamination and good surface crystallinity exposing epitaxial Ni. Accordingly, a chemical cleaning followed by thermal cleaning was opted.

References

[1] A. Goyal, D.P. Norton, D.K. Christen, E.D. Specht, M.P. Paranthaman, D.M. Kroeger, J.D. Budai, Q. He, F.A. List, R. Feenstra, H.R. Kerchner, D.F. Lee, E. Hatfield, P.M. Martin, J. Mathis, C. Park, Appl. Supercond. 4 (1996) 403-427.

[2] Srivatsan Sathyamurthy and Kamel Salama, Supercond. Sci. Technol. 14 (2001) 643–645.

[3] K. Knoth, R. Hühne, S. Oswald, L. Schultz, B. Holzapfel, Acta Mater. 55 (2007) 517-529.

[4] V. Cloet, J. Feys, R. Hühne, S. Hoste, I. Van Driessche, J. Solid State Chem. 182 (2009) 37-42.

Chapter-4

Study on multiple-buffer layered architecture of buffer layers for YBCO coated conductors

Multiple buffer layers of CeO_2 and $La_2Zr_2O_7$ (LZ,O) were deposited by the dip coating method. Two different buffer layer architectures were adopted. The deposited crack-free buffer layers were heat treated between 900° C and 1000° C on cubic-textured Ni-5at%W substrates. The heat treated buffer layers were analyzed for its physical properties using XRD, AFM and XPS characterization techniques. Here, the main focus was payed to the different buffer layer architecture and the distinction of its properties.

4.1 Introduction

2G-Superconductors prepared on Rolling-Assisted-Biaxially-Textured-Substrates (RABiTS) Ni-5at%W substrates are presently the major drive to develop superconductor wires for commercial use. Superconductor layers of YBCO deposited on these substrates need deposition of good quality buffer layer to avoid penetration of Ni into the YBCO layer. However, it should also be efficient in transferring the cubic texture of the Ni substrate to the superconducting layer [1]. A crack-free and thicker epitaxial buffer layer on top of these flexible substrate helps in transfer of the cubic texture of the substrate to the final YBCO layer. These form the prime requisites of the present day 2G HTSC, which employ different deposition techniques of buffer layers and the YBCO layer. CSD, eventually based on dip-coating is considered to be the most suitable and promising method with regard to up-scaling and cost-efficiency [2]. Coated conductors based on different buffer layers have gained world-wide acknowledgement. In this paper, the focus is on CeO_2 and LZO buffer layers. In recent years, LZO has been found to have better lattice match with Ni-5at%W substrate. Although LZO has better lattice matching with Ni-5at%W, CeO_2 has better compatibility and lattice match with YBCO. Hence, buffer layer architecture of CeO_2/LZO/Ni-5at%W [3, 4] have been widely accepted. The work here is carried out on an aqueous LZO buffer system to make it more environment friendly [3]. Also, a comparison on the performance of the CeO_2/LZO/Ni-5at%W and a simulated CeO_2/LZO/CeO_2/Ni-5at%W analogous to CeO_2/ YSZ/ CeO_2/Ni-5at%W [5] is shown.

4.2 Experimental Procedure

4.2.1 Preparation of Ni-5at%W

The Ni-5at%W tape (Evico GmbH, Germany) (80 μm thick)was cut into strips of approximately 3 cm. Further, it was dipped in acetone and methanol to remove any further organic impurities and then the pieces were etched in a 50-50 mixture of formic acid and hydrogen peroxide mixture. Finally, the cut pieces were thermally treated at 800^o C in Ar+5%H_2 atmosphere to remove any native NiO layer built up during storage and handling on the substrate surface (see chapter 3).

4.2.2 Deposition and characterization of buffer layer coatings

The cleaned Ni-5at% W was employed in the following two systems of buffer layer architecture:

System 1: A solution with a total metal concentration of 0.4M was used for dip-coating LZO prepared from water-based solution using TEA as a complexant [3]. Dip-coating was carried out at room temperature with varying dip-coat velocity and the substrates were withdrawn from the solution under an angle of 90.The substrates were immersed in the solution for 30 s before they were withdrawn [3]. Initially, the cleaned metal strips were coated with the LZO system at a dip coating speed of 30 mm/s. Subsequently, they were dried in an oven at 60ºC for one hour for gelation. Later they were annealed at 1050º C to obtain better crystallinity of the deposited LZO buffer layer. The second layer of CeO_2 was successively deposited on top of the previously annealed buffer layer of LZO [6]. A dip coating speed of 50 mm/s was employed. It was followed by drying in the oven at 60ºC followed by an annealing treatment at 1050ºC. This completes the architecture of the double buffer layered system of CeO_2/LZO/Ni-5at%W, which is shown in Fig.4.1

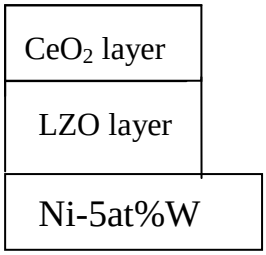

Figure 4.1: Diagrammatic representation of double-buffer layered architecture

System 2: The deposition and annealing methods are the same as explained in system 1, but with an extra CeO_2 directly on top of Ni-5at%W. The triple buffer layer architecture of CeO_2/LZO/CeO_2/Ni-5at%W is demonstrated in Fig.4.2.

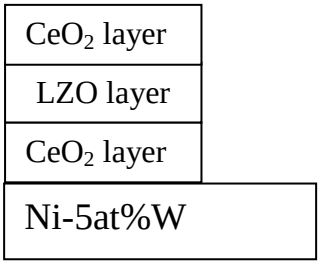

Figure 4.2: Diagrammatic representation of triple-buffer layered architecture

4.3 Results and Discussion

4.3.1 XRD analysis

The double buffered layer of CeO_2/LZO/Ni-5at%W and triple buffered layer of CeO_2/LZO/CeO_2/Ni-5at%W were deposited on a cleaned Ni-5at%W and annealed between 900º C and 1050º C as discussed in section 4.2.2. The obtained ceramic thin films are characterized using XRD to study the crystallinity and orientation of the (001) cubic peaks of the thin films. Fig. 4.3 shows a well-grown peak of (0 0 1) for the CeO_2/LZO/CeO_2/Ni-5at%W system, while for the CeO_2/LZO/Ni-5at%W system, an intensive and undesirable growth of (1 1 1) peak is observed.

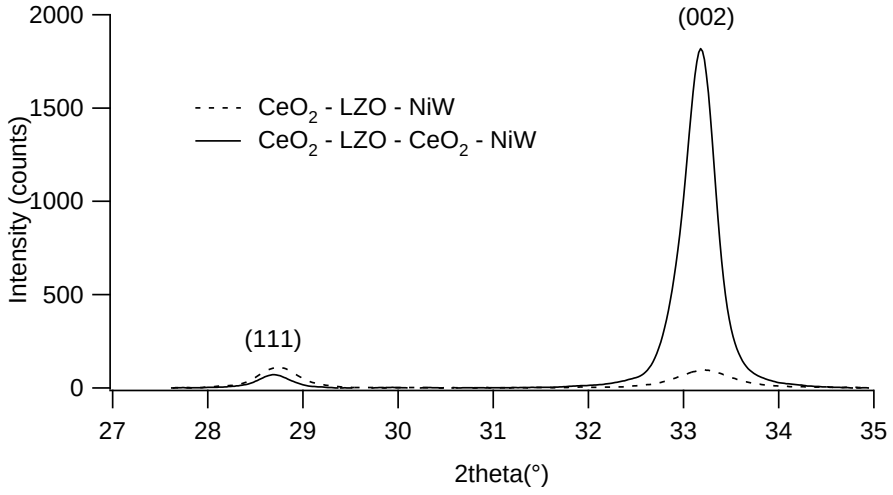

Figure 4.3: The XRD of CeO_2/LZO/Ni-5%W (System 1) and CeO_2/LZO/CeO_2/Ni-5at%W (System 2) substrate

The system of the triple buffer layer shows thus better crystal growth in the desired (0 0 1) orientation. The less intense growth of (0 0 1) phase in double buffer layered systems can be attributed to the absence of better coordination of thicker 70 nm LZO system with the underlying Ni-5at%W compared to that of a 20 nm CeO_2 layer (system 2). It can be inferred that thinner layers with better match at the interface of the substrate can promote better epitaxy.

4.3.2 AFM Measurements

The surface topology of the two systems has been compared and studied using the AFM measurements. The scanning area of the films was 25x25 μm^2. Fig. 4.4 shows the surface topology of the CeO_2/LZO/Ni-5at%W and fig.4.5, that of CeO_2/LZO/CeO_2/Ni-5at%W. Both show unfilled grain boundaries. This is typical for polycrystalline substrates as the grain boundaries that are deeper and it is further enhanced due to the etching occurring during chemical cleaning treatment.

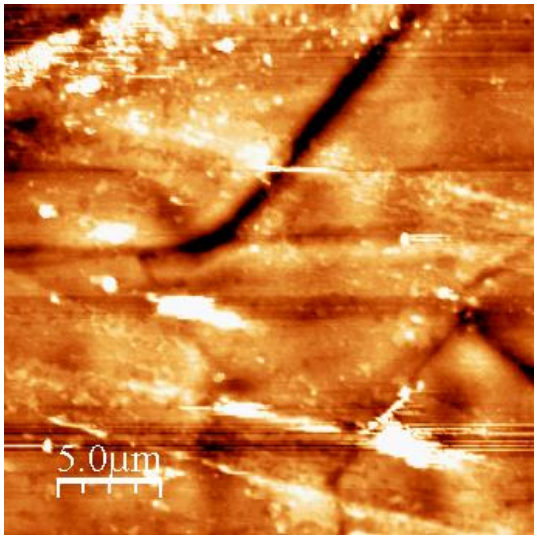

Figure 4.4: The unfilled grain boundaries of Ni-5at%W in CeO_2/LZO/Ni-5at%W (System 1)

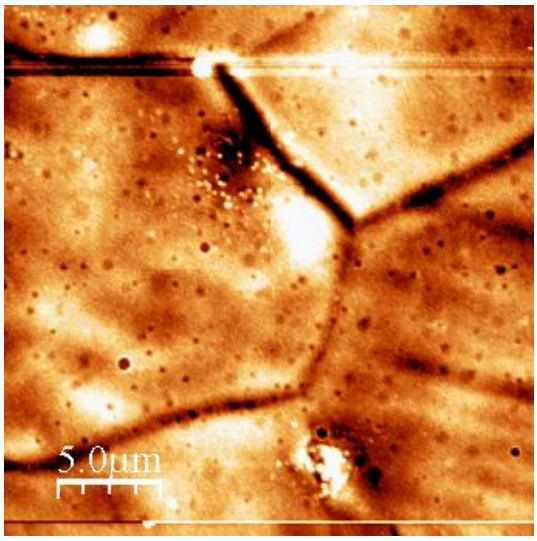

Figure 4.5: The unfilled grain boundaries of Ni-5at%W in CeO_2/LZO/CeO_2/Ni-5at%W (System 2) substrate

Comparable RMS surface roughness is seen for both systems, CeO_2/LZO/Ni-5at%W shows a value of 12.38 nm and that of CeO_2/LZO/CeO_2/Ni-5at%W system is 10.28 nm. This is attributed to the presence of CeO_2 as the top surface layer in both the systems. Clearly, CeO_2 shows a uniform, smooth and homogeneous growth [3]. Unfortunately, both systems show the Ni-5at%W grain boundary. This contributes to the fact that, the buffer layers have not filled the grain boundary of Ni-5at%W completely. After the superconductor layer deposition, the presence of the substrate grain boundary can be detrimental in the current carrying properties of the thin films.

4.3.3 XPS analysis

An XPS analysis on these multi-buffered layers was performed to study the distribution of various elements at different depths of the deposited thin films.

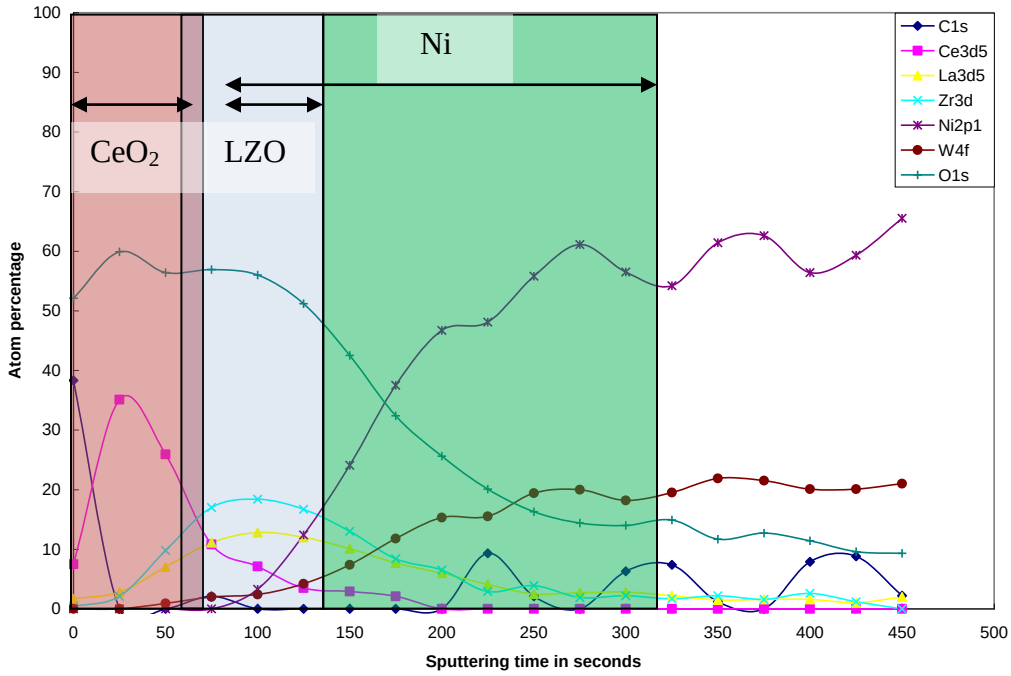

Figure 4.6: Depth profile measurement showing the presence of various elements at different depths of the thin film in CeO_2/LZO/Ni-5at%W (System 1)

Fig. 4.6 depicts the top layer of CeO_2 for system 1 extending over a length of 20 nm thickness (from ellipsometry). The inter-diffusion of LZO layer into the CeO_2 starts well before the range of CeO_2 layer of 20 nm thickness. It can also be probably attributed to the fact that, the layers were less dense and led to inter-diffusion of Ce and La ions during the annealing of the successive layers at high temperatures, as seen in the XPS. The presence of surface carbon and oxygen is well indicated in the Figs. 4.6. The penetration of Ni ions starts at an early stage which is seen from the top surface (Calibrated with sputtering rate of Ta_2O_5=1.5 Å/s). Theoretically, the Ni is not expected until the total thickness of the deposited buffer layer. In whole of the coated layer, nickel appears in the spectrum after 100 seconds of sputtering. Approximately 225 sputter seconds later, the atomic concentrations of La and Zr drop towards zero, while the Ni concentration reaches a plateau. To calculate the Ni penetration depth from these XPS data, we need to estimate the sputter rate for any one of this buffer layer. From ellipsometry, we determined the total layer thickness (sum of the two layers) to be 70 nm.

One can assume in this multiple buffer layer system taking LZO buffer layer of 50 nm thickness as standard, the effective LZO buffer layer starts at 25 s of sputtering and ends at 250-300 s of sputtering. It goes to half its value at 225 s. this means we average out a sputtering rate of approx. 2.2 Å/s. Ni appears in the spectrum after 100 s and thus after sputtering away the first 22 nm of the layer. Fig. 4.7 shows the distribution of elements at various depths after sputtering in the system 2.

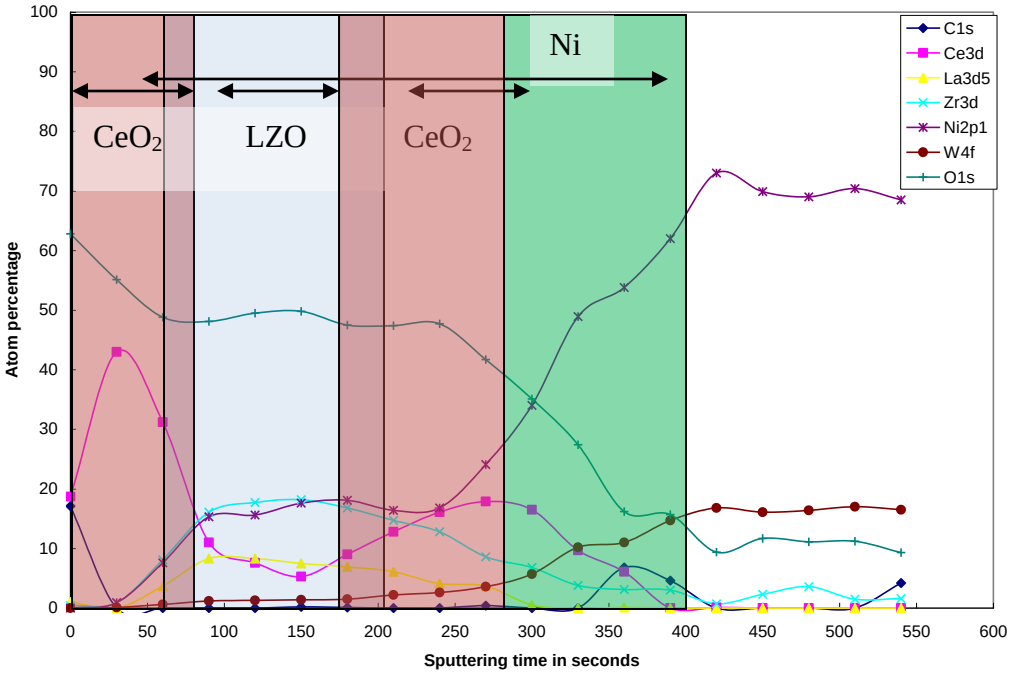

Figure 4.7: Depth profile measurement showing the presence of various elements at different depths of the thin film in CeO_2/LZO/CeO_2/Ni-5at%W (System 2)

Fig. 4.7 explicitly shows the presence of two distinct CeO_2 layers sandwiching the LZO layer. There is a clear overlap of CeO_2(20nm) / LZO(50 nm) / CeO_2(20 nm) regions indicating inter-diffusion of Ce and La ions through all the three layers. Based on the calculations used for the previous system in whole of the coated layer, nickel appears in the spectrum after 50 seconds of sputtering in a 90 nm (from ellipsometry) thick film. Approximately 350 sputter seconds later, the atomic concentrations of La and Zr drop towards zero, while the Ni concentration reaches a plateau at 400 s. Zr concentration drops to half of its averaged plateau value (i.e. at 250-275 s), indicating a sputtering rate of approx. 1.8-2 Å/s. Ni appears in the spectrum after 50 s and thus after sputtering away the first 9-10 nm of the layer. The Ni ions are seen as few as 9-10nm depth from the top

surface. This indicates Ni penetration through the buffer layers and evidence of inter-diffusion in multiple layers which is undesirable.

4.4 Conclusions

It is seen that the three buffer layered system shows better lattice matching with the substrate as seen in the XRD results. This is because, thin layer of 20 nm (CeO_2) forms good epitaxial growth with the underlying substrate compared to the thick layer of LZO with the substrate (system 1). However, both the systems are not able to control the penetration of Ni ions as seen from the XPS data. System 1 showed better Ni penetration properties compared to that of system 2. More interfaces in the CeO_2/LZO/CeO_2/Ni-5%W (system 2) probably contribute towards inter-diffusion in the interface rather than prevention of Ni diffusion. Secondly, the grain boundary of Ni-5at%W is not covered completely by the buffer layer deposition which is important to achieve homogeneous growth of the to-be deposited YBCO layer. In summary, we can conclude that, thinner layers (seed layer) on top of the susbtrate promote good epitaxial growth of the to-be deposited thicker layers as seen from the XRD measurements. This can be attributed to lower stress distribution in the island like growth of crystals in the thin layers on a epitaxial substrate that relieves the stress in adapting the epitaxy. Furthermore, it was seen through the XPS measurements that, multiple buffer layers show inter-diffusion as in CeO_2/LZO/CeO_2/Ni-5%W (system 2) compared to CeO_2/LZO/Ni-5%W (system 1). Since LZO proved to be a better barrier layer for Ni penetration, thick and single buffer layers of this system are required with optimal properties.

References

[1] Srivatsan Sathyamurthy and Kamel Salama, Supercond. Sci. Technol. 14 (2001) 643-645.

[2] Marius Steffens, Martina Falter, Michael Bäcker, Christina Oligschleger, J. Physics: Conference Series 97 (2008) 012165-012168.

[3] V. Cloet, J.Feys,, R.Hùhne, S.Hoste , I.Van Driessche, J. Solid State Chem. 182 (2009) 37–42.

[4] G. Kotzyba, B. Obst, R. Nast, W. Goldacker, B. Holzapfel, J. Physics: Conference Series 43 (2006) 345-348.

[5] A. Goyal, D.P. Norton, D.K. Christen, D. Specht, M. Paranthaman, M. Kroeger, M. Budai,Q. He, A. List, R. Feenstra, H.R. Kercher, D.F. Lee, E. Hatfield, P.M. Martin, J. Matthias, IEEE. Trans. Appl. Supercond.69 (1996) 403-410.

[6] K. Knoth, R. Hühne, S. Oswald, L. Molina, O. Eibl, L. Schultz, B. Holzapfel, Thin Solid Films 516 (2008) 2099-2108.

Chapter - 5

Thick layers of LZO

In this chapter, several solutions based on metal-chelate chemistry using water as the main solvent were prepared in an attempt to make thick layers in a single coating. As seen in chapter 4, multiple layers and thin layers of LZO show significant Ni penetration and are hence undesirable. Polymeric polyvinylpyrrolidone (PVP) was included in the solutions to increase the critical thickness of the deposited films. Here, we analyze the crystallinity, morphology in terms of the XRD, RHEED, SEM and TEM measurements.

5.1 Experimental - Materials and methods

Four different LZO precursor solutions were formulated. The solutions were prepared based on metal-chelate chemistry to keep the metal ions dispersed homogeneously in the solution [1, 2]. Zirconium acetate hydroxide, zirconium propoxide and lanthanum acetate were used as metal precursors. All of the solutions contained ethylene-diamine tetraacetic acid (EDTA) as the complexant with water as the main solvent and acetic acid as an additional solvent. Two of the systems were prepared with inclusion of polymeric polyvinyl pyrrolidone (PVP). The additives included ethylene diamine (EDA), ammonia, 2-amino 2-methyl 1-propanol (AMP) and ethylene glycol (EG), that helped in the dissolution of EDTA and increase in wettability of the solutions, respectively. The following table gives an overview of the systems:

Table 5.1: Overview of the systems

Category	***Metals***	***System***	***Additives***
1	*Zirconium acetate hydroxide, Lanthanum acetate*	*S1*	*EDA, EG, Ammonia*
2	*Zirconium propoxide, Lanthanum acetate*	*S2*	*EDA, EG, Ammonia*
		S3	*EDA, EG, Ammonia, PVP*
		S4	*AMP, Ammonia, PVP*

Different concentrations of metal solutions were tried and tested including that of 0.2 mol/L, 0.4 mol/L and 0.6 mol/L. In the following section, only solutions of 0.4 mol/L concentration are discussed as they showed optimal stability.

Category 1: Lanthanum acetate-Zirconium acetate hydroxide based systems

This category of systems uses inorganic metal salts (acetates) as the precursor materials and a chelant or complexant (EDTA) to prevent the metal ions from precipitating. This metal-chelate structure reduces the free concentration of metal ions in the solution by forming water-soluble metal complexes. With variation of pH and metal concentration gelation can occur upon the evaporation of the solvent [1]. These systems henceforth will be referred as, **inorganic metal-chelate systems.** Additional organic components like EDA, EG play their specific role in these systems which will be discussed in the following sections.

System S1: La acetate-Zr acetate-EDA-EG system: A 0.4M LZO solution was prepared by dissolving zirconium acetate hydroxide ((Zr $(CH_3COO)(OH)_3$), Aldrich) in water (molar ratio Zr^{4+}: water = 1:170) at room temperature. On heating, the mixture gelates. Acetic acid (molar ratio of Zr^{4+}: acetic acid = 1:20) was added to the metal solution at room temperature and the mixture was heated to 80°C. Acetic acid was added to aid in better dissolution of the metal ions as well to obtain clear solutions and gels [3]. Ethylene-diamine tetra acetic acid (EDTA, Sigma-Aldrich, > 99.4%) was used as a complexant to keep the metals stable in solution at high concentrations and increased pH values [4, 5]. The EDTA solution was prepared by dissolving EDTA in a water and ethylene diamine (EDA, Fluka, 100%) mixture (molar ratio of EDTA: Water: EDA = 1:130:4) at room temperature. This is because, EDTA does not dissolve in water in acidic medium. It dissolves only in neutral to basic medium > 6 or 8 [6]. EDA is a highly alkaline liquid which is also the parental compound of EDTA. Hence EDA was added to the EDTA-water mixture to increase the pH and hence augment the dissolution of EDTA in water. EDA addition to EDTA in the water mixture caused an increase in temperature indicating the occurrence of acid-base reactions between EDA and EDTA. Different molar ratios of EDTA and (La^{3+}+ Zr^{4+}) were tried and finally fixed at 0.5:1. The reasoning behind this lies in the fact that the solution as well as the gel obtained from this ratios are stable. Then, the metal solution (La^{3+}+ Zr^{4+})

was slowly added to the EDTA solution at room temperature and stirred for 10 minutes. The pH of the mixture was adjusted to 6 by adding ammonia. A fixed amount of ethylene glycol (EG, Sigma- Aldrich, > 99%) was added to the above solution at 60°C (molar ratio EDTA: EG = 1:4). Finally, the excess solvent was evaporated until the desired concentration of 0.4 mol/L was obtained. The pH of the final solution was found to be 6.2-6.3 and a viscosity of 4.7-5 mPa s was obtained.

Category 2: Lanthanum acetate-Zirconium propoxide based systems

In the following category of systems, a combination of metal salt (acetate) and a stabilized metal alkoxide are used as the precursor materials. EDTA again acts as a chelant or complexant to prevent precipitation of metal ions in the solution. This procedure partly deduces the concept from the thin film preparation of piezoelectric thin films of lead zirconium titanante (PZT) wherein the combination of a metal salt (lead acetate) and stabilized metal alkoxide (zirconium alkoxide) form the hybrid process mechanism [7-9]. Hybrid processes are those in which the A-site precursors are carboxylate based precursors and B site precursors are alkoxides. These processes are called 'hybrid' because they use both carboxylates and alkoxides. The A-site carboxylate precursor is usually dissolved in the corresponding carboxylic acid because of their limited solubility in alcohols. When mixed, the B-site alkoxide precursors react with carboxylic acid to form oligomers. For e.g

$$2nZr(OR)_4 + 2n\ R'COOH \rightarrow 2nRO[\text{-}Zr\text{-}O\text{-}](OOCR')_2R + 4ROH \qquad (5.1)$$

As seen from the equation above, these routes rely heavily on the molecular modification of the alkoxide compounds, through reactions with other carboxylic acids (acetic and propionic acids). Usually the carboxylate groups, co-ordinate in a bidentate way with the B-site cation, thereby acting as bridging ligands. This chelation of the B-site cation leads to precursors which are less sensitive towards hydrolysis. Acetic acid or 2-4 petanedione (acetyl acetone) is often used as a chelating agent for the B-site alkoxides. This hybrid process followed by metal chelate (EDTA) was used to keep the excessive metal ions in place. Also, EG was added to increase the viscosity of the solutions.

System S2: La acetate-Zr propoxide system: The lanthanum precursor was retained to be lanthanum acetate. The zirconium precursor is changed to Zirconium n-propoxide (70%

w/w in n-propanol, Sigma-Aldrich). A 0.4M LZO solution was prepared by dissolving stoichiometric lanthanum acetate (La $(CH_3COO)_3.1.5H_2O$, Alfa- Aesar, 99.9%) in a water-acetic acid mixture (molar ratio La^{3+}:acetic acid:water= 1:16:150) at 80°C until a clear solution was obtained. The water sensitivity of the zirconium alkoxide was reduced by stabilizing it with acetic acid (molar ratio Zr^{4+}:acetic acid = 1:4) at room temperature [10]. The stabilized zirconium propoxide was diluted by adding water in a 1:20 molar ratio of Zr^{4+}: water at 80°C. The solution was clear after stirring for 5 minutes at 80°C. The zirconium precursor solution was added continuously to the lanthanum precursor solution at 80°C. The EDTA solution and the required EG were mixed with the metal solution (La^{3+}+ Zr^{4+}) as described in system S1. This solution was stirred and the excess of solvent evaporated until the desired concentration of 0.4 mol/L is obtained. The final solution is found to have a pH of 6.2-6.3 and a viscosity of 5.2-5.5 mPa s .

System S3: La acetate- Zr propoxide-EG-PVP system: System S3 is identical to system S2, except for the addition of polyvinyl pyrrolidone (PVP, Alfa- Aesar, MW 8000) to the solution. After addition of EG, a stoichiometric amount of PVP was added (La^{3+}+ Zr^{4+}: PVP = 1:0.5) and the mixture is heated until the final concentration of the solution reached 0.4 mol/L. The pH and viscosity of the solution is found to be 6.3 and 5.7-5.9 mPa s respectively.

System S4: La acetate-Zr propoxide-AMP-PVP system: The metal solution (La^{3+}+ Zr^{4+}) was prepared as in system S2. An EDTA solution (La^{3+}+ Zr^{4+}: EDTA = 1:0.5) was prepared by dissolving EDTA in water. The pH of this solution is increased by addition of ammonia until the dissolution of EDTA. Then, the metal solution (La^{3+}+ Zr^{4+}) was slowly added to the EDTA solution at room temperature and stirred for 10 minutes. 2-amino2-methyl-1 propanol (AMP, Sigma- Aldrich, 95%) was added to this mixture to decrease the surface tension of this water based precursor and the solution is heated to 60°C. Finally, a stoichiometric amount of PVP (molar ratio of La^{3+}+ Zr^{4+}: PVP = 1:0.5) is added and the final solution is evaporated until the desired concentration is achieved. The pH of the solution is found to be 4.6-4.7 and the viscosity was 4.8- 5.0 mPa s.

5.2 Solution complexation, stability and gelation

5.2.1 Stability of alkoxides against hydrolysis

In systems S2, S3 and S4, the zirconium n-propoxide was stabilized by mixing it with acetic acid in order to handle it in non-vacuum conditions. The viscosity of zirconium n-propoxide is high due to molecular association of zirconium propoxide. According to Yi et. al, acetic acid partially replaces the propoxide ions (OPr) by acetate ions (OAc) forming a zirconium propoxide-acetate complex that reduces the chances of immediate hydrolysis and condensation reaction of zirconium propoxide on addition of water as shown in equation 5.1 [10].

$$2nZr(OR)_4 + 2n\ R'COOH \rightarrow 2nRO[\text{-}Zr\text{-}O\text{-}](OOCR')_2R + 4ROH \qquad (5.1)$$

Excess acetic acid dilutes the viscosity of zirconium n-propoxide and the propanol formed as the by-product of the reaction forms co-ordinate bonds with Zr^{4+} ion inhibiting the coordination linkage between zirconium propoxide acetate molecules [10]. We fix the molar ratio of Zr^{4+}: acetic acid at minimum of 1:4 because, this ratio yielded a stable zirconium-propoxide-acetate molecules stable against hydrolysis.

5.2.2 Complexation and increase in viscosity

In all systems, EDTA is used as a strong chelating agent to form complexes with both lanthanum and zirconium ions [5]. It was calculated from potentiometric titrations that, EDTA, forms stable complexes with Ce^{3+} ions at a pH around 5.5-6 [4]. The same condition was applied here. After the addition of the metal solution to the EDTA-EDA-water mixture, the pH dropped to 3. Hence, the pH of the final metal- EDTA mixture was increased by addition of ammonia to 6 in systems S1, S2 and S3. Ammonia is used in place of EDA to increase the pH to keep the organics at minimum. The following addition of ethylene glycol (EG) was to improve the viscosity and the wettability on the metallic substrates. It is believed that EG promotes the formation of polymeric species on reaction between EDTA and EG as EDTA plays the role of citric acid and is similar to a Pechini process [11]. Although, the salts used here are not nitrates as in Pechini method, there was a definite increase in the viscosity of the solutions after the addition of EG. Based on this, it

was assumed that, the EG promotes the formation of esters on reaction with the carboxylic acid groups of EDTA.

Systems S3 and S4 contain AMP (a surfactant) which is highly alkaline in nature. It serves the purpose of reducing the surface tension of the water based solution as well increasing the pH of the solution. The EDTA solutions used in system S3 and S4 are dissolved primarily in NH_4OH followed by addition of AMP. In system S4, AMP replaces EDA (for its high alkalinity) and EG (for its wettability and surface tension) used in system S1, S2 and S3. The final solutions of system S4 were found equally stable at lower pH of 4.6 similar to other systems which were maintained at pH 6.

5.2.3 Polymer addition

Finally, the polymer PVP was added to system S3 and S4 to increase the single layer thickness without cracks. PVP is considered to promote structural relaxation during the heat-up stage of the annealing treatment causing reduction in the stress during the formation of thin films [12]. This is believed to increase the critical film thickness [13]. PVP can also promote an increase in viscosity of the solution [14].

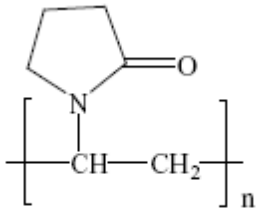

PVP

Figure 5.1: structure of PVP

The C=O of PVP caps the M-OH-M groups of the metals, preventing the occurrence of further condensation. Hence, the sudden shrinkage caused by the evaporation of the organic by-products (alcohol, water) during the heat-up stage is prolonged to higher temperatures wherein the nucleation begins. This alleviates the stress caused in the films during the heat-up stage which otherwise is relieved as cracks in the thin films. But, excess use of PVP causes pores in the thin films because it being a polymer and its burn-out during the

pyrolysis step leaves a huge void space. This followed by nucleation and crystal growth, cannot overcome the empty space left by the burnt-out of PVP. The critical limit of PVP and also its interaction with other organic species in the solution play an important role in the production of thicker films with dense morphology.

5.2.4 Gelation

A solution was considered stable when it did not precipitate at least for a few days of time. Following the criteria of preparing a stable solution, it is also necessary to get a good gel at 60˚C. A stable solution is selected by leaving the solution to evaporate at 60˚C for 12 hours. A clear gel indicates that the metal ions are dispersed homogeneously in a polymeric network and ensures growth of homogeneous metal-oxide under high temperature treatment. A typical optimized stable solution and gel, showing shelf-life stability of several weeks, is depicted in fig. 5.2a and 5.2b, respectively.

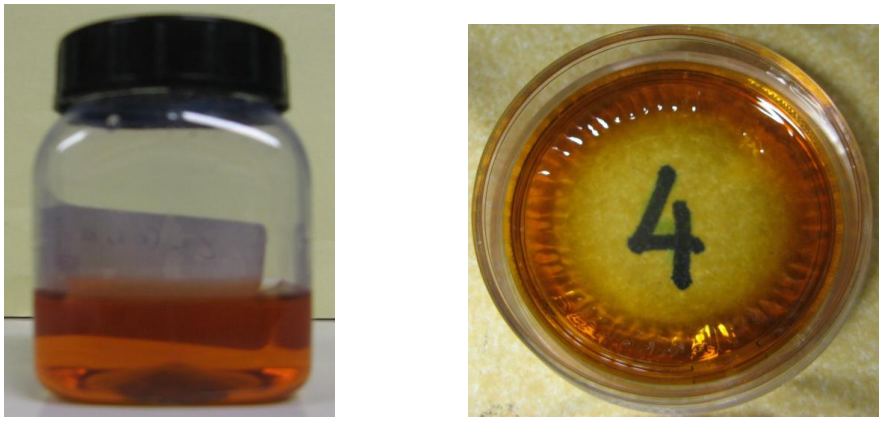

Figure5.2: a. Clear and stable solution b. Stable gel

5.2.4.a Effect of acetic acid on gelation: In all systems, a minimum of 1:8 molar ratio of total metal ions: acetic acid was required to obtain a stable and transparent gel. In this work, the molar ratio of total metal ions: acetic acid is fixed at 1:10. Although the solutions with less acetic acid looked stable, the gels obtained were white in color, because less acetic acid caused more free concentration of metal ions on excess solvent evaporation at 60˚C.

5.2.4.b Effect of EDA on gelation: In systems S1, S2, S3 a minimum ratio of EDTA: EDA was required to be 1:1.5. If the ratio was lower, the gels did not look transparent and clear.

Excess EDTA precipitated out due to change of pH (acidic) when the excess solvent was evaporated. In this work, the ratio of EDTA: EDA was maintained at 1:4 to obtain a clear gel. Also, use of EDA increased the viscosity of the solution which was profitable for water-based solutions.

5.2.4.c Effect of NH_4OH on gelation: In all the above systems, use of ammonia did not make a significant change on the gelation aspect. This is because, in systems S1-S3, EDA played an important role in keeping the gel transparent. In system S4, the use of AMP kept the gel clear and transparent in the network.

5.3 Solution deposition and treatment

Ni-5%W substrates of 1 cm wide and 80 µm thick (Evico, GmbH) were cut into strips of 3 cm length for cleaning and dip-coating as described in Chapter 3. The substrates were dip-coated in a clean room (class 10,000; flow cupboard class 100) to prevent contamination of dust particles. The dip-coat speed was maintained between 20-60 mm/min. The as-deposited layers were transformed into a gel by placing them in a drying furnace at 60°C for one hour. The amorphous layers were transformed into crystalline layers by a suitable heat treatment. Therefore, the as-deposited layers were first heated from room temperature to 450°C with a ramp rate of 1°C/min and let to dwell for one hour. Secondly, a 3°C/min heating rate was applied from 450°C until 900°C (dwell time = 1h). Finally, the films were heated to 1050°C at a 10°C/min ramp with a dwell time of one hour. After the heat treatment, the furnace was switched off and the samples were left to cool inside the furnace. The entire heating process was carried out in an Ar-5%H_2 atmosphere (gas flow 0.1L/min- 0.55 L/min).

5.4 Results and discussion

5.4.1 Crystallinity and orientation

Fig. 5.3a and 5.3b depicts the θ -2θ scans of the LZO layers of the systems S1-S4 by a normal X-ray diffractometer. Crack-free LZO layers of 100- 120nm thickness dip-coated at a speed of 40mm/min were chosen for system S1 and S2. Crack-free LZO layers of 280 nm thickness and 140 nm thickness, dip-coated at a withdrawal speed of 60mm/min obtained from systems S3 and S4 respectively were considered. The crystallinity and texture of the LZO films can be estimated by the peak intensity ratios**,** represented as:

$$\text{Intensity ratio's} = \frac{I_{max,(004)}}{[I_{max,(004)} + I_{max,(222)}]} \times 100\% \qquad (5.2)$$

A strong (0 0 4) reflection indicates good c- axis growth as calculated from the peak intensity ratio values. They were found to be 95.20%, 92.50%, 88.90%, and 95.12% respectively for the systems.

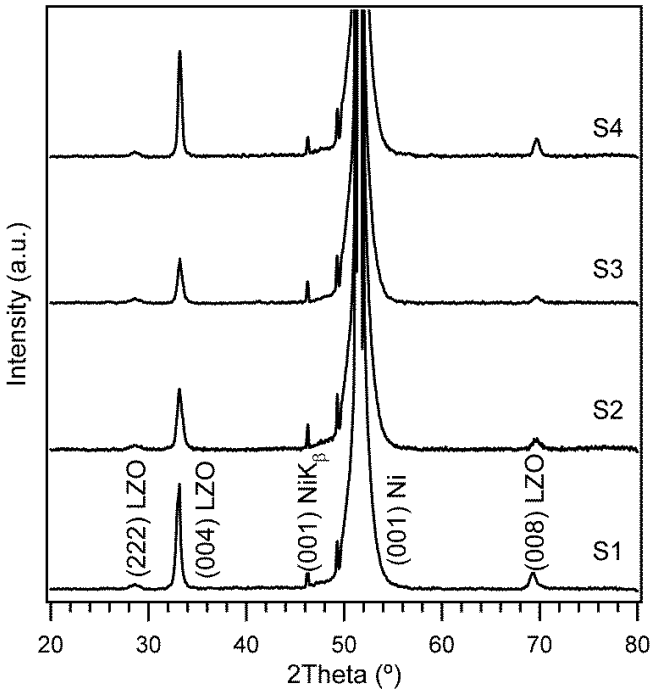

Figure 5.3: θ -2θ diffraction patterns of LZO systems S1-S4

Fig. 5.4 represents the phi-scans carried-out to measure the in-plane misalignment of the (2 2 2) plane of the LZO films.

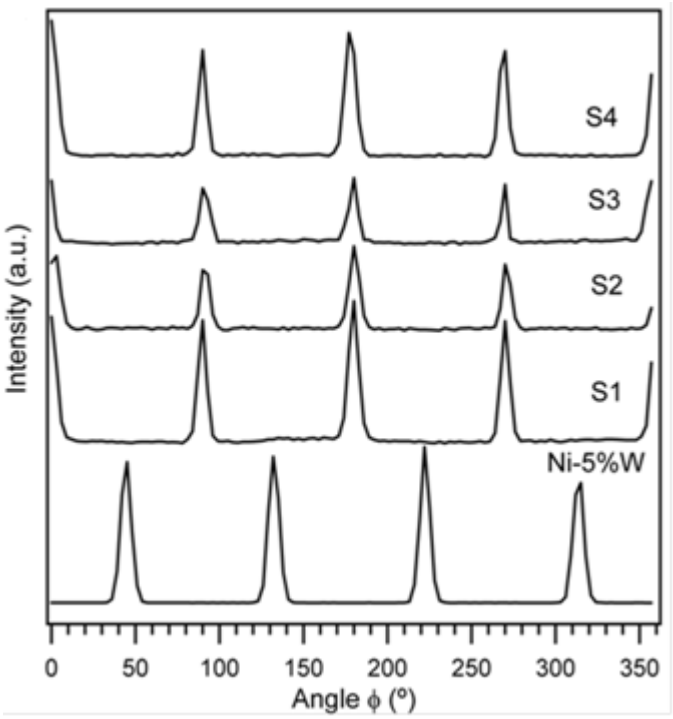

Figure 5.4: ϕ - scan of LZO systems 1a, 2a, 2b, 2c and 4 at 2θ= 28.62˚ and Ψ= 54.00˚

The average FWHM of the peaks of system S1-S4 were found to be 6.10°, 6.75°, 6.45° and 6.59°. These values are very close to the FWHM of 6.1° of the Ni-5%W substrate, which illustrates that the biaxial texture was successfully transferred. Fig. 5.5a and 5.5b display the pole-figures of the Ni-5%W substrate and that of system S1.

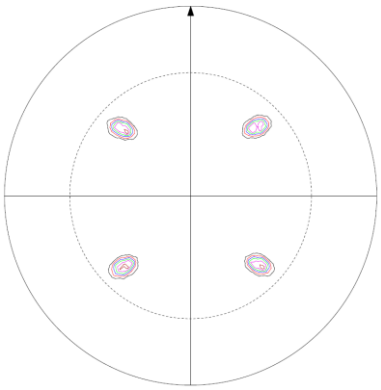

Figure 5.5a: Pole –figure of Ni-5%W substrate

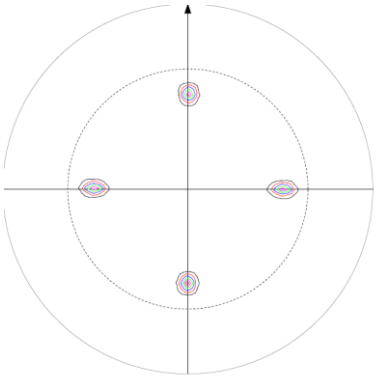

Figure 5.5b: Pole –figure of LZO system 1

Fig. 5.5b supports the fact that the LZO thin film has grown with a 45° grain rotation on top of the substrate to accommodate the lattice mismatch and maintain the biaxial texture [15, 16]. The out-of-plane misalignment was measured by rocking curve measurements along the (0 0 4) plane of LZO. This is depicted in fig. 5.6 for these LZO systems.

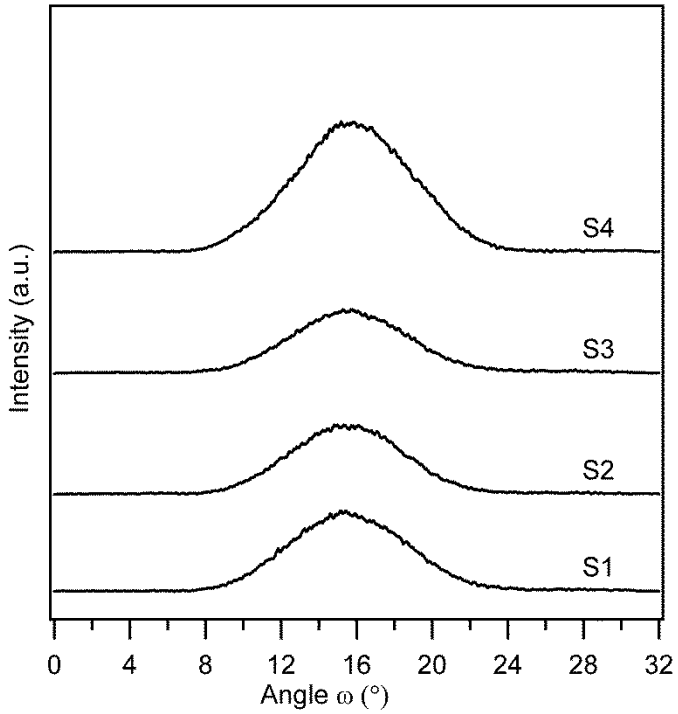

Figure 5.6: Rocking curve measurement along (004) plane of LZO systems

The FWHM of the systems S1-S4 were found to be 7.20°, 7.20°, 7.08° and 7.42° respectively. The surface orientation and the crystallinity of the top-surface were verified by RHEED analysis (Table 5.2).

Viewing direction	**S1**	**S2**	**S3**	**S4**
<100>	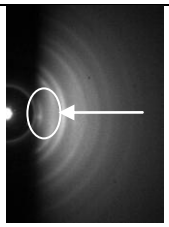	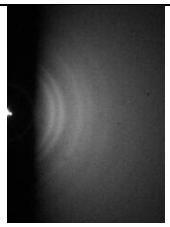	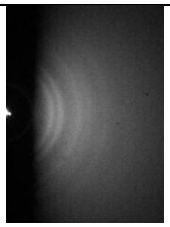	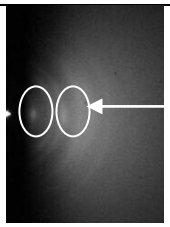
<110>	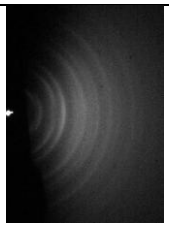	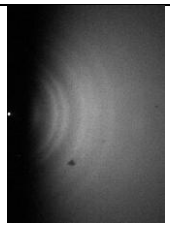	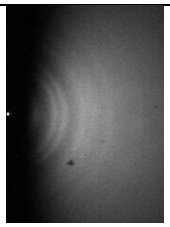	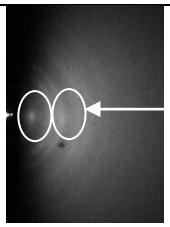

Table 5.2: RHEED pattern of the LZO systems

For all these systems, a typical ring like structure is found. This implies that the top surfaces of the films are polycrystalline or random textured. There are some discrete spots (marked by circles and arrows) inside the ring like structure in the RHEED pattern for system S1 and system S4 implying the presence of a small percentage of biaxial texture.

5.4.2 Electron microscopic analysis: SEM and TEM

Figure 5.7 (a-d) displays SEM micrographs (magnification 50K) of the four different LZO layers. A dense surface is required to prevent diffusion of nickel atoms into the YBCO layers and to prevent diffusion oxidation of the Ni-5%W substrate during YBCO deposition.

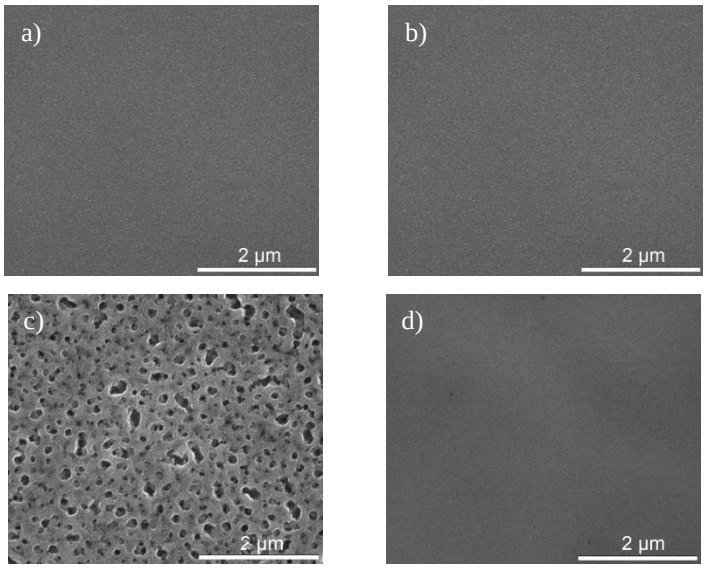

Figure 5.7 a- d: SEM images of the LZO systems 1a and 2a-2c respectively

Systems S1, S2 and S4 show a dense morphology. However, system S3 looks very porous. Choi et al. had concluded that in a system conatining PVP, there are chances of surface porosity [13]. Basically, these pores were regarded as the reason for the suppression of the formation of large cracks by relieving the stress on the film thereby increases the crack-free thickness [17]. Kozuka et al. in their work on PVP addition to thin films indicated that slow-heating ramp during pyrolysis prevented any pores caused due to PVP addition [12]. System S4 despite the presence of an equal molar ratio of PVP as in system S3, showed an entirely different morphology under SEM. It can be proposed that in the solution state of system S3, EDTA-EDA-EG-PVP forms a longer length polymeric chain compared to that of EDTA-AMP-PVP polymeric chain in system S4. Hence, during the burn-out of this long length polymeric chain (system S3), large pores are left out on their surface (fig.5.7c).

A TEM analysis was performed on two selected systems: system S2 and system S4. The TEM images are shown below in table 5.3.

LZO thin film	TEM image at Ni-5%W and LZO interface	At higher magnification
System S2	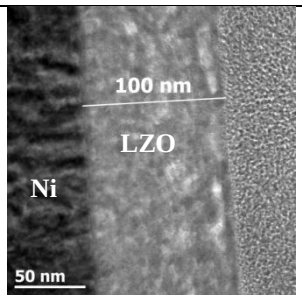	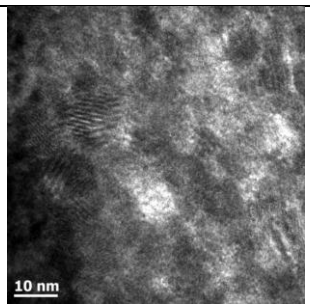
System S4	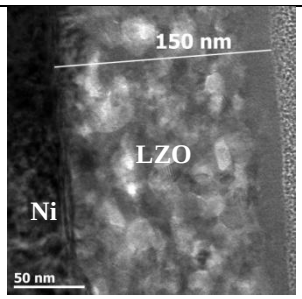	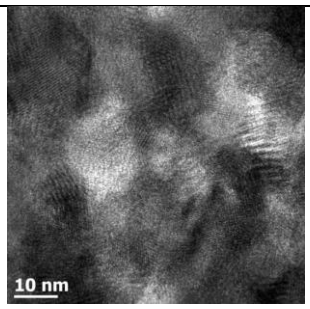

Table 5.3: TEM images of system S2 and S4

From the images above, we can infer that both systems contain nanovoids. These are the white areas seen amidst the darker regions in the images.The size of the nanovoids is ranging anywhere between 10 to 20 nm. Their size is in agreement with that of the nanovoids reported by other groups [18, 19]. Molina et al. have done extensive TEM analysis on these nanovoids and concluded that they are filled with carbon-rich gases which are formed during chemical reactions [19] In the work of Jiménez et al. it was observed that the nanovoids were formed even in their amorphous state at 500°C and these voids did not affect the final crystalline state formed at 960°C [18]. Also, a slower heating rate was considered good for crystallinity but detrimental for compactness of the thin film. Their work stated the possibility of colaescence of nanovoids under slow heating rate (100°C/h) causing percolation of voids resulting in connected nanovoids [18] Cloet et al. in their work described that, these nanovoids can be attributed to the growth of the LZO layers in an Ar-5%H_2 atmosphere [20]. Since LZO is an oxide that is grown under reducing Ar-5%H_2

atmosphere, it was proposed that the occurrence of nanovoids could be due to the use of reducing gas flow that impaired the growth of completely dense crystalline LZO oxide.

5.5 Texture improvement by gas flow control and seed layers

Since LZO buffer layers require both a thickness high enough to prevent inter diffusion of O and Ni and a highly crystalline surface to ensure transfer of texture to the YBCO layer grown on top, an attempt was made to further improve the top surface (2-5 nm) crystallinity following the results from table 2. Given the best results so far were obtained for system S4, focus was directed on this system. The various changes made to the protocol are the following:

5.5.1 Gas flow and heating ramp

Sample 1: Since the reducing gas can be detrimental for oxide formation, the flow was minimized to 0.1L/min from 0.55L/min for thin films deposited at a withdrawal speed of 60 mm/min. This reduction in gas flow is combined with an unchanged heat treatment. **Sample 2:** The lower gas flow of 0.1L/min is combined with a faster heating rate of 10 C/min till 600°C (dwell =1h) and at 10°C/min till 1050°C (dwell time= 1h). The withdrawal speed of the thin film was maintained at 60 mm/min.

5.5.2 Introduction of seed layer and changes with gas flow and heating ramp

A seed layer of a few nanometer thickness has been used by several investigators to improve the crystallinity of oriented layers [21-23]. The seed layers play a significant role in relieving the stress in the films and also act as nucleating centers for the to-be deposited thick film [24].

Seed layers of 15-40nm thickness were deposited on the Ni-5%W substrates. Afterwards, the usual deposition of the films prepared from system S4 is followed by the standard heat-treatment.

Sample 3: A seed layer prepared from a 0.2M LZO precursor solution [16] was deposited at a withdrawal speed of 30mm/min and heat-treated at 5°C/min till 900°C (dwell= 50

minutes) and at 10°C/min till 1050°C (dwell= 50 minutes). The gas flow was maintained constant at a rate of 0.4L/min. The seed layer thickness was found to be 15nm.

Sample 4: A seed layer was prepared from 0.4M LZO at a withdrawal speed of 30mm/min, heat-treated at 5°C/min till 900°C(dwell= 50 minutes) and at 10°C/min till 1050°C (dwell= 50 minutes) under a constant gas flow of 0.4L/min. A 40nm thick seed layer was obtained.

Sample 5: A seed layer prepared from 0.2M LZO [22] at a withdrawal speed of 30mm/min was heat-treated at a slower heating ramp of 1°C /min during the pyrolysis step. The gas flow was maintained constant at a low rate of 0.1L/min. The thickness of the seed layer was found to be 15nm.

The RHEED results from these layers are shown below (Table 5.4):

Viewing direction	**Sample 1**	**Sample 2**	**Sample 3**	**Sample 4**	**Sample 5**
<100>	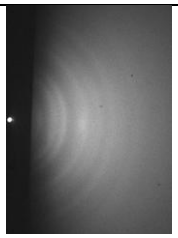	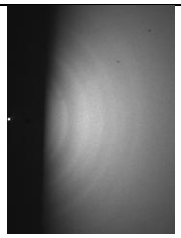	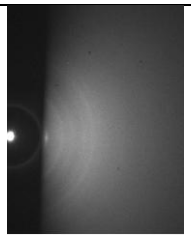	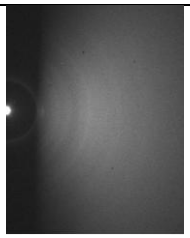	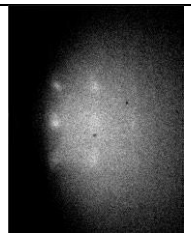
<110>	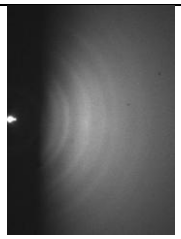	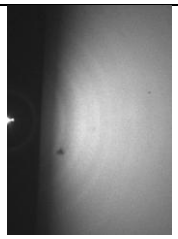			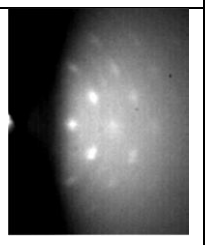
Thickness (nm)	~140	~135	~150	~180	~150

Table 5.4: RHEED analysis of the LZO layers with modifications in various parameters

As can be seen from Table 4, only sample 5, the LZO layer prepared with a seed layer of 15 nm at slow heating rate of 1°C/min shows a spotted pattern in RHEED analysis,

confirming the presence of a significant amount of crystalline top surface of the layer and transfer of the texture from the substrate to the buffer layer. Sample 1 prepared at low gas flow showed random texture and sample 2, prepared at low gas flow and with a fast heating ramp even shows a completely amorphous surface. These results indicate that varying gas flow and heating rate does not significantly improve the surface texture of the thick LZO samples. Sample 3 and 4, both prepared with an additional seed layer of 15 and 40 nm respectively, exhibit an amorphous top surface. The differences between sample 3, being amorphous, and sample 5, showing good quality top surface, is the decrease in heating rate from 5°C/min to 1°C/min during the pyrolysis step of the seed layer and also the reduction of gas flow from 0.4L/min to 0.1L/min. Therefore, we conclude that in the case of the use of seed layers, heating rate and gas flow influence the final quality strongly. This is in contradiction with results for the one step processed thick LZO layers for sample 1 and 2 where the change in heating rate and gas flow did not significantly improve the crystallinity of the top-surface This can be interpreted by the fact that, as-deposited seed layer of 15 nm is quite mobile and a high gas flow and heating ramp can distort the wet layer easily. This distortion of wet film causes the growth of LZO seed layer with comparatively less epitaxial growth. Since these act as nucleating centres for the further growth of thick LZO films passing on its epitaxy, the RHEED analysis shows less crystallinity on the top surface of the layer.

5.6 Discussion on PVP addition, pore formation and increased thickness

To study the influence on the surface morphology, increased amount of PVP was incorporated in systems S3 and S4. PVP in molar ratios of 0.25, 1.0 and 1.5 with respect to total metal ions was introduced in systems S3 and S4. Table 5.5 gives the overview of the morphology and thickness of the LZO films containing various ratios of PVP.

Ratio of Total metals: PVP	S3	Thickness (nm)	S4	Thickness (nm)
1:0.25	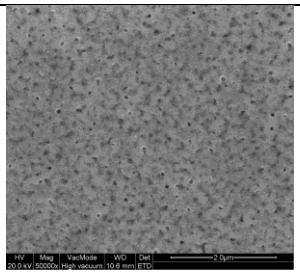	280 at 80mm/min	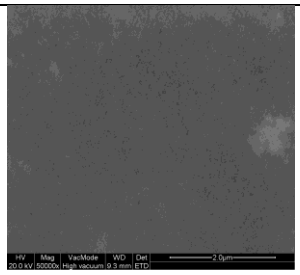	130-140 at 60 mm/min
1:1	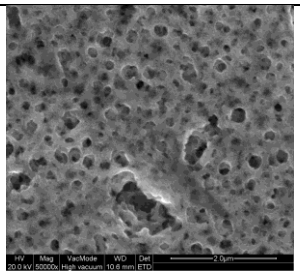	350 at 80mm/min	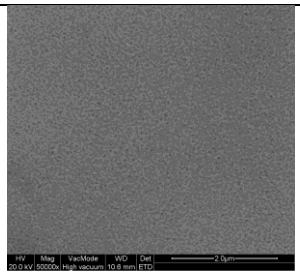	250-280 at 80 mm/min
1:1.5	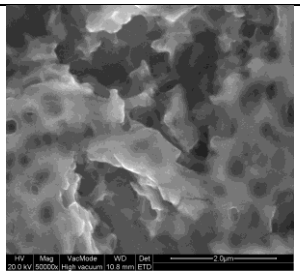	350 at 60mm/min	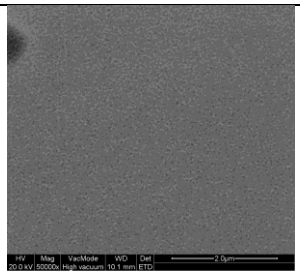	280 at 60mm/min

Table 5: SEM pictures of the systems containing various ratios of Metal ions: PVP

From the table above, we can clearly see that, increase in PVP for system S3 caused dramatic increase in pore size whereas the system S4 showed mild increase in pores with increase in PVP. Nevertheless, both systems show increase in the viscosity of the solution with increase in PVP as well as increase in thicknesses. This is in agreement with the previous statement that, in system S3, EDTA-EDA-EG-PVP forms a longer length polymeric chain compared to that of EDTA-AMP-PVP polymeric chain in system S4.

5.7 Conclusions

This research work presents a series of chemical solution deposition routes suited for the preparation of thick, crack-free LZO films from water-based precursors.

It is seen that the addition of a polymer was beneficial in increasing the single layer thickness, but it also created a porous surface in one of the formulations. The pores created in the layers are found to be inter-dependent on the total chemical composition of the solution and not on the mere presence of the specific polymer. Presence of AMP in the solution state of system S4, helped the formation of non-porous layers even in the presence of polymeric PVP. The TEM studies revealed the presence of nanovoids in the layers, which is inherent to all LZO films.

The best LZO layer acted as a good barrier against Ni penetration (discussed in chapter 6). A seed layer was incorporated in order to improve the crystallinity of the top surface of the LZO layer to support the growth of textured YBCO. Finally, a thick and high quality LZO layer from the water-based precursor solution, with improved biaxial texture on the top surface was obtained.

References

[1] I. Van Driessche, G. Penneman, E. Bruneel, S. Hoste, Pure Appl. Chem. 74 (2002) 2101-2109.

[2] I. Van Driessche, S. Cattoir, S. Hoste, Appl. Supercond. 2 (1994) 101-110.

[3] V. Cloet. Synthesis and microstructure analysis of $La_2Zr_2O_7$ buffer layers for coated conductors. PhD thesis, Ghent University, 2010.

[4] T. Thuy Tran, S. Hoste, G. Herman G, N. Van de Velde, K. De Buysser, I. Van Driessche, J. Sol-Gel Sci. Technol. 51 (2009) 112-118.

[5] A. E. Martell, R. M. Smith, Critical stability constants, Vol. 2, Plenum press, New York, 1975.

[6] S.N.B. Hodgson, X. Shen, F.R. Sale, J. Mater. Sci. 35 (2000) 5275-5282.

[7] J. R. Mc Bride, K. C. Hass, B. D. Poindexter, W.H. Weber, J. Appl. Phys.76 (1994) 2435-2438..

[8] V. Bellière, G. Joorst, O. Stephan, F. M. F. de Groot, B. M. Weckhuysen, J. Phys. Chem. B 110 (2006) 9984-9992.

[9] B. C. Morris, W. R. Flavell, W. C. Mackrodt, and M. A. Morris, J. Mater. Chem. 3 (1993) 1007-1110.

[10] G. Yi, M. Sayer, J. Sol-Gel Sci. Technol. 6 (1996) 65-74.

[11] M.S. Bhuiyan, M.P. Paranthaman, K. Salama, Superconductor. Sci. Technol. 19 (2006) R1-R21.

[12] H. Kozuka, A. Higuchi, Journal of Materials Research 16 (2001) 3116-3123.

[13] J.J. Choi, J.H. Jang, D.S. Park, B.D. Hahn, W.H. Yoon, C. Park, Jpn. J. Appl. Phys. 46 (2007) 3549-3555.

[14] Z. Wang, J. Liu, T. Ren, L. Liu, Sensor Actuat. A Phys. 117 (2005) 293-300.

[15] K. Knoth, R. Hühne, S. Oswald, L. Schultz, B. Holzapfel, Acta Mater. 55 (2007) 517-529.

[16] V. Cloet, J. Feys, R. Hühne, S. Hoste, I. Van Driessche, J. Solid State Chem. 182 (2009) 37-42.

[17] G. T. Park, C. S. Park, J. J. Choi, J. W. Lee, H. E. Kim, J. Am. Ceram. Soc. 89 (2006) 2314-2316.

[18] C. Jiménez, T. Caroff, L. Rapenne, S. Morlens, E. Santos, P. Odier, F. Weiss, J. Cryst. Growth 311 (2009) 3204-3210.

[19] L. Molina, K. Knoth, S. Engel, B. Holzapfel, O. Eibl, Superconductor Sci. Technol. 19 (2006) 1200-1208.

[20] V. Cloet, P. Lommens, R. Hühne, K. De Buysser, S. Hoste, I. Van Driessche, J. Cryst. Growth DOI 10.1016/j.jcrysgro.2011.04.029 (2011).

[21] R.W. Schwartz, T. Schneller, R. Waser, C. R. Chimie 7 (2004) 433-461.

[22] X.B. Zhu, S.M. Liu, H.R. Hao, P. Tong, C.X. Wang, W.H. Song, Y.P. Sun, K. Shi, Z.Y. Sun, S. Chen, Z. Han, Scripta Mater. 51 (2004) 659-663.

[23] X.B. Zhu, H.C. Lei, D.Q. Shi, L. Zhang, L. Wang, Y.P. Sun, W.H. Song, Z.R. Yang, J.H. Kim, R. Zeng, S.X. Dou, J. Yang, H.W. Gu, Phys. C Superconductivity 467 (2007) 73-79.

[24] M.P. Paranthaman, M.S. Bhuiyan, S. Sathyamurthy, L. Heatherly, C. Cantoni, A. Goyal, Phys. C Superconductivity 468 (2008) 1587-1590.

Chapter-6

XPS depth profiling for evaluation of LZO buffer layer capacity

Lanthanum zirconate (LZO) films as described in Chapter 5 were deposited on Ni-5%W tape, in order to act as a bufferlayer. These layers, prepared by aqueous solution-gel dipcoating, were tested as to how they protect a subsequently deposited superconducting YBCO film from Ni penetration by treating them under simulated YBCO conditions. XPS depth profiling was used in this chapter to study their barrier efficiency and the effect of an additional oxygen annealing step, which simulates the thermal treatment for YBCO thin film synthesis

6.1 Buffer layers and thickness necessity

As seen in chapter 5, $La_2Zr_2O_7$ (LZO) is used as one of the prominent buffer layer because of its closed packed pyrochlore structure with a lattice parameter of 10.79 Å. It has a low lattice mismatch to both YBCO (0.5% and 1.8% mismatch to YBCO (oxidized), a- and b- axes, respectively) and 8% to textured Ni-5%W substrate. [1]. Many different kinds of deposition techniques can be adopted for the deposition of the buffer layers. CSD is one of the cheapest and easily adaptable methods to suit the needs of the buffer layer deposition under non-vacuum conditions.

Recently Caroff et al. [2] have reported that, LZO layers of at least 150 nm thickness are required to ensure a sufficient texture quality and to absorb most of the defects of the substrate (150 nm > LZO thickness > 250 nm) [2]. Based on this comment, single and crack-free thicker LZO layers from LZO precursor solutions using water as main solvent were formulated (Chapter 5). The earlier published LZO layers by our group [3] were too thin and new water-based precursor solution needed to be synthesized. Newly prepared LZO layers of up to 150 nm thickness using water based solutions are considered in this chapter. The performance of these buffer layers were compared to non-water based layers deposited by Zenergy Power GmbH with a single layer thickness of 145 nm and a double layer thickness of 280 nm.

Earlier, XPS has been used as an effective tool in optimization of the performance of the LZO buffer layer by studying the in-depth composition of the elements and the inter-diffusion thickness of the Ni substrate and the LZO layer [4]. These layers were prepared under reducing conditions to prevent oxidation of the Ni-5%W substrate. Technically, these LZO buffer layers annealed under reducing conditions (in Ar-5%H_2 gas) are further processed by depositing YBCO on top of them, under oxidizing conditions. The effective action of the buffer layer is to prevent the oxidation of the Ni-5%W substrate and penetration of Ni into the YBCO layer during the YBCO annealing under oxidizing conditions. There are reports that indicate that nickel oxide (NiO) is formed during the annealing step on the interface of the substrate and LZO layer after deposition of YBCO [5]. Also for MOCVD YBCO deposition in inert conditions in low O_2 conditions at 800^{o}C followed by an oxygen annealing at 500^{o}C did not cause oxidation of the

Ni-tape. Here, we process the as-prepared LZO buffer layers (water-based and non-water based layers) under YBCO processing conditions (in oxygen atmosphere) without depositing YBCO. Their buffer layer action is compared with that of the as-prepared LZO buffer layers (water-based and non-water based layers) prepared under reducing conditions using XPS. Totally 7 different LZO layers under as-prepared and under YBCO annealing conditions were studied using XPS.

6.2 Experimental methods

6.2.1 Synthesis of precursor solutions

System 1 is a La acetate- Zr acetate-sol with TEA and acetic acid. The precursor solution was prepared using lanthanum acetate, $La(CH_3COO)_3.1H_2O$, zirconium(IV)hydroxideacetate, $Zr(OH)_3(CH_3COO).H_2O$, and acetic acid dissolved in water with triethanolamine (TEA) as a complexing agent. The acidity was set at pH 7 using ammoniumhydroxide. The procedure for the following solutions was described in more detail previously [3, chapter 5]. In the resultant sol with a viscosity of 3.9 mPa.s the concentrations are 0.17 M La^{3+}; 0.17 M Zr^{4+}; 0.67 M TEA and 3.3 M acetic acid.

In system 2 a stoichiometric mixture of lanthanum acetate and zirconium n-propoxide (70% w/w in n-propanol) was diluted with acetic acid and water. Then we added a solution of ethylenediammine tetraacetate (EDTA) and ethylenediammine (EDA) solution. The pH of the mixed solution was adjusted to 6 by adding ammonia. Finally ethylene ethylene glycol (EG) was added to the solution at 60°C, in order to increase the wettability and the viscosity of the solution. This solution was stirred and an excess of solvent was evaporated until a concentration of 0.2 M La^{3+}; 0.2 M Zr^{4+} ; 0.8 M ethylene glycol; 1.6 M EDA; 0.2 M EDTA and 4 M acetic acid was obtained.

In system 3 the zirconium precursor from system 2 was replaced by zirconium-hydroxideacetate because it is soluble in water and has a shorter carbon chain, minimizing the amount of organic material that has to be burned off. Zirconiumhydroxideacetate hydroxide and lanthanum acetate were dissolved in water at room temperature. After heating and addition of acetic acid, a solution of EDTA and EDA was added. The sol was neutralized towards a pH of 6 with ammonia and EG was

added. Finally the sol was heated until the final concentration of the solution reached 0.2 M La^{3+}; 0.2 M Zr^{4+} ; 0.8 M ethylene glycol; 1.6 M EDA; 0.2 M EDTA; 4 M acetic acid.

System 4 is a water based La acetate- Zr propoxide-sol with polyvinyl pyrrolidone (PVP). The preparation method is the same as in system 2 but prior to evaporation polyvinyl pyrrolidone (PVP, Alfa- Aesar, MW 8000) was added to the solution, PVP is known to cause stress relaxation while heating up the gel, which makes it possible to synthesize thicker crack free films [6]. The final concentration of the solution reached 0.2 M La^{3+}; 0.2 M Zr^{4+} ; 0.8 M ethylene glycol; 1.6 M EDA; 0.2 M EDTA; 4 M acetic acid and 0.5 M PVP(monomer).

System 5 is a water based La acetate-Zr propoxide sol with polyvinylpyrrolidone in which ethylene glycol and EDA were replaced by 2-amino-2-methyl-1-propanol (AMP). The final concentration is 0.2 M La^{3+}; 0.2 M Zr^{4+} ; 0.8 M AMP ; 0.2 M EDTA; 4 M acetic acid and 0.5 M PVP(monomer).

Solutions prepared in system 2, 3, 4 and 5 can be correlated to systems S2, S1, S3 and S4 in chapter 5. All the above prepared solutions were filtered using a 0.2 µm filter prior to dipcoating and showed to be stable for at least 4 months. An overview of the different precursor solutions is given in table 6.1.

Table 6.1: Overview of LZO layers

	Precursor salts	Complexing agent	Additives	Polymer	Thickness
Layers prepared by sol-gel dipcoating					
System 1	La-acetate Zr-acetate hydroxide	TEA	Acetic Acid, TEA, NH_4OH	-	40 nm[a]
System 2	La-acetate Zr-propoxide	EDTA	Acetic Acid, EDA, EG NH_4OH	-	110 nm[a] 100 nm[b]
System 3	La-acetate Zr-acetate hydroxide	EDTA	Acetic Acid, EDA, EG NH_4OH	-	90-95 nm[a] 70 nm[b]
System 4	La-acetate Zr-propoxide	EDTA	Acetic Acid, EDA, EG	PVP	280 nm[a, b]

			NH_4OH		
System 5	La-acetate Zr-propoxide	EDTA	Acetic Acid, AMP NH_4OH	PVP	125 nm[a]- 150 nm[b]
Commercial layers					
Commercial 1					140-145 nm
Commercial 2 (double)					275-280 nm

[a]by ellipsometry

[b]byTEM

6.2.2 Deposition and heat treatment

Ni-5%W tapes were cleaned as per description in chapter 3 and cut into pieces of 2.5 cm length. For deposition of systems 2 and 3, the withdrawal speed was 40 mm/min and for system 4 and 5 it was kept at 60 mm/min. The as-deposited layers were transformed into a gel by drying at 60°C for one hour. Then they were first heated from room temperature to 450°C (ramp 1°C/min) for 30 minutes. Next, a 3°C/min heating rate was applied from 450°C until 900°C (dwell time = 1h). Finally, the films were heated upto 1050°C at 10°C/min with a dwell time of one hour. After the heat treatment, the furnace was switched off and the samples were left to cool inside the furnace. Conditions for system 1 are described elsewhere [3]. In this synthesis the processing at high temperature is somewhat less envasive, the film was heated towards 900°C with a heating rate of 5°C/min. After a restrained dwell time of 50 minutes, the temperature was rapidly increased to 1050°C and again maintained constant for an isothermal heat treatment of 50 minutes. The sample was cooled down to room temperature at a rate of 10°C/min. All thermal treatments were carried out in forming gas (Ar-5%H_2) at a constant gas flow between 0.4 and 0.55 L/ min.

A duplicate of each sample was additionally annealed in a gas flow of 200 ppm O_2 in N_2. The temperature was increased from room temperature to 815 $^{\circ}$C at a rate of 10 °C/min. After 150 min the temperature was decreased to 400 °C at a rate of 3°C/min. During this cooling ramp, the atmosphere was switched to oxygen (industrial quality) at 525 °C. After an annealing step of 5 h, the samples were furnace-cooled to room

temperature. This annealing step is identical to the heat treatment suitable for synthesis of YBCO thin films from an aqueous solution [7].

6.2.3 Determination of the thickness and microstructure of the buffer layer

The thickness of the layers was analyzed by spectroscopic ellipsometry (J. A. Woollam Co), fitting the experimental curve to model for LZO films on Ni-5%W substrates (wavelength = 638.3nm and refractive index= 1.998). The microstructure of the surface was analyzed with a scanning electron microscope (FEG-SEM, FEI). Thickness was verified using a C_s corrected transmission electron microscope (TEM, JEOL 2200 FS) after an in-situ lift-out procedure with FIB (FEI, Nova 2000).

6.3 XPS analysis for evaluating buffer layer capacity

The ability of the buffer layer to withstand migration of Ni towards the surface was evaluated by XPS depth profiling. (S-probe, Surface Science Instruments, VG with an monochromatic AlKα-source, 1486.6 eV). The voltage and power of the source were kept constant at 10 KV, 200 W. Sputtering of an area of 3 x 3 mm^2 for 40 seconds was performed with an Ar ion gun (4 KV) resulting in a sputterrate for Ta_2O_5 of 0.15 nm/sec. After each consecutive sputter cycle an area of 250 x 1000 μm^2 was analyzed. Regions for O 1s, C 1s, Zr 3d, La $3d_{5/2}$, Ni $2p_{1/2}$ and W 4f peaks were registered with a resolution of 0.15 eV. Peak areas were converted into atomic concentrations with the software package CasaXPS (Casa Software Ltd., UK) using a Shirley background and scoffield sensitivity factors.

All layers exhibit crack free surfaces, unless stated otherwise, as is shown in fig. 6.1 for a layer synthesized using solgel system 2. The sample thickness of the LZO layers is given in table 1. The values for the thickness determined by ellipsometry is in accordance with the results from TEM measurements. In fig. 1b a TEM bright field image of a cross section throughout the LZO layer is shown. Bright areas in the LZO layers can be correlated to nanovoids [8].

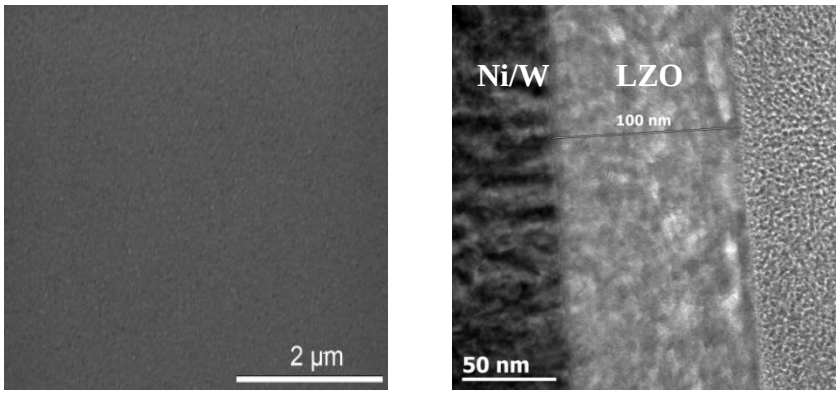

Figure 6.1: Thin layer from solgel system 2. a) SEM of surface b) TEM of cross section.

Fig. 6.2 shows the results of the XPS depth profiling for samples synthesized using solgel system 1 before and after annealing. From the figure 6.2a, it is observed that on top of the sample mainly carbon is observed due to a thin layer of surface contamination. After one sputter cycle the majority of the carbon has been sputtered off and predominantly La, Zr and Oxygen peaks are registered.

The observed stoechiometry of La/Zr in the XPS measurements is not exactly 1:1. The use of standards for the determination of correction factors could compensate for this apparent off stoichiometry [7]. However there is no physico-chemical reason to doubt the constitution of the LZO layers, thus no calibrations were performed. Nevertheless for each sample the presence of phase pure $La_2Zr_2O_7$ was confirmed with XRD/RHEED analysis.

The sputter rate of $La_2Zr_2O_7$ was determined by comparing the thickness of the film with the time needed to sputter through the $La_2Zr_2O_7$ layer. More precisely the time till Zr and La concentrations diminish till half their maximum value. This coincides with the point where the nickel concentration has increased until half its maximum value. In system 1, fig. 6.2a, this is after approximately 250 seconds, for a 40 nm thick LZO film. From this we calculate a sputter rate of 0.16 nm/sec. As performed for all samples, the estimated average sputter rate for LZO is 0.17 ± 0.1 nm/sec, or 1.13 times faster compared to the sputter rate of Ta_2O_5. The thickness of the LZO layer is marked with a (light + dark) grey box on the graphs. The time it takes for the Zr and La concentration to diminish to half of their maximum value was taken as a limit. This approximately

coincides with the point where the nickel concentration has increased until half its maximum value. The nickel-free zone is marked with a dark grey box.

The Ni $2p_{1/2}$ and W 4f peaks were first observed after 200 seconds of sputtering. Based on the sputter rate of $La_2Zr_2O_7$ we can conclude that the nickel free region on top of the sample is no more than 34 nm. After 400 seconds of sputtering the Zr and La peaks disappeared from the spectra. Small oxygen and carbon peaks remained visible in the interior part of the sample, fig 6.3 a, c. The shifts in the peaks with different sputtering times can be attributed to the surface O-H bonds that cause energy shifts in oxygen and carbon peaks on the surface compared to that of the inner layers.

Annealing this sample, thus mimicking an YBCO deposition, resulted in an increase in diffusion of all elements, fig 6.2b. The steepness of the curves vastly decreases and the region where both Ni/W and La/Zr are present is doubled. From the high percentage of oxygen in the inner part of the sample and the shift in oxygen peak position, fig. 6.3d, we conclude that during the annealing process the substrate is severely oxidized, confirming the observations made by V. Cloet et al. by TEM [5]. In the mean time the carbon content inside the layer disappeared, presumably it was oxidized by the penetrating oxygen fig. 6.3b.

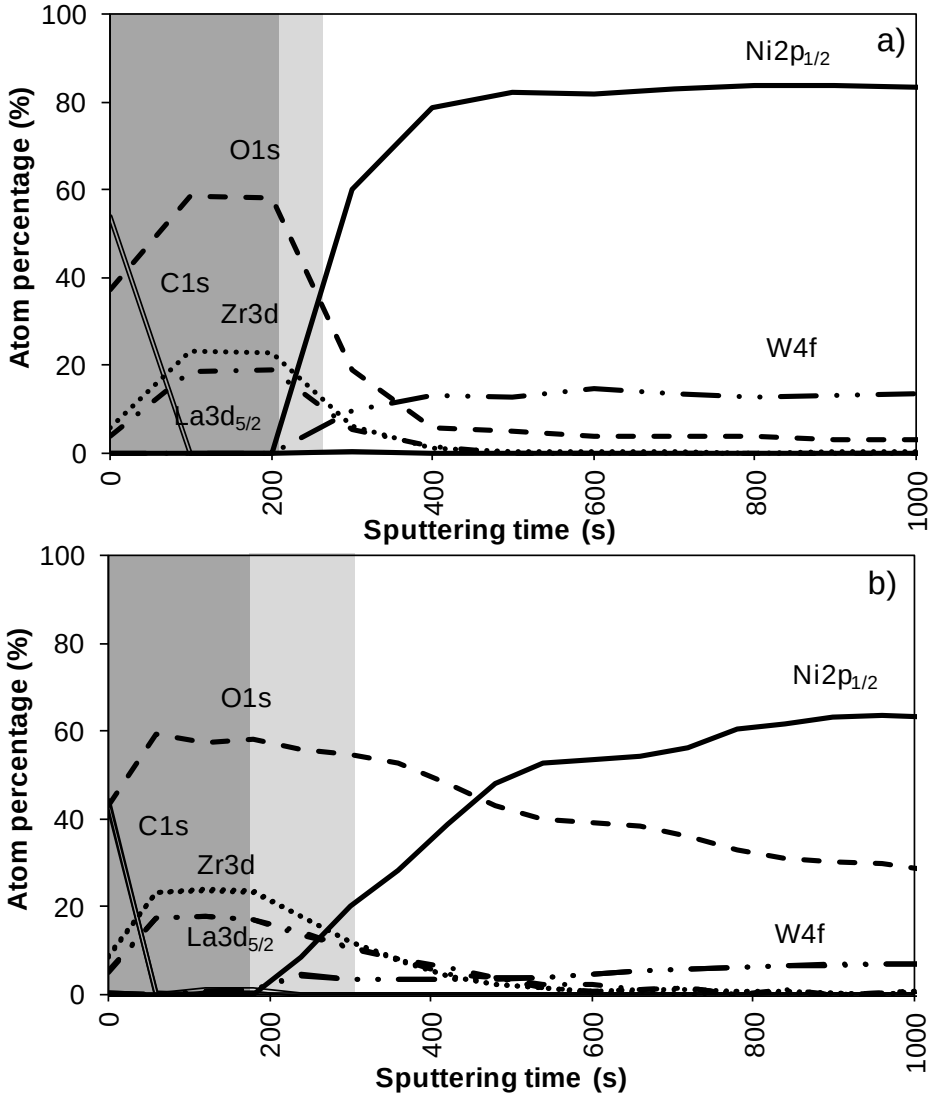

Figure 6.2(a-b): XPS depth profile, sample using sol gel system 1 a) before and after b) simulated oxidation treatment.

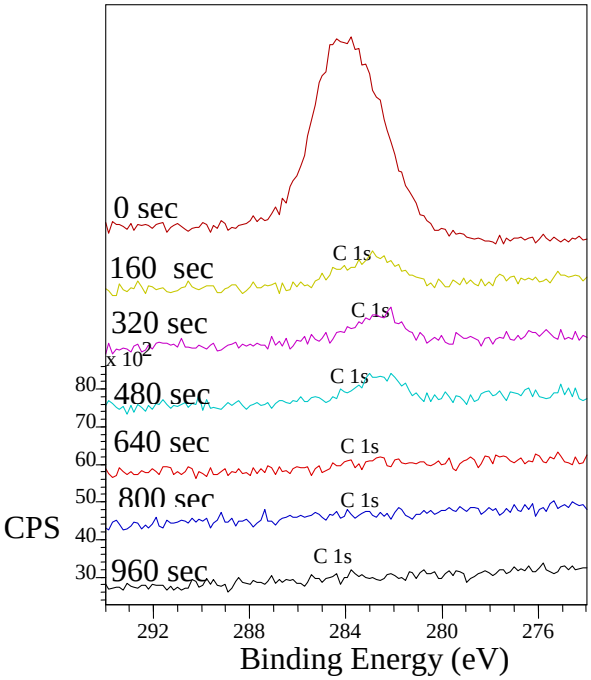

Figure 6.3a: Carbon 1s region of a sample from system 1

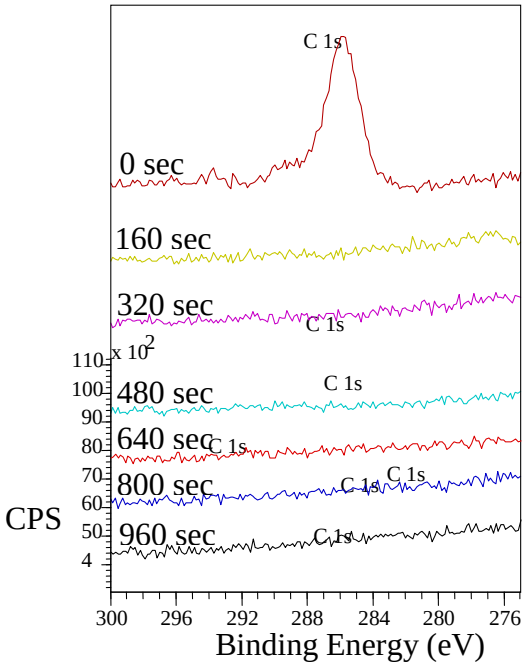

Figure 6.3b: Carbon 1s region from a sample using system 1, after annealing

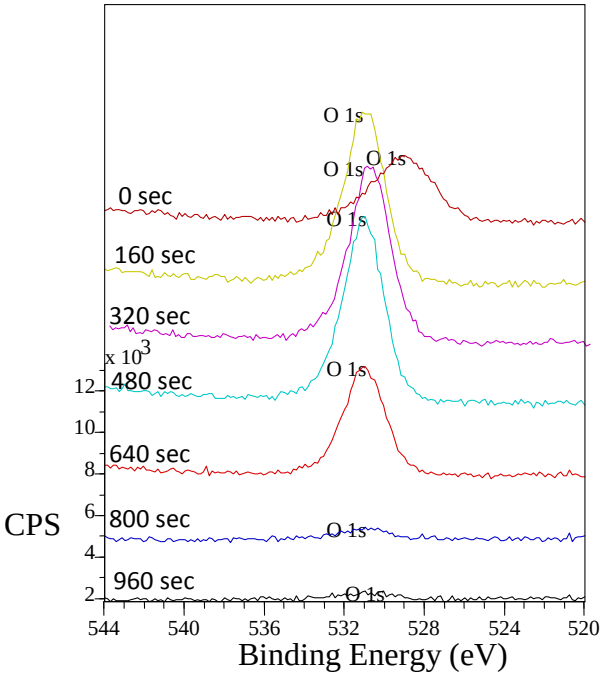

Figure 6.3c: O1s region from a sample using system 1

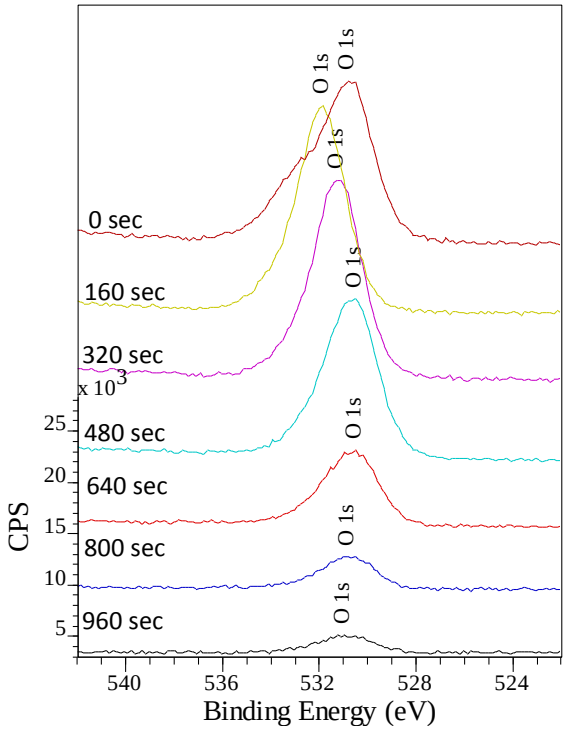

Figure 6.3d: O1s region from a sample using system 1, after annealing

In the O 1s spectra, fig. 6.3c and 6.3d, a broad oxygen peak is observed on the surface of the sample. It can be deconvoluted into a peak at low binding energy at 528 eV assigned to surface contamination and a peak at 532 eV corresponding to LZO. There is a shift in the oxygen peaks at different depths of the sample, corresponding to the various oxides present. With sputtering, the peak at 532 eV diminishes when La and Zr concentrations diminish. It shifts towards 531.5 eV, particularly in the annealed sample, indicating that oxidized Ni is present in the inner part of the sample. During annealing the physical property of the sample also changed from shiny texture (as-prepared LZO layer) to a hazy, and mildly peeled off layer (under YBCO conditions).

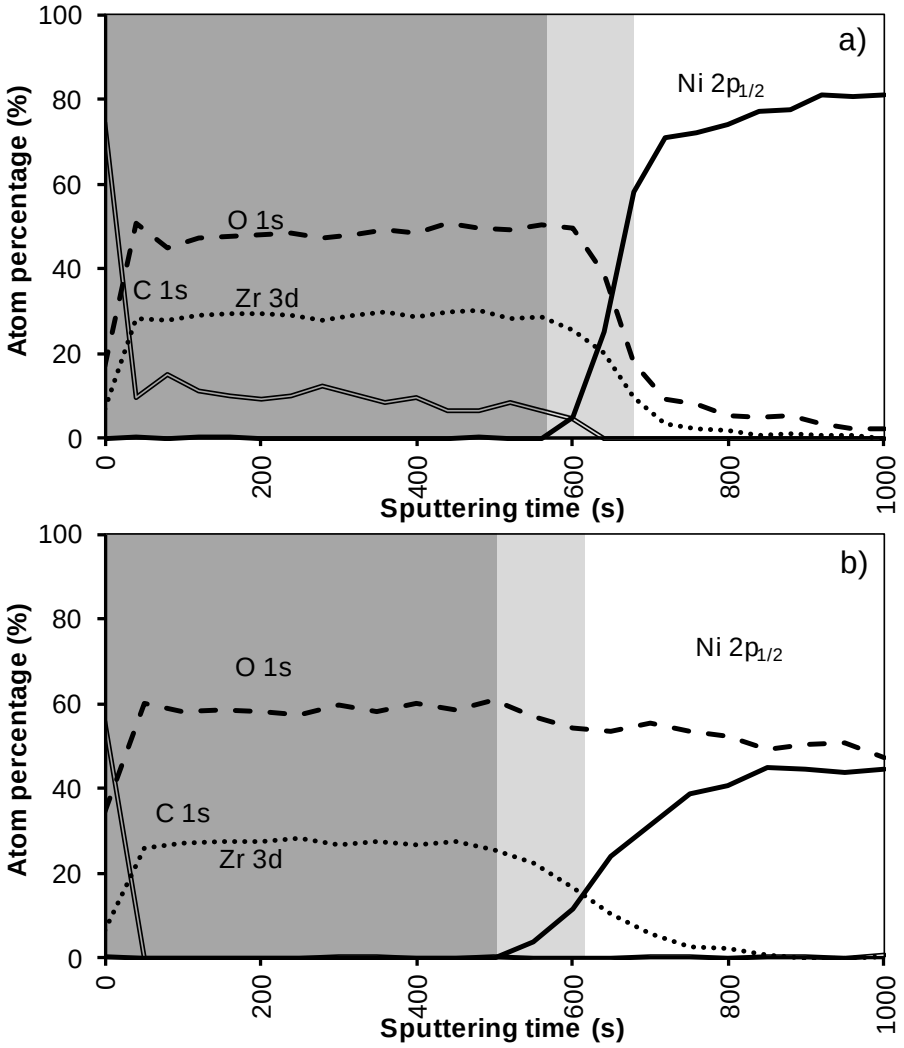

Figure 6.4(a-b): XPS depth profile using sol gel system 2 a) before and after b) simulated oxidation treatment

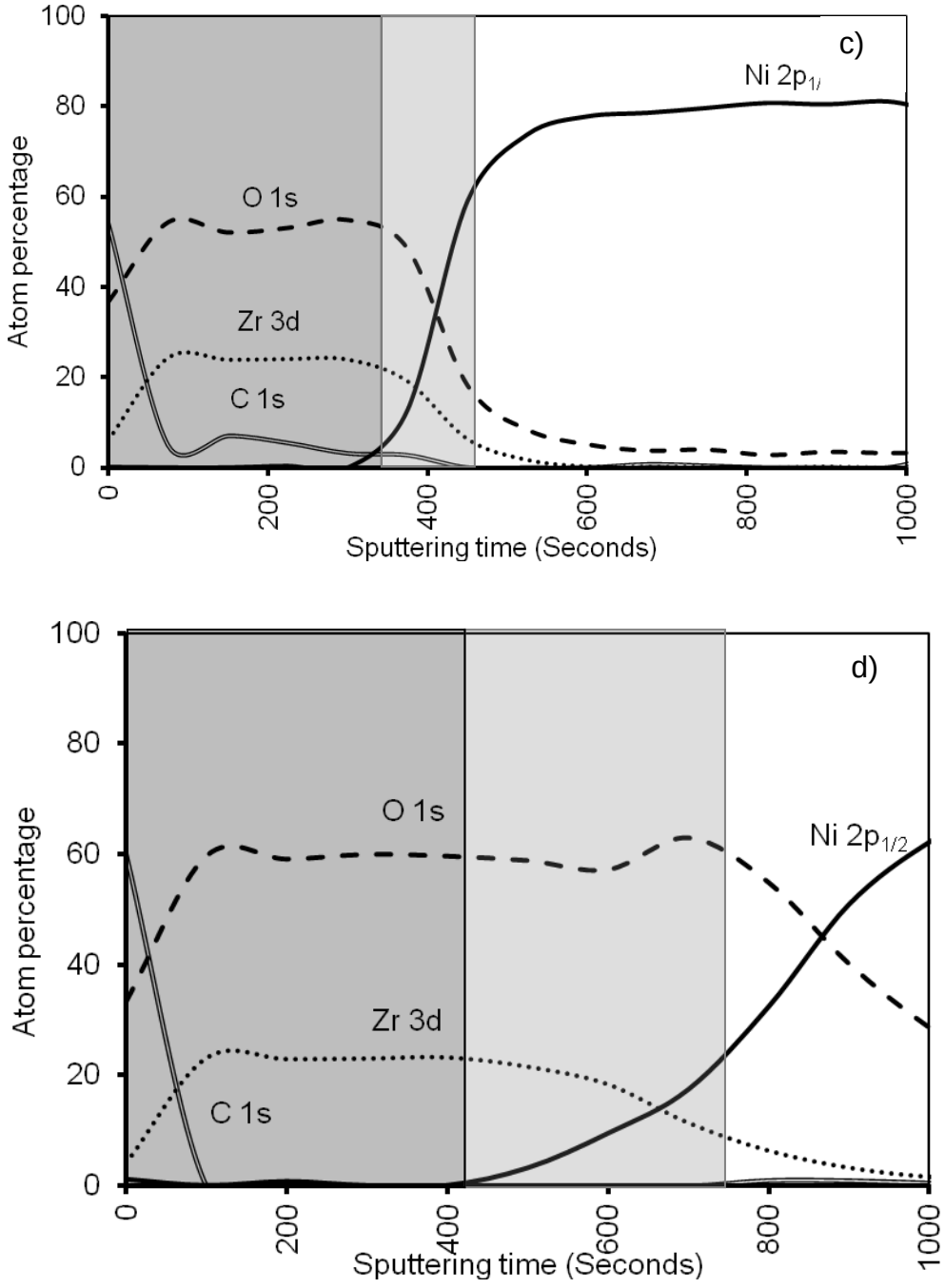

Figure 6.4 (c-d): XPS depth profile using sol-gel system 3 a) before and after b) simulated oxidation treatment.

Fig. 6.4a shows the XPS depth profile of the sample prepared with system 2 before annealing. The increased viscosity resulted in a thicker oxide film. As could be expected from ellipsometry and TEM measurements, the LZO film and thus the nickel free zone is now much thicker. The first nickel peak appears in the spectrum after 560 seconds of sputtering. Another 100 sputter seconds later the concentration of Zr drop towards half the maximal value. The thickness of the LZO layer is confirmed to be approximately 110 nm thick. The spectra are free of Nickel during the first 560 s.

After annealing this sample shown in Fig. 6.4b, again, the diffusion of Zr into Ni and vice versa vastly increased. The position at which the nickel concentration steeply increased, is reduced from 100 to 85 nm (560 to 500 s respectively). In the mean time the carbon content inside the layer disappeared. Presumably it was oxidized by the penetrating oxygen.

Similar results were obtained in samples prepared with solgel system 3, fig 6.4c-d. The observed nickel free region is estimated to be 51 and 20 nm respectively before and after annealing. The carbon observed in the sample is lower, allocated to the lower organic load of this system in fig 6.4c-d.

In order to increase the critical thickness of the layers and the final nickel free zone after annealing, polyvinyl pyrrolidone (PVP) was added to the sol. System 4 is similar to system 2 but the addition of PVP increased the viscosity of the sol to 5.7 mPa.s and the layer thickness after dipcoating is at least doubled. Ellipsometry shows a layer thickness of 280 nm while FIB-SEM (Fig. 6.5a) showed local thicknesses of 205 – 225 nm. Unfortunately, during the thermal process gases get trapped into the solution-gel system and the resulting layer exhibits a high porosity (Fig. 6.5b) compared with Fig.6.1a. Those pores were present throughout the entire layer.

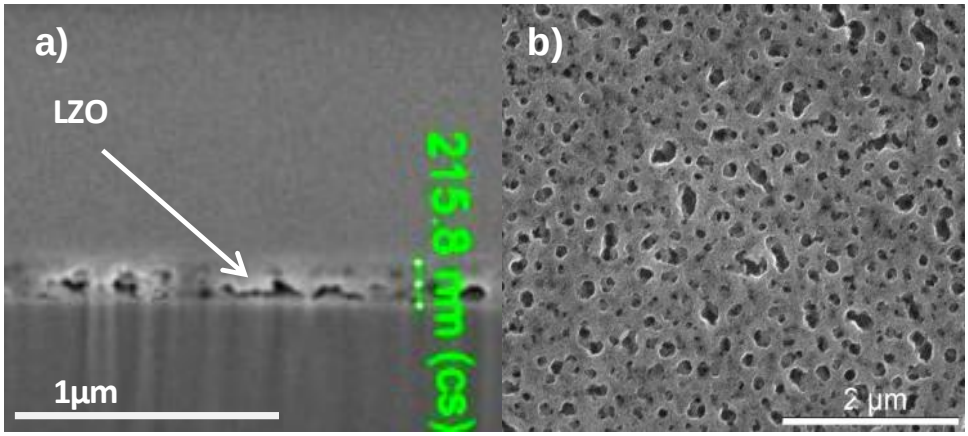

Figure 6.5 a) Cross- sectional FIB-SEM micrograph and a SEM micrograph of the top surface of a sample prepared by system 4 before simulated oxidation annealing.

In the XPS depth profiling (Fig. 6.6a and b) of samples prepared by system 4, the first nickel peaks are observed after 120 nm (720 s). During annealing the nickel containing zone shifts with at least 30 nm (180 s). The increased thickness of the Ni free zone is related to the thicker LZO layer but the poor morphology causes an important reduction of the buffer capacity by 30 % after annealing. A more dense but still thick enough LZO layer could lower the Ni penetration after annealing.

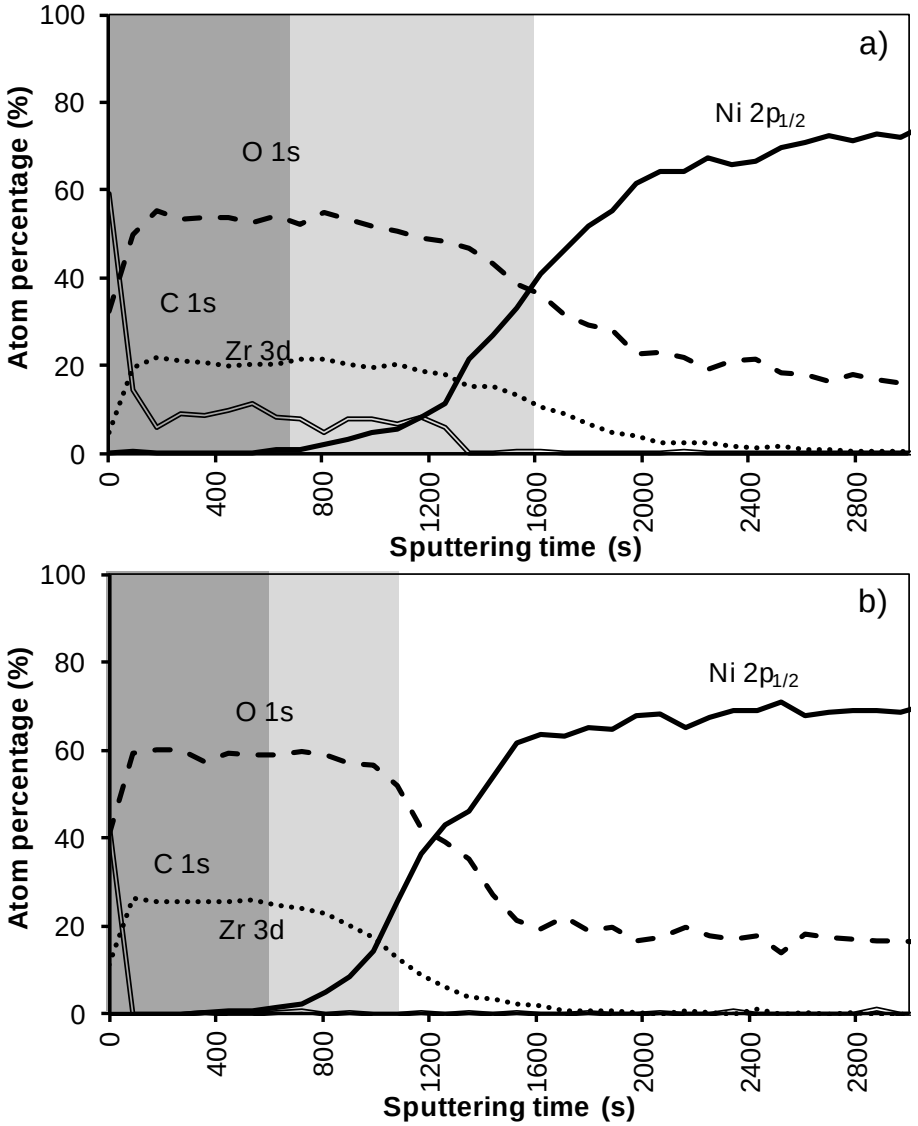

Figure 6.6 (a-b): XPS depth profile of a buffer layered sample using system 4 a) before and after b) simulated oxidation treatment.

A dense, crack free film, with an intermediate thickness could be synthesized by using PVP but replacing ethylene diamine and ethylene glycol by AMP. This results in a precursor solution (system 4) with an intermediate viscosity of and a resultant layer thickness between 125 and 150 nm. SEM and FIB-SEM analysis on this sample confirmed that gases now could escape from the gel and a dense, crack-free top surface of the film was created as can be seen in Fig. 6.7 (a-b).

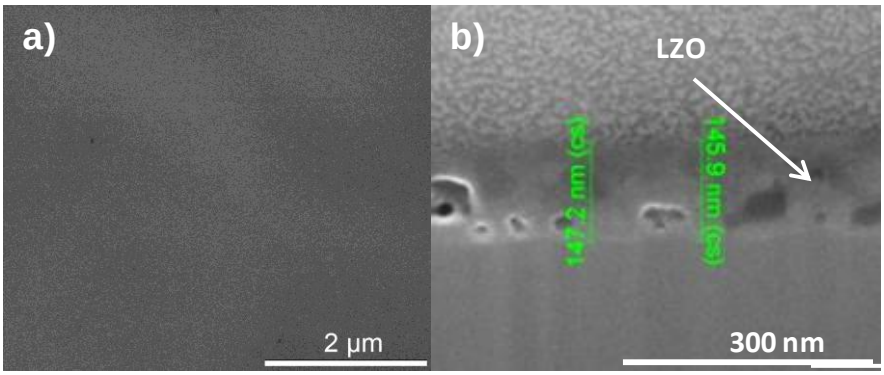

Figure 6.7: SEM micrograph of the a) top surface and b) cross section of a sample prepared by system 5 before simulated oxidation annealing.

The XPS depth profile of a film synthesized using this sol gel system 5 is shown in Fig. 6.8. Before annealing the nickel free zone is estimated to be 85 nm (500 sec) which is in the same order as system 2. As in all previous samples annealing results in an increase in oxygen content in the interior of the sample, pointing to the formation of NiO, removal of carbon and an increased interdiffusion of the adjacent layers. However, it is promising that with the increased layer thickness the nickel free zone of 85 nm could be maintained after annealing. Based on the above results, it can be summarized that the performance of the water based thin film (non-polymer and polymer included) against Ni penetration is strongly dependent on its thickness and morphology. But, layers from all these systems do not completely withstand the oxidizing condition under YBCO annealing completely as they are showing partial oxidation through the layers.

Additionally it has been shown that the film, prepared by system 5, is an appropriate buffer layer for the preparation of an YBCO coated conductor as a highly resembling film was used as a buffer layer for depositing an YBCO thin film by metal-organic decomposition (MOD) [9]. A buffer layer prepared by system 5 shows that CSD layers prepared by a well defined water-based chemistry can result in buffer layers preventing Ni diffusion and Ni oxidation.

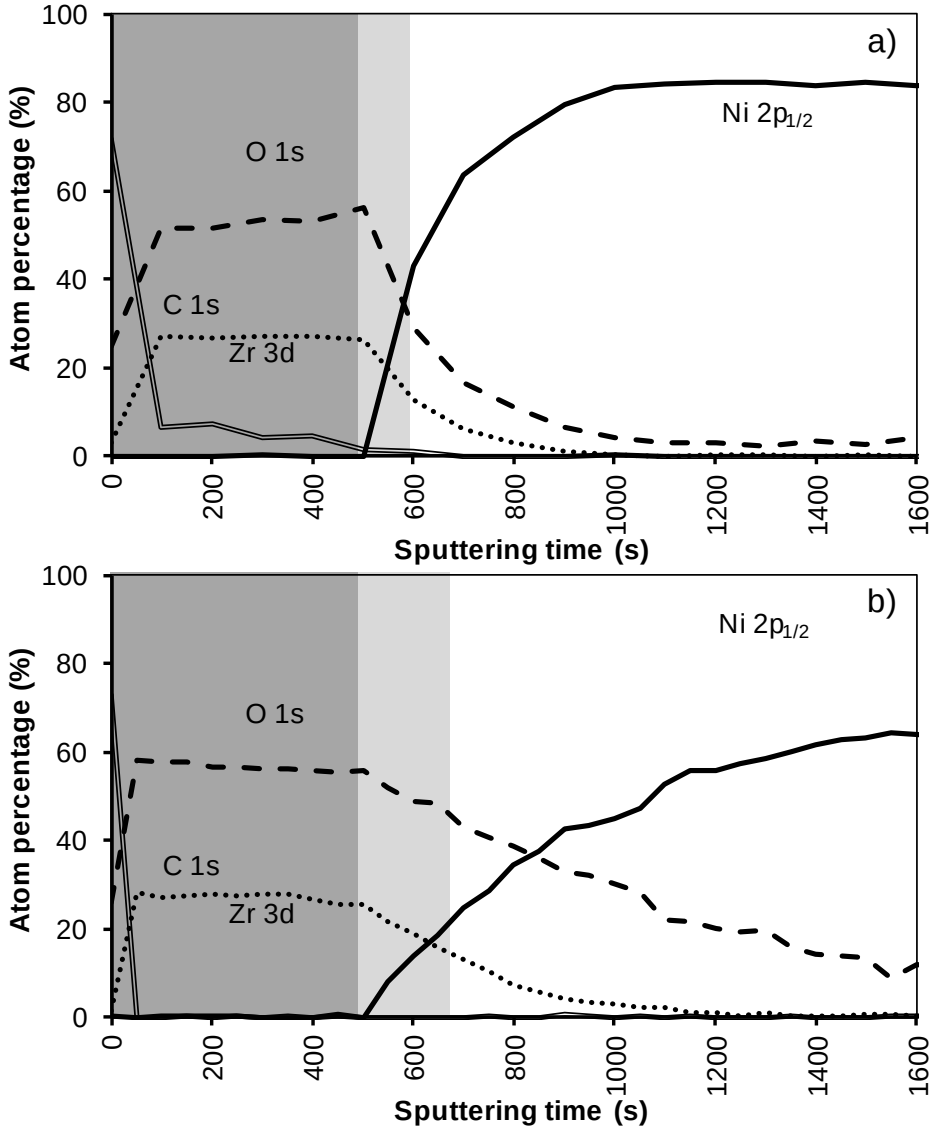

Figure 6.8 XPS depth profile of a buffer layered sample using system 5 a) before and b) after simulated oxidation treatment

Finally the capacity of our film to withstand nickel diffusion was compared to the commercially available LZO layers of Zenergy GmbH with a thickness of respectively 140 and 275 nm.

The 140 nm thick LZO layer showed to have a nickel free zone of 96 nm before and 72 nm after annealing, fig. 6.9a. Similar to the evolution we observed in our samples.

The overall evolution of the different atomic concentrations in the 140 nm thick commercial LZO layer resembles the concentrations when using system 5. But after annealing the oxygen penetrates much further into the Ni/W tape and the interdiffusion of La/Zr and Ni/W tape increased till more than 700 seconds of sputtering (fig. 6.9b).

The analysis of the 275 nm thick commercial layer, fig. 6.10a, shows that in this case the nickel free region could be maintained at 220 nm even after annealing (1400 sec). A closer look at the evolution of the oxygen concentration shows us that the time needed to drop from the maximum value (60 at%) to half that value (30 at%) is about 450 seconds and did not increase during annealing, fig. 6.10b In contrast to what is observed in all previous samples in which this decline at least tripled in time during the annealing step. The sputtertime at which Zr and La concentration decrease till half their maximum in the commercial layers, respectively 750 and 1800 seconds again confirm an average sputterrate of 0.17 nm/sec for LZO.

The percentage of oxygen through the layer decreased constantly with increasing Ni both in as-prepared and sample treated under YBCO condition. This indicates that the sample is free from oxidation. Based on the above results, it can be summarized that the performance of the water based (non-polymer and polymer included) and non-water based LZO layers (on comparable thickness range) show comparable performance against Ni penetration. But, layers from all these systems thinner than 270 nm were not efficient to withstand the oxidizing condition under YBCO annealing totally showing partial oxidation through the layers.

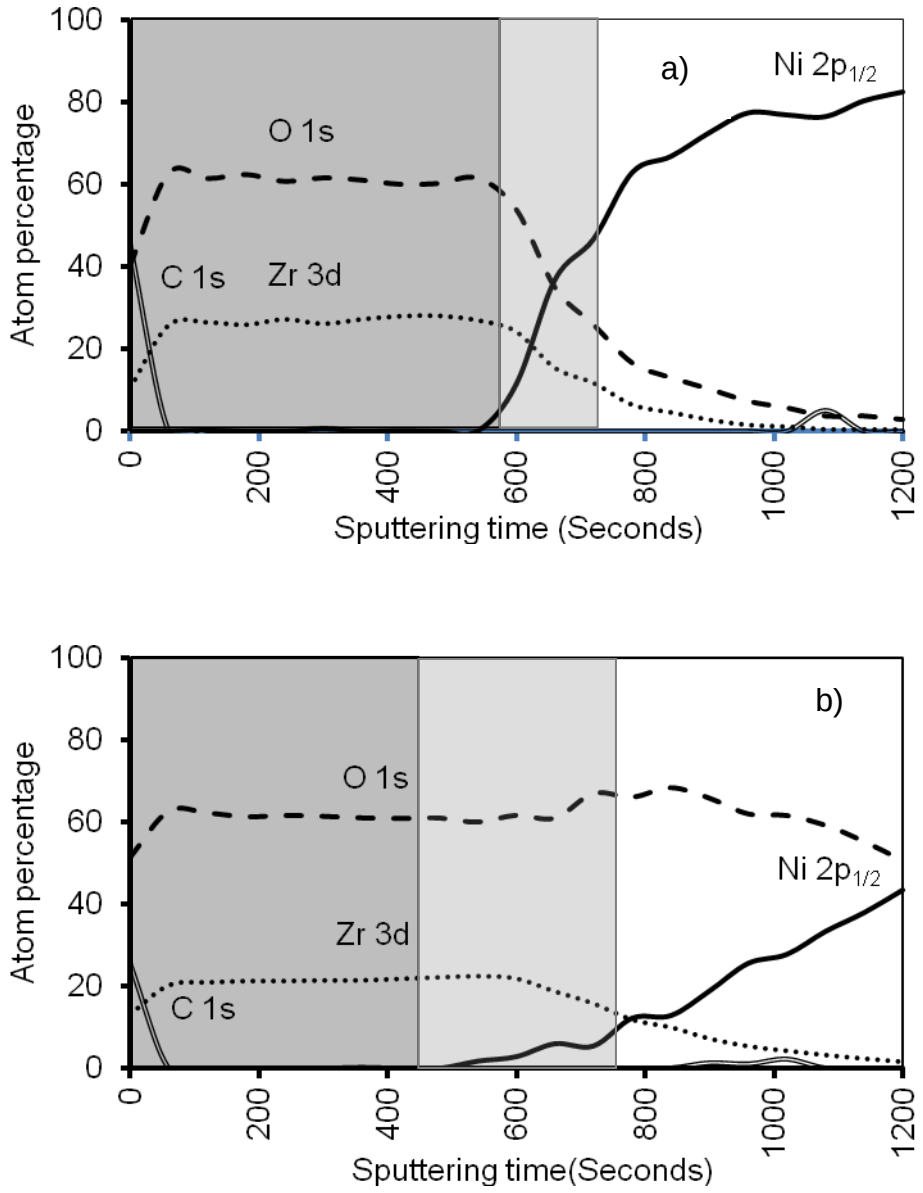

Figure 6.9(a-b): XPS depth profile of 140 nm thick commercial LZO, a) before and after b) simulated oxidation treatment.

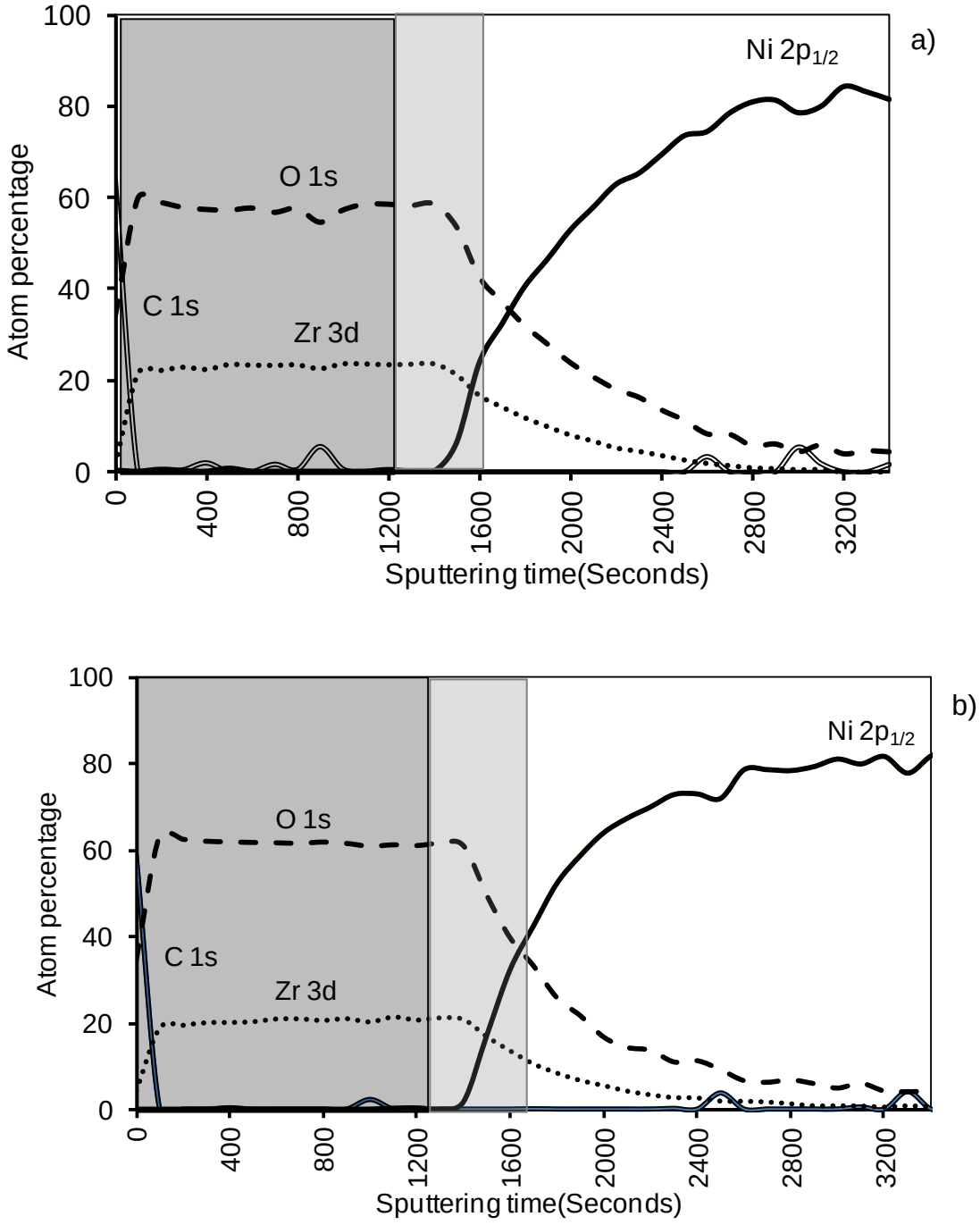

Figure 6.10(a-b): XPS depth profile of 275 nm thick commercial LZO a) before and after b) simulated oxidation treatment

Table 2 summarizes all the seven different LZO layers as follows;

LZO layers	*Thickness of buffer layer according to elllipsometry*	*Zr concentration drops to half of maximum value*	*Average sputter rate*	*Strong increase in Ni peak*	*Ni reaches start of plateau*
		seconds of sputtering		*seconds of sputtering*	*seconds of sputtering*
System 1	*40 nm*	*250*	*1.7 Å/s*	*200*	*400*
System 1 YBCO annealed		*300*	*1.7Å/s*	*180*	*550*
System 2	*~110 nm*	*660*	*1.7Å/s*	*560*	*720*
System2 YBCO annealed		*630*	*1.7 Å/s*	*500*	*1200*
System 3	*85-90 nm*	*420-440*	*1.7 Å/s*	*700*	*500*
System 3 YBCO annealed		*700-720*	*1.7 Å/s*	*900*	*920*
System 4	*280 nm*	*1600*	*1.7 Å/s*	*810*	*2000*
System 4 YBCO annealed		*1100*	*1.7 Å/s*	*540*	*1600*
System 5	*125-150 nm*	*580*	*1.7 Å/s*	*500*	*900*

System 5 YBCO annealed		*670*	*1.7 Å/s*	*500*	*1400*
Commercial layer 1	*140-145 nm*	*650*	*1.7 Å/s*	*900*	*900-950*
Commercial layer 1 YBCO annealed		*850*	*1.7 Å/s*	*1100*	
Commercial layer 2	*275-280 nm*	*1600*	*1.7 Å/s*	*2400*	*2500*
Commercial layer 2 YBCO annealed		*1600*	*1.7 Å/s*	*2400*	*2500*

6.4 Conclusions

It was shown that XPS depth profiling is a versatile tool to analyse thin films towards their ability to act as a bufferlayer. Several LZO thin films were synthesized and annealed. Depth profiles allowed to compare the degree of oxidation in the inner part of the samples, degree of diffusion and thus width of nickel-free zones on top of the samples. It was thus shown that the Ni diffusion is influenced by the microstructure of the LZO layers. Comparing these results with ellipsometry and TEM cross sections showed an LZO sputter rate of 0.17 nm/sec both in synthesized and commercial layers.

An aqueous sol gel synthesis for LZO layers was produced which results in bufferlayers that have a capacity of protecting subsequent layers from Ni diffusion that is

comparable to a 140 nm thick commercial LZO layer, with a nickel free region of 65 nm, sufficient for deposition of an YBCO film by pulsed layer deposition.

A 275 nm thick commercial LZO layer exhibits a nickel free region which is far higher compared to what was reached in our samples and could resist additional oxidation of nickel during annealing step.

References

[1] K. Knoth , R. Hühne , S. Oswald , L. Schultz , B. Holzapfel, Acta Materialia 55 (2007) 517–29.

[2] T. Caroff, L. Porcar, P. Chaudouët, A. Abrutis, C. Jiménez, P.Odier and F. Weiss, IEEE Transactions on Applied Superconductivity 19 (2009) 3184-3187.

[3] V. Cloet, J. Feys, R. Hühne, S. Hoste, I. Van Driessche, Journal of Solid State Chemistry 182 (2009) 37–42.

[4] Steffen Oswald, Kerstin Knoth and Bernhard Holzapfel, Microchim Acta 156 (2007) 121–124.

[5] V. Cloet, T. Thersleff, O. Stadel, S. Hoste, B. Holzapfel, I. Van Driessche, Acta Materialia 58 (2010) 1489–94.

[6] H. Kozuka, Journal of the ceramic society of Japan111 (2003) 624-632.

[7] Pieter Vermeir, Iwein Cardinael, Michael Bäcker, Joseph Schaubroeck, Etienne Schacht, Serge Hoste and Isabel Van Driessche, Supercond. Sci. Technol. 22 (2009) 075009-075015

[8] L. Molina, K. Knoth, S. Engel, B. Holzapfel, O. Eibl, Supercond. Sci. Technol. 19 (2006) 1200-1208.

[9] S. Petit, M. Mikolajczyk, J.L. Soubeyroux, T. Waeckerle, R. Batonnet, S. Pairis, P. Odier, IEEE Trans. Appl. Supercond. 21 (2011) 2977-2980.

Chapter-7

Lattice-tuned $La_xCe_{1-x}O_\delta$, doped LZO and modified LZO epitaxial layers

This chapter focuses on the deposition of lanthanum-cerium oxide (LCO) films were deposition on Ni-5%W substrates by CSD as well from from water-based precursors. These LCO films were prepared in a range starting from CeO_2 to $La_2Ce_2O_7$ containing different ratios of La and Ce ions. The layers' composiiton was optimized towards the formation of LCO buffer layers, lattice-matched with the superconducting $YBa_2Cu_3O_y$ layer. As a continuation, cerium doped lanthanum zirconate (LCZO) films and non-stoichiometric lanthanum zirconate buffer layers on metallic Ni-5%W substrates using chemical solution deposition (CSD), starting from aqueous precursor solutions is presented. $La_2Zr_2O_7$ films doped with varying percentages of Ce at constant La concentration ($La_{0.5}Ce_xZr_{1-x}O_y$) were prepared as well as non-stoichiometric $La_{0.5+x}Zr_{0.5-x}O_y$ buffer layers with different percentages of La and Zr ratios. The variation in the composition of these thin films allows to create novel buffer layers with tailored lattice parameters in lines with LCO and other epitaxial layers This was envisaged to be useful for the development of coated conductors with possibly single buffer layers that can replace the $CeO_2/La_2Zr_2O_7$/Ni-5%W.

7.1 Route towards novel buffer layers

To suppress the production cost for long length coated conductors, one is looking to replace the current three or two buffer layers by one single layer [1-6]. Therefore, we need a material that can grow as a thick enough layer on Ni-W tape without losing its biaxial texture on the top surface and furthermore with a small lattice mismatch compared to YBCO to ensure high superconducting properties. Possible lattice matched buffer layers that have been reported for this purpose include $YBiO_3$, Gd^{3+} doped CeO_2, La^{3+} doped CeO_2 or Eu^{3+} doped Yb_2O_3 [7-8].

In the past 10 years, cerium oxide and more specifically La^{3+} doped CeO_2 (LCO) have been reported as materials with a very high thermal and chemical stability and a low thermal conductivity. LCO does not show any phase transitions between room temperature and up to 1400 °C. Therefore, it is also being investigated as one of the most promising new materials for thermal barrier coatings [9-11]. Furthermore, the Ce-cations in the CeO_2 fluorite type cubic lattice can easily change their oxidation state from 4+ and 3+ and vice versa, a process being coupled with the presence of oxygen vacancies in the ceria lattice. By introducing rare earth dopants in the lattice, this tendency of CeO_2 to store/conduct/release oxygen can be further improved since for each two La^{3+} ions being introduced in the ceria lattice, one oxygen vacancy needs to be formed to ensure charge neutrality of the compound. Recent theoretical work on this system by Vanpoucke *et al.* shows that oxygen vacancies in LCO clearly prefer a Ce environment over a La one, resulting in a reduction of the Ce ions neighbouring the oxygen vacancy [12]. Related to this, it has been reported that the creation of vacancies and defects in the structure of CeO_2, changing the oxidation state of the Ce ion, influences the stability, thereby reducing the reactivity of the layer [13]. Hence, $La_{1-x}Ce_xO_{2-x/2}$ is a promising oxide material for use in solid oxide fuel cells as electrolyte layer or in catalysts [9-14] and could be envisaged as an alternative buffer layer for YBCO coated conductors, related to the appropriate crystal structure and possible improved stability compared to CeO_2. La^{3+} is reported to be incorporated in the CeO_2 crystal lattice up to doping percentages of 55%. Since La^{3+} has a larger ionic radius than Ce^{4+} (1.16 vs 0.97 Å), it increases the cubic lattice parameter of ceria upon doping (from ~5.42 to ~5.6 Å) [15-16]. In this work, the lattice tuning combined with the excellent material properties of LCO has been investigated for its use as a buffer layer in coated conductor architectures.

By varying the composition of the LCO material from pure CeO_2 to $La_2Ce_2O_7$, the lattice mismatch with the Ni-5%W tape is being increased from 8 to 11%. At the same time, with increasing La content, an almost perfect lattice match with the $YBCO_{7-x}$ *a*-axis, $YBCO_{6+x}$ or the $YBCO_{7-x}$ *b*-axis can be obtained. The influence of the elemental composition of the material on its lattice parameters and the quality of the epitaxial growth of LCO layers directly on buffered tape has been studied. The research focused on the investigation of solid solution compositions with optimal lattice match towards YBCO, the growth of single buffer layers on NiW substrates exhibiting dense, crack-free, uniform and textured morphology and structure and the study of the buffer capacity of these coatings.

7.2 Experimental Methods for LCO layers

7.2.1 Precursor solution synthesis

Aqueous LCO precursor solutions (0.4M) was prepared by dissolving cerium acetate ($Ce(CH_3COO)_3.xH_2O$, Sigma-Aldrich, 99.9%) in a water (MilliQ) - acetic acid (Rotipuran, 100%) (HOAc) mixture (Ce^{3+}:HOAc:H_2O = 1:5:40) at 80°C. A stoichiometric amount of lanthanum acetate ($La(CH_3COO)_3.xH_2O$, Sigma-Aldrich, 99.9%) was added to the cerium precursor solution at 80°C. To ensure stoichiometry, the water content of all precursor salts was determined by TGA analysis. To dissolve the metal acetates completely, additional H_2O and HOAc are added (Ce^{3+}+ La^{3+}: HOAc : H_2O = 1:5:80). Ethylene-diamine-tetra-acetic acid (EDTA, Sigma - Aldrich, 99.4%-100.6%) was used as a complexant [17, 18]. An EDTA solution was prepared by dissolving EDTA in a water and ethylene-diamine mixture (EDA, Fluka, 100%) (EDTA:H_2O:EDA = 1:60:4) at room temperature. The molar ratio of EDTA:(Ce^{3+}+ La^{3+}) was fixed at 0.5:1. The metal solution (Ce^{3+}+ La^{3+}) was slowly added to the EDTA solution at room temperature and stirred for 10 minutes. The pH of the mixed solution was adjusted from 3 to 6 by addition of ammonia. After heating to 60°C, ethylene glycol (EG, Sigma- Aldrich, > 99%) was added (molar ratio EDTA:EG = 1:6). Finally, excess solvent was evaporated while stirring at 60 °C, until the desired concentration of 0.4 mol/L was obtained. This precursor solution has a final pH of 6 and a viscosity of 5.60 mPas. This preparation is in accordance with earlier preparation methods (sec. 5.2) using water as the main solvent for environmental friendliness and cost-efficiency.

7.2.2 Preparation of powders

A series of powders with varying composition ($La_xCe_{1-x}O_\delta$ with $0 \leq x \leq 1$) were prepared from the precursor solutions discussed above. The powders were obtained by pouring 15 mL of the precursor solution into an Al_2O_3 crucible that was placed inside a muffle furnace. The conversion into solid matter was carried out under air by reaching 1000 °C from room temperature in 4 hours and let to stabilize for 2 hours. They were then cooled down to room temperature within 3 hours time.

7.3 Solution deposition and heat treatment for LCO

The Ni-5%W tapes of 1 cm width and 80 µm thickness (manufactured by EVICO GmbH) were supplied by Zenergy Power GmbH. The tapes were cut into strips of 2.5 cm length for dip-coating and cleaned as described in chapter 3. These substrates were dip-coated at a withdrawal speed ranging between 20-60 mm/min in a clean room (class 10,000) to prevent contamination with dust particles. The as-deposited layers were transformed into a gel by placing them in a drying furnace at 60°C for one hour. The amorphous gel layers were transformed into crystalline layers by applying a suitable heat treatment. The as-deposited layers were first heated from room temperature to 450°C (ramp rate of 1°C/min) and let to dwell for 1 hour. Secondly, a 3°C/min heating rate was applied from 450°C until 900°C (dwell time = 1h). Finally, the films were heated to 1050°C at a 10°C/min ramp with a dwell time of one hour. After the heat treatment, the furnace was switched off and the samples were left to cool inside the furnace. The entire heating and cooling process was carried out in an Ar-5%H_2 atmosphere (gas flow range: 0.1L/min).

7.4 LCO powders and cell parameters

A series of different lanthanum cerate precursor solutions, with a composition ranging from pure CeO_2 to $La_2Ce_2O_7$ were prepared according to the synthesis methods discussed above (sec.7.2.1). For clarity, the La^{3+} doping of CeO_2 in this work is represented by the following formula: $La_xCe_{1-x}O_{2-x/2}$ [19]. Typically, a 50% La^{3+} doped CeO_2 is written as $La_{0.5}Ce_{0.5}O_{1.75}$ (or $La_2Ce_2O_7$ according to the number of atoms present in the unit cell of the crystallographic lattice). Since, for LCO based compounds, it is well-known that the number of oxygen vacancies

can fluctuate easily, we use the label δ to denote the oxygen off-stoichiometry throughout this work. To study the substitution behavior of La^{3+} for Ce^{4+}, these different precursor solutions were converted into solid matter by heating to 1000°C under air and studied by X-ray diffraction (fig. 7.1). In literature, cerium oxide doped with La^{3+} is presumed to exhibit the typical CeO_2 fluorite lattice for low dopant concentrations and even up to concentrations of 40 at.%. For doping concentrations reaching 50% either a distorted fluorite or a pyrochlore structure is assumed [19-21]. In their recent theoretical study on $La_2Ce_2O_7$, Vanpoucke *et al.* show that the pyrochlore structure is the actual crystallographic ground state for $La_2Ce_2O_7$ [12]. It is found that, La^{3+} addition in CeO_2 is more energetically favoured when assuming such a structure. More specifically, it is shown that the introduced oxygen vacancies prefer a Ce tetrahedral surrounding. Vanpoucke *et al.* have also calculated for a fluorite lattice with randomly distributed La and Ce cations that the number of charge compensating oxygen vacancies will outnumber the number of Ce tetrahedra for a La concentration of about 43 at. %, indicating the driving force of the pyrochlore transformation [12, 20]. One of the most relevant theoretical findings of this work is that, based on simulated XRD spectra, the spectrum of $La_2Ce_2O_7$ with a pyrochlore structure is nearly indistinguishable from a fluorite spectrum. They also showed that the typical pyrochlore (3 3 1), (4 2 2) and, (5 1 1) peaks have extremely low intensities, making them unobservable in most of the experiments. In this case, all experimental XRD spectra obtained from powders are indicative of the typical fluorite lattice for the full doping range, and no peaks related to the formation of secondary phases such as La_2O_3 can be found. A clear shift of the reflections towards lower 2theta values as a function of La^{3+} content was found.

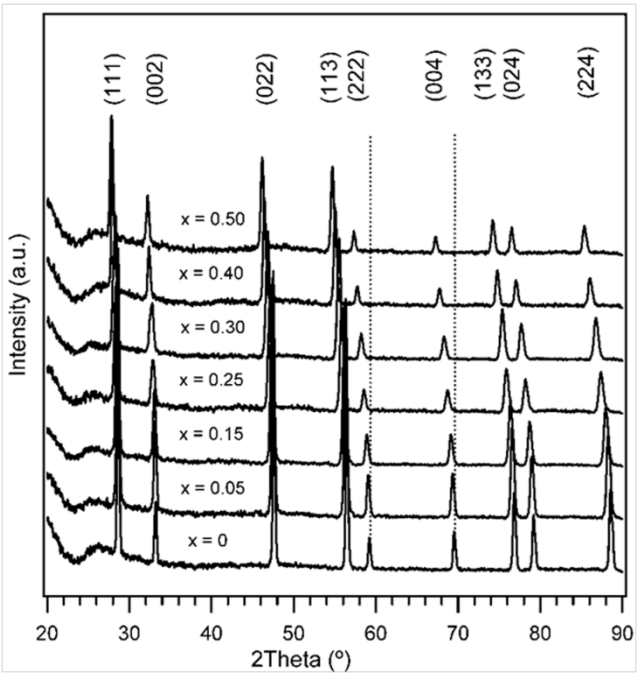

Figure 7.1: XRD reflection patterns obtained for a series of $La_xCe_{1-x}O_\delta$ powders (from bottom to top : x = 0, 0.05, 0.15, 0.25, 0.30, 0.40 0.50).

Using the (CeO_2, fluorite) reflections indexed in figure 7.1, the cell parameters for the different $La_xCe_{1-x}O_\delta$ compositions were calculated with *unit cell 2006* [22].

7.5 Epitaxial LCO films on Ni-5%W tape and their characterization

Based on the results obtained for LCO powders, where it is obvious that the LCO lattice parameter can be linearly varied by doping with different amounts of La^{3+}, we continued our research on thin films deposited on NiW tape. Again, a series of samples with varying La^{3+} content, ranging from pure CeO_2 to $La_2Ce_2O_7$, were prepared. The withdrawal speed during dip coating was set at 20 mm/min. In this way, layers with a thickness of ~ 60 to 70 nm, as determined from ellipsometry, can be obtained. Figure 7.2 shows the XRD spectra collected for these thin films on NiW tapes.

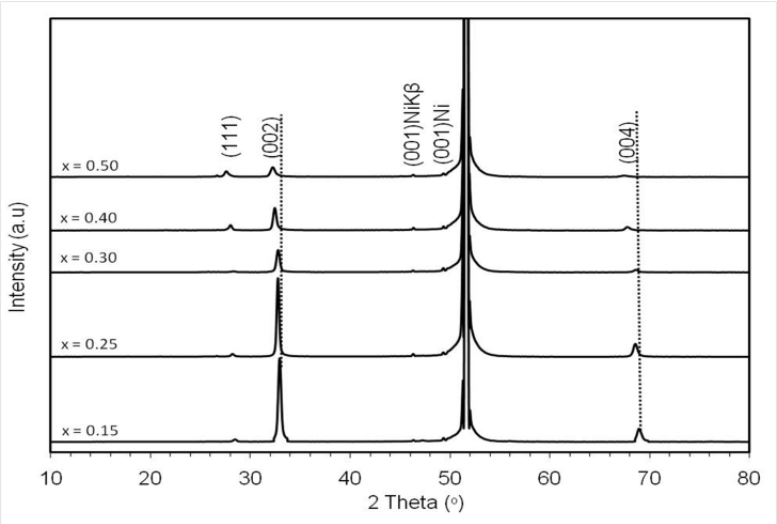

Figure 7.2: XRD reflection patterns obtained for a series of $La_xCe_{1-x}O_\delta$ thin films deposited at a dipcoating speed of 20mm/min on Ni-5%W tape (from bottom to top : x = 0.15, 0.25, 0.30, 0.40 0.50).

In line with the results for powder diffraction, no trace of any secondary phase can be found, and all layers exhibit the expected fluorite structure. Also for the layers, the reflections shift to lower 2 theta values as a function of La^{3+} content, related to its larger ionic radius compared to Ce^{4+}. The lattice parameters extracted from these XRD reflections are plotted as a function of La^{3+} content in figure 7.3.

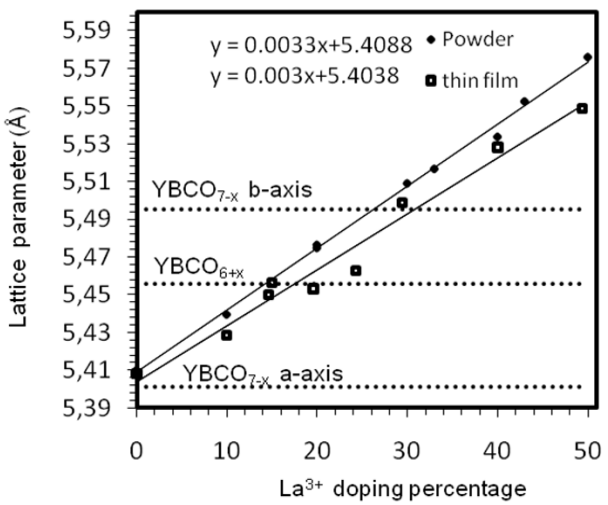

Figure 7.3: $La_xCe_{1-x}O_\delta$ fluorite lattice parameter as a function of La^{3+} doping percentage as calculated from XRD reflections for both LCO powders and thin films deposited on NiW tape. As a reference, the a and b lattice parameters for $YBCO_{7-x}$ and the a-lattice parameter for $YBCO_{6+x}$ are added to the graph. Powders : slope = 0.0033, intercept = 5.409 and for the films : slope = 0.0030, intercept = 5.404.

In figure 7.3, these lattice parameters are plotted as a function of La^{3+} doping percentage. Due to the large ionic radius of La^{3+} (1.16 Å) in comparison with Ce^{4+} (0.97 Å), we observe an increase of the lattice parameter. In line with previous findings for $La_{1-x}Ce_xO_\delta$, a linear increase of the lattice parameter up to doping percentages of 50% (solubility limit for La^{3+} in CeO_2 is 55%) is observed, showing that using this aqueous sol-gel process, stoichiometric solid-solutions can be formed. A least-squares linear fit through the points gives a slope of 0.0033 which is in line with others [5, 23]. The larger scattering on the data for the thin films compared to the powders is related to the much smaller number of reflections which can be used to perform the lattice parameters calculations because of the disappearance of a large number of reflections due to the oriented (0 0 1) growth on Ni-5%W substrates. Due to compressive stain on the a-b plane there should be increase in lattice constant along the c-axis. But in this work only just the (00l) planes are not measured and taken into account, for the powder samples, the nine indexed planes [(1 1 1), (0 0 2), (0 2 2), (1 1 3), (2 2 2), (0 0 4), (1 3 3), (0 0 4), (1 3 3), (0 2 4), (2 2 4)] as shown in figure and the lattice parameter was calculated corresponding to each plane using a program named "Cell parameter". The presented lattice parameter corresponds to their average value. However, for the thin films only three planes were indexed, (1 1 1), (0 0 2) and (0 0 4) due to the epitaxial growth. Moreover, the lattice parameters for thin films were determined using Bragg's law corresponding to each plane and the average value is presented. (Cell parameter program needs at least values from nine crystalline planes). Added to this, the powder samples were synthesized in air and thin films were grown in an Ar-5%H_2 reducing atmosphere. Nevertheless, also for the thin films, we find a linear relation between the La^{3+} content and the lattice parameter. Yet, all data points for the thin films lie below those for the powders. This difference in lattice parameter between powder and thin films might have many origins. Firstly, the lattice parameter of the NiW substrate is 3.54 Å. Since LCO grows 45° rotated versus the NiW cubic lattice for lattice matching, this means that the substrate (sqrt($2a^2$) = 5.01 Å) has a negative mismatch compared to the LCO layers and thus compressive strain will occur in the thin films. On the other hand, the LCO powders were synthesized under air while thin films on NiW tape have to be heat treated under reducing conditions (Ar-5%H_2). It is well known that LCO is very sensitive to the formation of oxygen vacancies and these can influence the lattice parameters. Vanpoucke et al have published, based on DFT simulations, that in the case where

no oxygen vacancies exist and thus similar to when processing under air, the lattice parameter changes 2.75% when moving from CeO_2 to $La_2Ce_2O_8$. From our experimental values for powders we find a value of 2.95 %. In the case of LCO samples containing oxygen vacancies, the theoretical lattice expansion by La^{3+} doping is expected to be smaller, somewhere between 2.7 and 1.7%, depending on the lattice site being occupied by the vacancies. These numbers are in line with a number of experimental reports [19-21, 23-25]. Here, an experimental expansion of the lattice parameter of ~2.4% shows good agreement with the theoretical expectations.

Figure 7.4 represents the phi-scans carried-out to measure the in-plane misalignment of the (111) plane of the Ni substrate (at $2\theta = 44.50^{\circ}$ and $\phi = 54.7^{\circ}$) and that of the LCO films respectively. The FWHM of the reflections for these layers were found to be 6.21°, 6.49°, 6.95°, 7.02° and 7.16° respectively for $La_xCe_{1-x}O_\delta$ with x = 0.15, 0.25, 0.3, 0.4 and 0.5 while for the Ni-5%W tape a FWHM value of 6.10° was found. These results prove that the biaxial texture of the Ni-5%W tape was successfully transferred to the LCO layers,. The FWHM values calculated from the ϕ-scans are comparable to those that were previously reported for water-based LZO thin films (6.65°). To ensure the quality of YBCO growth on top of the LCO layers, it is necessary to analyze the surface texturation. Therefore, RHEED analysis was performed for a $La_{0.15}Ce_{0.85}O_\delta$ and a $La_{0.50}Ce_{0.50}O_\delta$ film on NiW tape. The first composition was selected for further research because of its good epitaxial growth on NiW tape and its small lattice mismatch with $YBa_2Cu_3O_{6+x}$ and $YBa_2Cu_3O_{7-x}$.

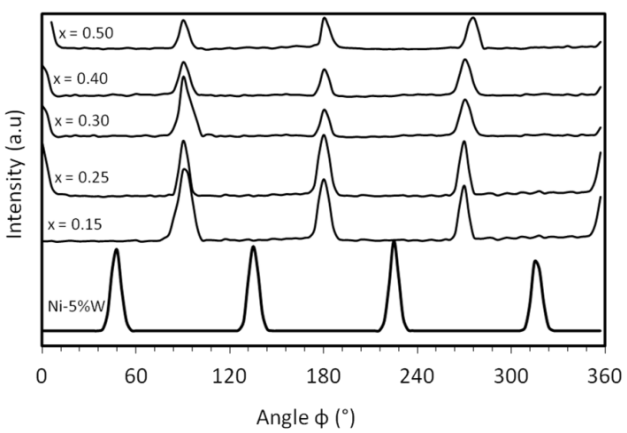

Figure 7.4: ϕ-scan measurements collected for approx. 60 nm thick $La_xCe_{1-x}O_\delta$ (x = 0.15, 0.25, 0.30, 0.40 and 0.50) films and a reference Ni-5%W tape.

From figure 2 it is clear that the LCO films can grow epitaxially on the Ni-5%W tape. Yet, clear differences in the quality of the epitaxial growth can be distinguished based on the La^{3+}/Ce^{4+} content in the different samples. The (002) reflections found for thin films of $La_{0.15}Ce_{0.85}O_{\delta}$ and $La_{0.25}Ce_{0.75}O_{\delta}$ are clearly the most intense. This can be easily understood based on lattice matching. Since the lattice parameter for Ni-5%W tape is even smaller than that of pure CeO_2, increased La^{3+} doping will cause an increased lattice mismatch between substrate and layer and thus disturb epitaxial growth at higher doping concentrations (see table 7.1)

Table 7.1 Lattice parameters for a series of $La_xCe_{1-x}O_{\delta}$ thin films on Ni-5%W tape and the related lattice mismatch values calculated for the Ni-5%W substrate, $YBCO_{6+x}$ and the a and b-axis of $YBCO_{7-x}$.

'La' doped cerium oxide systems	Lattice parameter 'a' (Å)	% Lattice mismatch with Ni-5%W substrate (3.54 Å)	% Lattice mismatch with **$Y_1Ba_2Cu_3O_{6+x}$** (3.86 Å)	% Lattice mismatch with the **a-axis of $Y_1Ba_2Cu_3O_{7-x}$** (3.83Å)	% Lattice mismatch with the **b-axis of $Y_1Ba_2Cu_3O_{7-x}$** (3.89 Å)
CeO_2	5.41	8.05	0.83	0.50	1.63
$La_{0.15}Ce_{0.85}O_{\delta}$	5.45	8.62	0.16	-0.560	1.14
$La_{0.25}Ce_{0.75}O_{\delta}$	5.46	9.13	-0.13	-0.989	0.66
$La_{0.3}Ce_{0.7}O_{\delta}$	5.49	9.85	-0.91	-1.644	0.10
$La_{0.4}Ce_{0.6}O_{\delta}$	5.52	10.18	-1.10	-2.06	0.37
$La_{0.5}Ce_{0.5}O_{\delta}$	5.54	10.85	-1.70	-2.72	0.98
$La_2Zr_2O_7$	10.79	7.60	1.11	0.52	1.83

As can be seen from figure 7.5, the top surfaces of the 60 to 70 nm thick films of both $La_{0.15}Ce_{0.85}O_{\delta}$ (figure 7.5a) and $La_{0.50}Ce_{0.50}O_{\delta}$ (figure 7.5b) are characterized by bright and discrete spots and some faint rings. This indicates that, grains at the surface of these layers are oriented along the (002) plane, although some parts of the layers are randomly oriented. There is

no clear difference in surface crystallinity between the two samples with variable La^{3+} content.

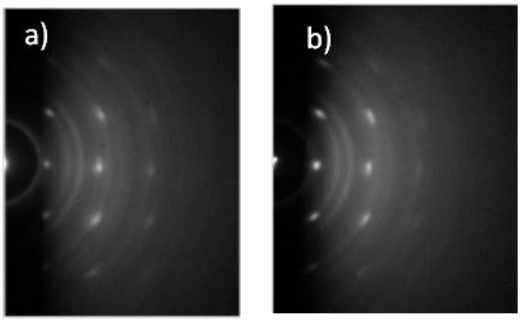

Figure 7.5: RHEED diffraction patterns collected along the <001> direction for a) a $La_{0.15}Ce_{0.85}O_{\delta}$ film of 60 nm thickness and b) a $La_{0.5}Ce_{0.5}O_{\delta}$ film of 60 nm thick, all deposited via aqueous CSD on 5% NiW tape

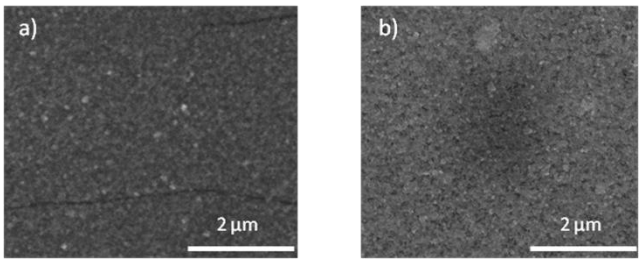

Figure 7. 6: SEM micrographs obtained for (a) $La_{0.25}Ce_{0.75}O_{1.875}$, and (b) $La_{0.5}Ce_{0.5}O_{1.75}$ layers on top of Ni-5%W tapes.

SEM micrographs (magnification 50K) for the 60 nm thick $La_{0.25}Ce_{0.75}O_{\delta}$ and $La_{0.50}Ce_{0.50}O_{\delta}$ films on NiW tape are shown in fig. 7.6. Crack-free surfaces are obtained, which is an important criterion to prevent diffusion of Ni-atoms from the tape into the YBCO layer and to suppress oxidation of the NiW tape by oxygen diffusion. A detailed analysis of the roughness of the surface was performed by AFM analysis. The root mean square (RMS) over 25 μm^2 varied from 3.9 to 7.3 for the different compositions (see figure 7.7).

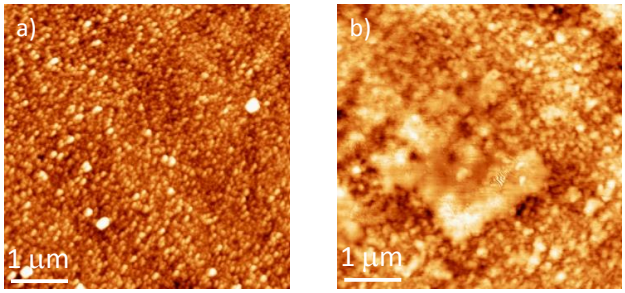

Figure 7.7: AFM analysis on 25 µm^2 a) $La_{0.15}Ce_{0.85}O_\delta$ film (RMS: 3.90) and b) $La_{0.5}Ce_{0.5}O_\delta$ film (RMS: 5.63)

The XPS depth profiles of a $La_{0.25}Ce_{0.75}O_\delta$ and a $La_{0.50}Ce_{0.50}O_\delta$ layer deposited at a dipcoating speed of 40 mm/min are shown in figure 7.8. The graphs show the results of the elemental analysis of La, Ce, Ni, W, C and O after each cycle of 40s Ar^+ bombardment. E.g. after 120 s of sputtering, a La to Ce ratio of 1:3.4 is found for the $La_{0.25}Ce_{0.75}O_\delta$ film. This is in reasonable agreement with the nominal composition where the molar ratio of La to Ce should be 1:3. Also for the $La_{0.50}Ce_{0.50}O_\delta$ layer, the La content extracted from XPS is slightly higher than expected from the experimental composition of the sample i.e. 1.07:1 instead of 1:1. This error can be explained by the error on the XPS measurements since no calibration for standard material was performed. For both samples, the same value was found for the oxygen concentration, indicating that no significant change in oxygen vacancy concentration exists between the two layers. For the $La_{0.25}Ce_{0.75}O_\delta$ layer, nickel appears in the spectrum after 280 seconds of sputtering. Approximately 200 sputter seconds later, the atomic concentrations of La and Ce drop towards zero, while the Ni concentration reaches a plateau. To calculate the Ni penetration depth from these XPS data, we need to estimate the sputter rate for the LCO layers. From ellipsometry, we determined the layer thickness of the $La_{0.25}Ce_{0.75}O_\delta$, i.e. 80 nm. If one assumes that the layer ends when the cerium concentration drops to half of its averaged plateau value (i.e. at 360 s), this means we find a sputtering rate of approx. 2.2 Å/s. Ni appears in the spectrum after 280 s and thus after sputtering away the first 60 nm of the layer. A similar Ni-penetration depth can be found for all samples, therefore an average penetration of 20 nm is calculated.

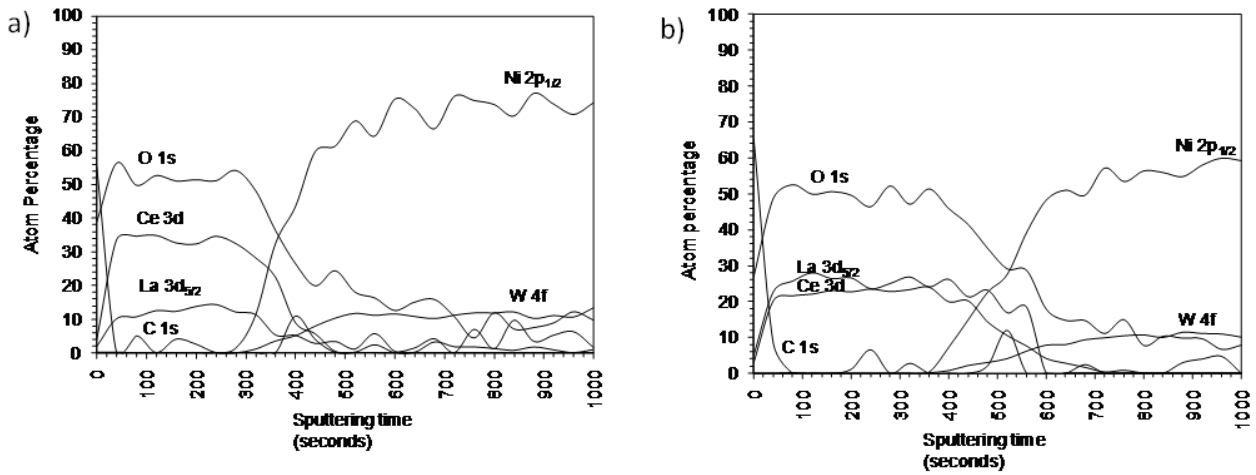

Figure 7.8: XPS depth profiling results showing the elemental composition of (a) a $La_{0.25}Ce_{0.75}O_{\delta}$ and (b) a $La_{0.5}Ce_{0.5}O_{\delta}$ thin film on NiW tape after full thermal treatment as a function of sputter time.

Thin $La_{0.25}Ce_{0.75}O_{\delta}$ and $La_{0.50}Ce_{0.50}O_{\delta}$ films (withdrawal speed = 20 mm/min) on top of a NiW tape buffered with a 280 nm thick LZO layer supplied by Zenergy Power GmbH. It is found that both layers exhibit preferential growth along the (002) direction. A FWHM value of 7.52° and 7.48° is found for the $La_{0.25}Ce_{0.75}O_{\delta}$ and $La_{0.5}Ce_{0.5}O_{\delta}$ layer respectively. Figure 7.9 shows the RHEED patterns obtained for both layers. As expected for LCO layers that exhibit a biaxially textured surface, the RHEED reflections show discrete reflection spots along the <100> and <110> viewing direction.

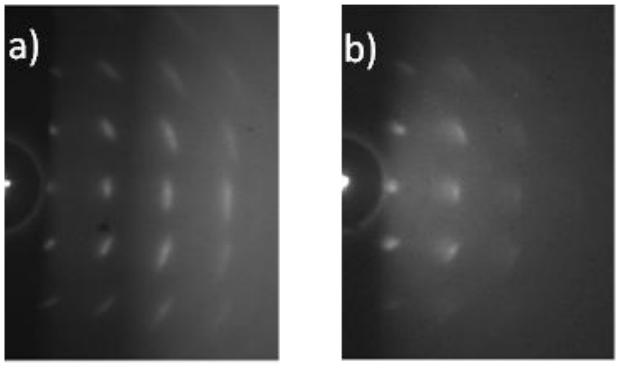

Figure 7.9: RHEED patterns collected along the <001> direction for (a) a $La_{0.25}Ce_{0.75}O_{\delta}$ and (b) a $La_{0.5}ce_{0.5}O_{\delta}$ thin film deposited on a double LZO buffer layer on Ni-5%W tape.

Figure 7.10a shows a HAADF-STEM image of a $La_{0.25}Ce_{0.75}O_{\delta}$ buffer layer in plan-view. A grain boundary network of LCO grains of 10-20 nm in size is revealed. Similar results were reported for $La_2Zr_2O_7$ buffer layers, but with increased LZO grain size (100-200 nm) [26]. Z-contrast imaging allowed to identify the dark areas seen in the figure as nanovoids of 1-2 nm in size. The size of the nanovoids found in the LCO case is reduced in comparison with the 10-20 nm in size nanovoids reported in CSD-prepared $La_2Zr_2O_7$ buffer layers [27, 28]. Figure 10b features a single ~20 nm in size LCO grain. Nanovoids ~2 nm in size are found at the LCO grain boundaries.

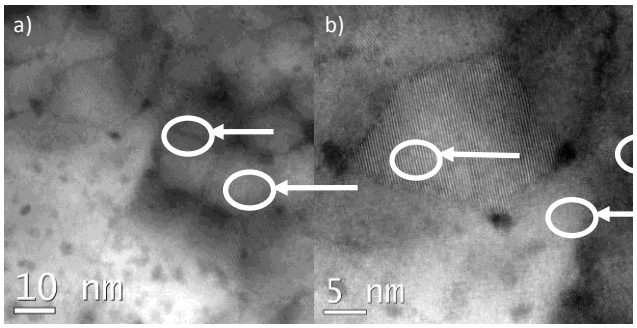

Figure 7.10: a) HAADF-STEM image of a LCO buffer layer in plan-view and b) Aberration corrected HAADF-STEM image of a LCO buffer layer in plan-view.

Figure 7.11 shows the cross-sectional SEM image as obtained after FIB slicing for a $La_{0.25}Ce_{0.75}O_{\delta}$ buffer layer of 70-90 nm thickness deposited on double LZO layers on Ni-5%W substrates. We can clearly distinguish the 90 nm thick LCO layer from the 250

nm thick, porous LZO layer underneath. Although clearly some large pores can be seen at the LCO/LZO interface, its overall appearance seems denser than for LZO. Supporting the previous observation, it can therefore be estimated that the use of LCO instead of LZO buffer layers will result in denser coatings, with less nanovoid formation and leading to voids smaller in size.

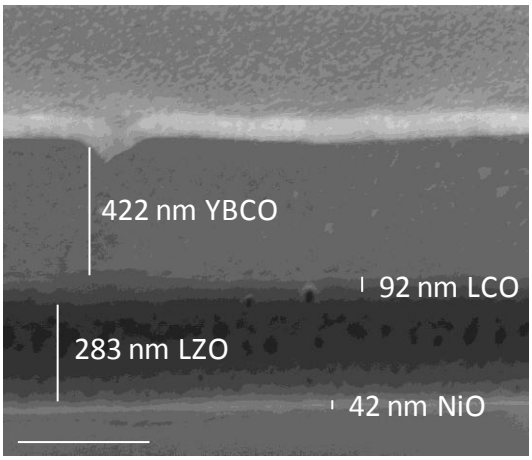

Figure 7.11: PLD-YBCO deposited LCO layer on double LZO layer of Zenergy Power GmbH

7.6 YBCO deposition on LCO buffer layers

PLD YBCO was deposited on top of $La_{0.25}Ce_{0.75}O_{\delta}$ and $La_{0.50}Ce_{0.50}O_{\delta}$ layers coated on double LZO buffered Ni-5%W substrate from Zenergy Power GmbH. After deposition of PLD-YBCO (figure 11), the LCO layer thickness remains unchanged. For the PLD-YBCO with an estimated thickness of ~300nm, a critical current density of ~0.6 MA/cm^2 in self field at 77K is determined for both LCO layers. For the layer with x = 0.25 a ΔT_c of 3.6 K is found while for the x = 0.50 LCO sample, ΔT_c is much smaller, 1.8K. Earlier, a Jc (K) of 0.6-0.8 MA/cm^2 at a ΔT_c of 1.4 K has been reported for a PLD-YBCO deposited on CeO_2 capped LZO buffer layer on Ni-5%W substrate [8]. These observations support the conclusion that the prepared LCO buffer layers using a water based CSD method can be suited buffer layers for the production of coated conductors and might have a future in replacing the more complex NiW-LZO-LZO-CeO_2 architectures.

7.7 LCZO and modified LZO buffer layers

In this research, $La_2Zr_2O_7$ films doped with varying percentages of Ce at constant La concentration ($La_{0.5}Ce_xZr_{1-x}O_y$) were prepared as well non-stoichiometric $La_{0.5+x}Zr_{0.5-x}O_y$ buffer layers with different percentages of La and Zr ratios. Ce^{4+} has a higher ionic radius (0.97 Å) than Zr^{4+} (0.86 Å) and its substitution in the Zr^{4+} lattice position of LZO results in a LCZO solid solution with pyrochlore structure and increased lattice parameter with a very high thermal expansion coefficient. Similarly, an increased percentage of La^{3+} in non-stoichiometric LZO ($La_{0.5+x}Zr_{0.5-x}O_y$) leads to an increase of the lattice parameter values due to its higher ionic radius (1.16 Å) [29]. These variable compositions can lead to minimal lattice matches with the initially formed $YBa_2Cu_3O_{6+x}$ and that of the finally formed YBCO. This is in line with lattice tuned La^{3+} doped CeO_2 (LCO) buffer layers (sec. 7.1-7.6)

The influence of the precursor solution composition on the microstructure and crystallinity was studied using XRD and SEM. Their effective buffer layer action is studied using XPS depth profiling.

7.8 Experimental Methods

Two separate ways of preparing LCZO and modified LZO were adopted as described below:

7.8.1 Preparation method for cerium doped lanthanum zirconate (LCZO) solutions

Acetic acid was added to zirconium n - propoxide (70 % w/w in n - propanol, Sigma-Aldrich) in order to stabilize it (molar ratio Zr^{4+}:HOAc = 1:4) [30] . This solution was lightly stirred. Cerium acetate ($Ce(CH_3COO)_3.xH_2O$, Sigma-Aldrich, 99.9 %), acetic acid and water ((Ce^{3+} + Zr^{4+}):HOAc: H_2O = 1:3:40) were added to this mixture. The partially dissolved mixture was heated to 60 °C. This was followed by the addition of lanthanum acetate ($La(CH_3COO)_3.xH_2O$, Sigma-Aldrich, 99.9 %), together with acetic acid and water ((La^{3+} + Zr^{4+} + Ce^{3+}):H_2O:HOAc = 1:7.5:100). The mixture was left to stir at 60 °C until all precipitates dissolved. In another beaker, ethylene diamine tetraaceticacid (EDTA, Sigma - Aldrich, 99.995 %) solution was prepared. EDTA was used as the

complexant. A specific molar ratio of the EDTA with respect to the total metal ions concentration (Ce^{3+} + La^{3+} + Zr^{4+}):EDTA = 1 : 0.5) was dissolved in water at room temperature. The dissolution of EDTA in water was aided by increasing the pH of this mixture with ethylene diamine (EDA) (molar ratio of EDTA:EDA = 0.5:4). Later, both the metal ion solution and the EDTA solutions were mixed together and the pH was adjusted to 6 with addition of ammonia. A fixed amount of ethylene glycol (EG, molar ratio EDTA:EG = 1:4) was added to this solution under stirring heated to 60 °C. The solution was evaporated until a concentration of 0.4 mol/L is obtained. According to the method described above, LCZO solutions with different percentages of zirconium and cerium ($La_{0.5}Ce_xZr_{0.5-x}O_y$ with 'x' a variable amount) with a constant lanthanum percentage were prepared. The pH of the solutions were found to be 6.0-6.2 and the viscosity 5.2-5.5 mPa s. Three different Ce^{4+} percentages substituted in LZO systems led to the following LCZO compositions : $La_{0.5}Ce_{0.10}Zr_{0.4}O_y$, $La_{0.5}Ce_{0.25}Zr_{0.25}O_y$ and $La_{0.5}Ce_{0.40}Zr_{0.10}O_y$.

7.8.2 Preparation method for non-stoichiometric modified lanthanum zirconate solutions

0.4 mol/L non-stoichiometric LZO solutions were prepared by dissolving varying percentages of lanthanum acetate in a water-acetic acid mixture (molar ratio, La^{3+}:HOAc:H_2O = 1:16:150) at 80°C until a clear solution was obtained. This was in accordance to the ratios satisfying the formula, $La_{0.5+x}Zr_{0.5-x}O_y$. The water sensitivity of the zirconium alkoxide was reduced by stabilizing it with acetic acid (molar ratio, Zr^{4+}:HOAc = 1:4) at room temperature [30]. This stabilized zirconium propoxide was diluted by adding water in a 1:20 molar ratio of Zr^{4+}:H_2O at 80°C. A clear solution was obtained after stirring for 5 minutes at this temperature. Subsequently, the zirconium precursor solution was added to the lanthanum precursor solution at 80°C. An EDTA solution (molar ratio, (La^{3+}+Zr^{4+}):EDTA = 1:0.5) was prepared by dissolving EDTA in water. The pH of this solution was increased by addition of ammonia until the dissolution of EDTA (pH between 7 and 8). This was then followed by the addition of the metal solution (La^{3+}+Zr^{4+}) added to the EDTA solution at room temperature and stirred for 10 minutes. A viscous surfactant 2-amino-2-methyl-1-propanol (AMP, Sigma-Aldrich, 95%) with a high pH (>12) was added to the mixture (molar ratio, EDTA:AMP = 1:4) to increase the wettability and pH of this water-based precursor solution. The solution was heated to 60°C. Finally, polyvinyl

pyrrolidone (PVP) (molar ratio, (La^{3+}+Zr^{4+}): PVP = 1:0.5) was added and the final solution evaporated until the desired concentration was achieved. The pH of the solution was found to be 4.6-4.8 and the viscosity 4.6-4.9 mPa s.

Two different La^{3+} and Zr^{4+} non-stoichiometric percentages were chosen that led to the following compositions: $La_{0.55}Zr_{0.45}O_y$ and $La_{0.60}Zr_{0.40}O_y$.

7.8.3 Solution stability, influence of complexant and polymer

For both the non-stoichiometric LZO and the LCZO precursor solutions, the zirconium propoxide was stabilized by mixing it with acetic acid in order to handle it in non-vacuum and water-based conditions. Acetic acid partially replaces the propoxide (OPr) groups by acetate groups (OAc) forming a zirconium propoxide-acetate complex that reduces the chances of immediate hydrolysis and condensation reaction of zirconium propoxide on the addition of water [30]. EDTA was used as a strong chelating agent for both precursors. It can form very strong complexes with lanthanum, cerium and zirconium ions [17, 18], avoiding the metal ions from precipitating when high metal concentrations are reached during the transformation from solution to gel. For both precursors, additives are necessary to increase the viscosity and improve the wetting behavior over the metal substrate. EG was used in the LCZO solution preparation to increase the viscosity of the water-based solution. This allows the preparation of thicker layers from one single coating. A combination of AMP and PVP was used for the same reason in the non-stoichiometric LZO preparations. PVP is considered to promote structural relaxation during the heat-up stage of the annealing treatment thereby causing a reduction in stress during the formation of the layer and thus suppressing crack formation [31] and AMP acts as a surfactant. AMP and PVP cannot be used in the presence of Ce-precursor where they cause precipitation.

7.9 Solution deposition and heat-treatment for LCZO and modified LZO layers

The substrates were cleaned and duly as described (Chapter 3). The cleaned Ni-5%W substrates were dip-coated in a clean room (class 10000; flow cupboard class 100) in order to prevent any contamination from dust particles. The dip-coat speed was varied

between 20 mm/min and 60 mm/min. The as-deposited wet layers were transformed into a gel by placing them in a drying furnace at 60°C for one hour. The amorphous layers in their gel state were subjected to a suitable heat treatment that resulted in a desired crystalline metal oxide phase, in the following sequence: Firstly, the layers were heated from room temperature to 450°C (ramp rate of 1°C/min) and let to dwell for one hour. Secondly, a 3°C/min heating ramp was applied from 450°C until 900°C (dwell time = 1h). Finally, the films were heated to 1050°C at a 10°C/min ramp with a dwell time of one hour. After the heat treatment, the furnace was switched off and the samples were left to cool inside the furnace. The entire heating process was carried out in an Ar-5%H_2 atmosphere (gas flow rate: 0.1 L/min).

7.10 Results and discussion

7.10.1 Crystallinity and orientation

From ellipsometry, we find that at the maximum dipcoating speed of 40mm/min, crack-free non-stoichiometric LZO layers of about 140 nm thick can be obtained. In the case of LCZO solutions, which have a slightly higher viscosity, the withdrawal speed is reduced to 20mm/min, to achieve the same layer thickness. The epitaxial growth and crystallinity of these LCZO buffer layers and non-stoichiometric buffer layers of varying composition prepared from water-based precursor solutions were analyzed using XRD (Figure 7.12). For both systems, mainly reflections related to the epitaxially grown, c-axis oriented pyrochlore structure of stoichiometric LZO could be found. In all samples, much weaker reflections related to the formation of a small fraction of the undesired (2 2 2) growth are also present. No additional reflections, indicative of the formation of secondary phases could be distinguished. Although a textured growth along the (002) plane of the Ni-W tape is observed, untextured part is visualized with the presence of (111) peak. For a stoichiometric LZO buffer layer with a pyrochlore structure, the (0 0 4) peak position normally is observed at 2θ=33.3° and the less intense (0 0 8) peak position at 2θ=69.8° [7]. In the case of the LCZO film, clearly the (0 0 4) and (0 0 8) reflections shifts to lower angles as a function of Ce^{4+} doping percentage. This indicates that the larger Ce^{4+} ions are successfully doped into the LZO lattice, leading to an increase of the lattice parameter of the LCZO buffer layers, as can be expected from the larger ionic radius of Ce^{4+} (101 pm) compared to Zr^{4+} (86 pm). In the case of non-stoichiometric LZO, the peak shift is much more limited. In Table 1 and 2, the lattice parameters, calculated according to Bragg's law, from the shifted peak positions as shown in Fig. 7.12 are given. In the case of LCZO, the lattice parameter increases from 10.79 to 10.99 Å, upon replacing 80% of the Zr ions with Ce. For non-stoichiometric LZO, a shift from 10.79 to 10.89 Å is calculated when moving from stoichiometric LZO to $La_{0.6}Zr_{0.4}O_y$.

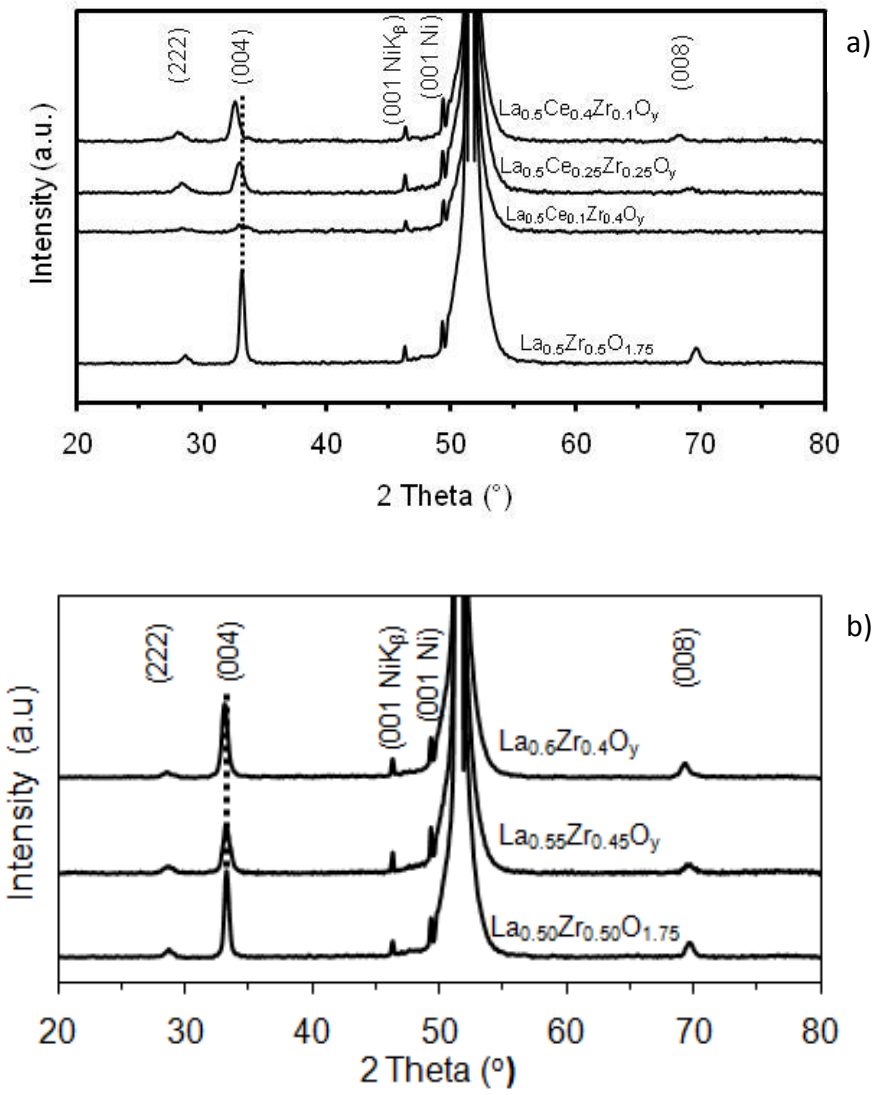

Figure 7.12: X-ray Θ-2 Θ diffraction patterns obtained for (a) LCZO buffer layers and (b) Non-stoichiometric LZO buffer layers

In table 7.2, the lattice parmaters as calculated from XRD for the range of LCZO samples is shown, together with the lattice mismatches with the Ni-5%W substrate, the $YBCO_7$ a- and b-axis and the $YBCO_6$ a-axis.

Table 7.2: Lattice parameters of the $La_{0.5}Ce_xZr_{0.5-x}O_y$ thin films and their lattice mismatch with the Ni-5%W substrate and that of YBCO.

Sample	Lattice parameter a (Å)	Lattice mismatch with Ni-5%W (%) (3.54 Å)	Lattice mismatch with $Y_1Ba_2Cu_3O_{6+x}$ (%) (3.8578 Å)	Lattice mismatch with the *a*-axis of $Y_1Ba_2Cu_3O_{7-x}$ (%) (3.83 Å)	Lattice mismatch with the *b*-axis of $Y_1Ba_2Cu_3O_{7-x}$ (%) (3.889 Å)
$La_{0.5}Zr_{0.5}O_{1.75}$	10.79	7.76	1.11	0.50	1.82
$La_{0.5}Ce_{0.1}Zr_{0.4}O_y$	10.82	8.06	0.84	0.12	1.63
$La_{0.5}Ce_{0.25}Zr_{0.25}O_y$	10.85	8.35	0.58	-0.16	1.37
$La_{0.5}Ce_{0.4}Zr_{0.1}O_y$	10.99	9.76	-0.72	-1.45	0.09

$La_{0.5}Ce_{0.25}Zr_{0.25}O_y$ shows minimal lattice mismatch towards $YBa_2Cu_3O_{6+x}$ (0.58 %) while $La_{0.5}Ce_{0.4}Zr_{0.1}O_y$ has a lattice mismatch of only 0.09 % with the *b*-axis of YBCO and has an acceptable mismatch with $YBa_2Cu_3O_{6+x}$. Yet, it should be pointed out that introducing Ce also unavoidably leads to a worse mismatch with the underlying Ni-5%W substrate, yet in XRD, no disturbance of the epitaxial growth could be inferred from this.

By increasing La^{3+}:Zr^{4+} ratio in the lanthanum zirconium oxide lattice ($La_{0.5+x}Zr_{0.5-x}O_y$), the lattice parameter of the $La_{0.5+x}Zr_{0.5-x}O_y$ increases and accordingly the thin films can be tailored to provide a minimal lattice mismatch with the a- axis of YBCO. Substitution until 60% of La^{3+} is possible without disturbing crystal growth and inducing the formation of secondary phases. This is because, for more than 60% of La^{3+} substitution, next to the pyrochlore phase, also fluorite occurs [1]. Table 7.3 provides the lattice mismatch calculation for the prepared layers to that of Ni-5%W substrate and to different relevant YBCO lattice parameters.

Table 7.3: Lattice parameters of the $La_{0.5+x}Zr_{0.5-x}O_y$ thin films and their lattice mismatch with the Ni-5%W substrate and that of YBCO.

Sample	Lattice parameter a (Å)	Lattice mismatch with Ni-5%W (%) (3.54 Å)	Lattice mismatch with $Y_1Ba_2Cu_3O_{6+x}$ (%) (3.8578 Å)	Lattice mismatch with the *a*-axis of $Y_1Ba_2Cu_3O_{7-x}$ (%) (3.83 Å)	Lattice mismatch with the *b*-axis of $Y_1Ba_2Cu_3O_{7-x}$ (%) (3.889 Å)
$La_{0.5}Zr_{0.5}O_{1.75}$	10.79	7.76	1.11	0.50	1.82
$La_{0.55}Zr_{0.45}O_y$	10.83	8.20	1.06	0.2	1.84
$La_{0.60}Zr_{0.40}O_y$	10.89	8.39	0.99	0.07	1.90

$La_{0.60}Zr_{0.40}O_y$ e.g. shows an almost zero lattice mismatch to that of the YBCO a-axis which might lead to high quality YBCO growth on top of these buffer layers.

7.10.2 Buffer layer action: XPS Study

The capacity of the buffer layers to withstand nickel penetration was evaluated by XPS depth profiling. Fig. 7.13 shows the result of 20 consecutive sputter cycles, each consisting of an elemental analysis of La, Ce, Ni, W, C, O after 40 seconds of Ar^+ ion bombardment for an as-deposited $La_{0.50}Ce_{0.10}Zr_{0.40}O_y$ layer. The layer under study has a thickness of 65 nm (dip-coating speed : 40 mm/min) as obtained from ellipsometry.

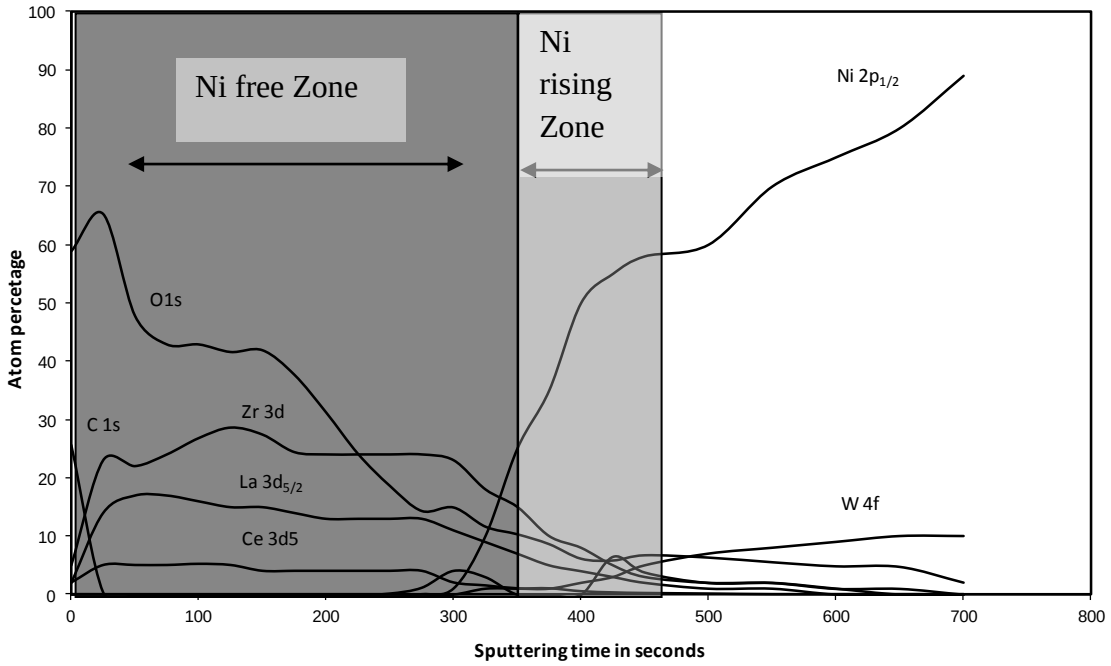

Figure 7.13: XPS depth profile spectrum for $La_{0.5}Ce_{0.10}Zr_{0.40}O_y$ layer

For a rough estimation of the Ni penetration depth one can assume the following : the buffer layer ends when the concentration of the Zr drops below half of its original value. In this layer, this occurs after 350 seconds of sputtering. Thus roughly 65 nm is sputtered in 350 seconds or we have a sputtering rate of 1.8 Å/s. The first Ni peak appears at 300 s of sputtering. The nickel-free zone on the top of the sample is thus approximately 54 nm. The thickness of the penetration zone is estimated to be ~11 nm. Accordingly, it can be confirmed that the $La_{0.5}Ce_{0.10}Zr_{0.40}O_y$ acts as a good barrier layer against Ni penetration.

7.11 Conclusions

In this work, it is found that doping of up to 50 % of La in CeO_2 is possible without the formation of any secondary phases. A linear expansion of the fluorite lattice with increasing La^{3+} content is deduced. For LCO layers on NiW tape, the same trend is found. All LCO layers, with x up to 0.5, grow epitaxially on NiW tape, yet clearly the increased lattice mismatch with the substrate suppresses crystallinity along the (001)

direction when x > 0.25. The in-plane orientation of the LCO layers obtained here is of comparable quality to that of the more established CSD LZO films. RHEED analysis shows that for thin layers, good biaxial surface texture is present. The deposited LCO layers have a more dense look in TEM-FIB analysis and the nanovoid size (of 1-2 nm) is considerably reduced in comparison with CSD-LZO prepared buffer layers. Results from XPS depth profiling show that Ni penetration is only present in the first 20 nm for an average thickness of 80nm for the LCO layer after thermal treatment, proving the buffer capacity of the layers. Deposition of a 300 nm thick YBCO layer by PLD gives a Jc value of 0.6 MA/cm^2 both on $La_{0.25}Ce_{0.75}O_{\delta}$ and $La_{0.5}Ce_{0.5}O_{\delta}$. These observations support the conclusion that the LCO buffer layers prepared using water based sol-gel route are suited for coated conductors and might have a future in replacing the more complex NiW-LZO-LZO-CeO_2 architectures.

For the cerium doped LZO ($La_{0.50}Ce_{1-x}Zr_{0.5-x}O_y$) and the non-stoichiometric LZO lanthanum zirconium oxide ($La_{0.5+x}Zr_{0.5-x}O_y$) buffer layers, a shift in lattice parameter was observed for varying doping percentages. The lattice parameters of these layers were tunable according to the lattice parameters of YBCO to provide less lattice mismatch. The XPS study showed that the buffer layer was effective in preventing the diffusion of Ni atoms. Further research need to explore the possibility of depositing good YBCO on top of these buffer layers is needed.

References

[1] Y. Akin, Z.K. Heiba, W. Sigmund, Y.S. Hascicek, Solid-State Electron.47(2003) 2171.

[2] G. Li, M.H. Pu, X.H. Du, R.P. Sun, H. Zhang, Y. Zhao Physica C 463 (2007) 589.

[3] K. Chiba, S. Makino, M. Mukaida, M. Kusunoki, S. Ohshima IEEE Trans. Appl. Supercond.(2001) 1-4.

[4] Y. Takahashi, Y. Aoki, T. Hasegawa, T. Maeda, T. Honjo, Y. Yamada, Y. Shiohara, Physica C 412 (2004) 905-912.

[5] D. Chambonnet, D. Keller, C. Belouet, Physica C 302 (1998) 198-207.

[6] L. Arda, Z.K. Heiba, Thin Solid Films 518 (2010) 334-3354.

[7] M.P. Paranthaman, S. Sathyamurthy, X. Li, E.D. Specht, S.H. Wee, C. Cantoni, A. Goyal, M.W. Rupich, Physica C 470 (2010) 352-355.

[8] Y. Wang , H. Guo, S. Gong, Ceram. Int. 35 (2009) 2639-2646.

[9] W.Ma, S. Gong, H. Xu , X. Cao , Surf. Coat. Techol. 200 (2006) 5113-5116.

[10] N. J. Lawrence, J.R. Brewer, L. Wang, T.S. Wu, J.W. Kingsbury, M. M. Ihrig, G. Wang, Y. L. Soo, W. N. Mei, C. L. Cheung, Nano Lett. 11 (2011) 2666-2673.

[11] F. Zhang , P. Wang , J. Koberstein , S. Khalid , S. W. Chan, Surf. Sci 563 (2004) 74-85.

[12] D. E. P. Vanpoucke, P. Bultinck, S. Cottenier, V. Van Speybroeck, I. Van Driessche, Phys. Rev. B 84 (2011) 054110-054113.

[13] M. Coll, J. Gazquez, F. Sandiumenge, T. Puig, X. Obradors, J. P. Espinos, R Hühne, Nanotechnology 19 (2008) 395601-395606.

[14] F. Zhang, S.W. Chan, J. E. Spanier, E. Apak, Q. Jin, R.D. Robinson, I. P. Herman, Appl. Phys. Lett. 80 (2002)127-130.

[15] S. Patil, S. Seal, Y. Guo, A. Schulte, John Norwood, Appl. Phys. Lett. 88 (2006) 243110-243113.

[16] S. Babu, R. Thanneeru, T. Inerbaev, R. Day, A.E. Masunov, A. Schulte, Sudipta Seal, Nanotechnology 20 (2009) 085713-.085717.

[17] T. Thuy Tran, S. Hoste, G. Herman G, N. Van de Velde, K. De Buysser, I. Van Driessche, J. Sol-Gel Sci. Technol. 51 (2009) 112-122.

[18] A. E. Martell, R. M. Smith, Critical stability constants, 1975, Vol. 2, Plenum press, New York.

[19] X. Cao, R. Vassen, W. Fischer, F. Tietz, W. Jungen, D. Stover, Adv. Mater. 15 (2003) 1438-1445.

[20] J. S. Bae, W. K. Choo, C. H. Lee, J. Eur. Ceram. Soc., 24 (2004) 1291-1300.

[21] K. M. Ryan, J. P. McGrath, R. A. Farrell, W. M. O'Neill, C. J. Barnes, M. A. Morris, J. Phys.-Condes. Matter 15 (2003) L49-L55.

[22] T. J. B. Holland, S A.T. Redfern, Mineral. Mag. 61(1975) 65-68.

[23] J. R. Mc Bride, K. C. Hass, B. D. Poindexter, W.H. Weber, J. Appl. Phys.76 (1994) 2435-2438..

[24] V. Bellière, G. Joorst, O. Stephan, F. M. F. de Groot, B. M. Weckhuysen, J. Phys. Chem. B 110 (2006) 9984-9992.

[25] B. C. Morris, W. R. Flavell, W. C. Mackrodt, and M. A. Morris, J. Mater. Chem. 3 (1993) 1007-1110

[26] L. Molina, S. Engel, K. Knoth, R. Huhne, B. Holzapfel, O. Eibl J. Phys.: Conf. Ser. 97 (2008) 012108-012110.

[27] L. Molina, K. Knoth, S. Engel, B. Holzapfel, O. Eibl, , Supercond. Sci. Technol. 19 (2006) 1200-1210.

[28] L. Molina, H. Tan, E. Biermans, K. J. Batenburg, J. Verbeeck, S. Bals, G. Van Tendeloo, Supercond. Sci. Technol 24 (2011) 065019-06502.

[29] M.P. Paranthaman, S. Sathyamurthy, X. Li, E.D. Specht, S.H. Wee, C. Cantoni, A. Goyal, M.W. Rupich, Physica C: Supercond. 470 (2010) 352-356.

[30] G. Yi, M. Sayer, J. Sol-Gel Sci. and Tech. 6 (1996) 65-74.

[31] H. Kozuka, A. Higuchi, Journal of Materials Research 16 (2001) 3116-3123.

Summary and conclusions

In the context of coated conductors, there is a need towards a simplification of the typical two or even three layered buffer structure. This research explored the use of polymers to prepare thicker LZO layers and three new layers based on doping of lanthanum in CeO_2, doping of cerium in LZO and modified LZO to replace the CeO_2/LZO films in an YBCO/CeO_2/LZO/NiW structure.

This thesis is divided into eight chapters. The first chapter gives an introduction to superconductivity and the three generations of superconductors, in particular the second generation or so called coated conductor design. The second chapter summarizes the experimental techniques that were used in this thesis. Preparation of the substrates is dealt in chapter 3. The necessity of a single, thick layer is shown in chapter 4 with some XPS analysis. The solution preparation chemistry and characterization thicker LZO layers and three new layers based on doping of lanthanum in CeO_2, doping of cerium in LZO and modified LZO are described in chapters 5-7. Chapter 5 specifically deals with preparation and characterization of thick LZO layers. In Chapter 6, the single LZO layers and their counterpart of single LZO layers treated under simulated YBCO conditions are compared for their performance as buffer layer. Chapter 7 deals with La^{3+} doping in CeO_2 and doping of cerium in LZO and modified LZO to replace the CeO_2/LZO films in an YBCO/CeO_2/LZO/NiW structure.

In chapter 3, the main focus was to obtain a wettable Ni-5%W substrate for coating water-based solutions. Since XPS could provide significant information on the contamination percentages of C, Ni and O through the thickness of the sample by means of sputtering, an in-depth study was undertaken. This, supported with a RHEED analysis, proved that a combination of chemical cleaning with etching+thermal cleaning is best-suited in terms of wettability and minimal contaminations. The reverse treatment of the substrate by thermal followed by chemical cleaning with etching showed increase in oxygen content of the substrate which could be correlated to NiO formation. Since NiO tends to grow along the (1 1 1) plane, a cleaning such as this will result in growth of buffer layers along the (1 1 1) orientation, which should be avoided.

In chapter 4, the crystallinity and interface diffusion in multiple buffer layer depositions were studied with the help of XRD and XPS. Accordingly, in a system of CeO_2(20nm) / LZO (70nm) / Ni-5%W compared to that of CeO_2(20nm) / LZO(50 nm) / CeO_2(20nm) / Ni-5%W, the desired (0 0 4) growth was seen in CeO_2 (20nm)/LZO (50 nm)/CeO_2 (20nm)/Ni-5%W system as studied from the XRD analysis. On the contrary, this system showed inter-difussion in the interfaces and significant Ni penetration without good barrier properties as inferred from XPS. However, CeO_2 (20nm)/LZO (50 nm)/CeO_2 (20nm)/Ni-5%W showed better barrier properties especially in the LZO region inspite of less (0 0 4) growth in comparison to the CeO_2(20nm) / LZO(50 nm) / CeO_2(20nm) / Ni-5%W system. Hence, it was concluded that, multiple buffer layers led to significant inter-diffusions in the interface that is undesirable and LZO was a better barrier against Ni penetration. The good crystallinity of CeO_2 (20nm)/LZO (50 nm)/CeO_2 (20nm)/Ni-5%W system could be attributed to thin CeO_2 layer of 20 nm on the Ni-5%W substrate which acts as seed layer minimizing stress in the substrate-layer interface and aiding epitaxial growth of to-be deposited thicker layers. Hence, it was concluded that water-based LZO can act as a good barrier layer and preparation of thicker LZO with optimal properties were considered for further investigations.

In chapter 5, a combination of additives in the form of EDTA-AMP-PVP proved to be better than EDTA-EDA-EG-PVP for obtaining LZO solutions from which non-porous layers could be derived. It was believed that an EDTA-EDA-EG-PVP combination led to longer polymeric chain in the solution state that gave rise to pores during pyrolysis that could not be filled even during crystallization. On the other hand, EDTA-AMP-PVP led to lower polymeric chains with a non-porous layer. This led to the conclusion that inclusion of a polymer and hence the porosity of the layer as result is inter-dependent on the total chemical species present in the system and not the mere presence of the polymer.

In chapter 6, XPS analysis on the LZO systems was conducted in their as-prepared state and after treatment in simulated YBCO conditions. It was found that, with simulated YBCO treated conditions, the Ni-free region decreased in comparison to an as-prepared sample. On the other hand, the performance of the water-based LZO layers and non-water-based LZO layers (from

Zenergy Power GmbH) were comparable in terms of prevention of Ni penetration. It was concluded that a layer thickness of 125-150 nm is required to effectively prevent Ni diffusion.

In chapter 7, doping of CeO_2 with La^{3+} (LCO), Ce doping in LZO and non-stoichiometric LZO layers were studied. These doped layers showed the possibility of lattice tuning as a function of doping percentages. Interestingly, for LCO layers the nanovoids were smaller in comparison to the LZO layers. Since the presence of these nanovoids are considered harmful for the buffer layer capacity, this can be considered as a major observation.

To conclude, the research work showed:

1. The possibility of choosing better cleaning methods
2. The necessity of single or lesser number of buffer layers compared to multiple buffer layers.
3. The possible use of polymers in a better chemical combination for obtaining non-porous buffer layers with improved thickness.
4. A thickness dependency of simulated YBCO condition treatment of LZO layers leading to Ni-free regions.
5. The possibility to obtain doped and lattice tuned buffer layers towards single buffer layers.

Peer-reviewed Publications

- *A nitrilo-tri-acetic-acid/acetic acid route for the deposition of epitaxial cerium oxide films as high temperature superconductor butter layers*: T.T. Thuy, P. Lommens, **V. Narayanan**, N. Van de Velde, K. De Buysser, G. Herman, S. Hoste, I. Van Driessche, Journal of Solid State Chemistry 183 (2010) 2154-2160
- *Thick lanthanum zirconate buffer layers from water-based precursor solutions on Ni-5%W substrates*: **Vyshnavi Narayanan**, Petra Lommens, Klaartje De Buysser, Ruben Hühne, Isabel Van Driessche, Journal of Solid State Chemistry (2011), 184, Issue 11, 2887-2896
- *Aqueous CSD approach for the growth of lattice-tuned novel $La_xCe_{1-x}O_\delta$ epitaxial layers*: **Vyshnavi Narayanan**, Petra Lommens, Klaartje De Buysser, Ruben Hühne, Danny Vanpoucke, Leopoldo Molina, Gustaaf Van Tendeloo, Pascal Van Der Voort, Isabel Van Driessche, Journal Materials Chemistry *(*2012), 22, Issue 17, 8476 – 8483.
- *XPS depth profiling for evaluation of LZO buffer layer capacity*: **Vyshnavi Narayanan**, Klaartje De Buysser, Els Bruneel, Isabel Van Driessche, Materials *(*2012), 5, Issue 3, 364-376.
- *Effective cleaning of substrate, study on multiple buffer layers leading to a need of single buffer layers all from water based precursors*: **Vyshnavi Narayanan**, Petra Lommens, Isabel Van Driessche, To be submitted to IEEE journal of superconductivity.
- *Effect of polymer on thickness and morphology in buffer layers*: *XPS and microstructural study:* **Vyshnavi Narayanan**, Isabel Van Driessche, To be submitted to Materials Letters.
- *Novel water-based buffer layers for YBCO coated conductors: A review:* **Vyshnavi Narayanan**, Isabel Van Driessche, To be submitted to Nanomaterials.
- *XPS as a tool for study of the characteristics of buffer layers: A review:* **Vyshnavi Narayanan**, Isabel Van Driessche, in preparation.

Presentations at conferences

***Oral Presentations*:**

- *Novel water based lanthanum zirconate and lanthanum cerium oxide buffer layers for YBCO coated conductors*: **V. Narayanan**, E. Bruneel, P. Lommens, K. De Buysser, S. Hoste, I. Van Driessche, VJC 10, 1st-2nd March 2010, Blankenberge, Belgium.
- *Novel water-based lanthanum zirconate and doped buffer layers for YBCO coated conductors*: **V. Narayanan**, D. Vanpoucke, P. Lommens, E. bruneel, K. De Buysser, S. Hoste, I. Van Driessche, BCerS annual meeting 2011, 7th February 2011, Mons, Belgium.
- *Chemical solution deposition of novel, thick and dense lattice-matched single buffer layers for YBCO coated conductors: Preparation and characterization*: **V. Narayanan**, P. Lommens, E.Bruneel, K. De Buysser, M. Bäcker, R. Hühne and I. Van Driessche, MPA meeting 2011, 27th-29th June 2011, Alvor Portugal.
- *Chemical solution deposition of thick and dense single buffer layers for YBCO coated conductors from water based precursors*: **Vyshnavi Narayanan**, Petra Lommens, Els Bruneel, Klaartje De Buysser, Ruben Hühne, Michael Bäcker and Isabel Van Driessche, EUCAS-2011, 18th-23rd September 2011, Den Haag, Netherlands.

***Poster Presentations*:**

- *Characterization and studies on novel water based cerium oxide precursor solution for coated conductors*: **V. Narayanan**, I. Van Driessche, Tran Thi Thuy, E. Bruneel, D. Vandeput and S. Hoste, Jong KVCV conference, 4th April 2008, Antwerp University, Belgium.
- *X-ray photoelectron spectroscopy studies on three buffer layered architecture in HTSC*: **V. Narayanan**, I. Van Driessche, V. Cloet, J. Feys, E. Bruneel, Nico De Roo and S. Hoste, i-SUP 2008 conference, 22nd- 25th April 2008, Brugge, Belgium.
- *Deposition and characterization of multiple buffer layer architecture in HTSC*: **V. Narayanan**, I. Van Driessche, V. Cloet, N. Van de Velde and S. Hoste, Doctoraat symposium, 28th April 2009, Ghent University, Belgium.
- *Multiple buffer layer architecture in HTSC- Deposition and characterization*: **V. Narayanan**, I. Van Driessche, V. Cloet, N.Van de Velde and S. Hoste, EUCAS-2009, 13th-17th September 2009, Dresden, Germany.
- *Novel water-based lanthanum zirconate and doped buffer layers for YBCO coated conductors*: **V. Narayanan**, D. Vanpoucke, P. Lommens, E. Bruneel, K. De Buysser, S. Hoste, I. Van Driessche, ACIN 2011, 11th-14th September 2011, Namur, Belgium.